

Electronic Theses and Dissertations, 2004-2019

2013

High Flux Isolated Attosecond Pulse Generation

Yi Wu

University of Central Florida

 Part of the [Electromagnetics and Photonics Commons](#), and the [Optics Commons](#)
Find similar works at: <https://stars.library.ucf.edu/etd>
University of Central Florida Libraries <http://library.ucf.edu>

This Doctoral Dissertation (Open Access) is brought to you for free and open access by STARS. It has been accepted for inclusion in Electronic Theses and Dissertations, 2004-2019 by an authorized administrator of STARS. For more information, please contact STARS@ucf.edu.

STARS Citation

Wu, Yi, "High Flux Isolated Attosecond Pulse Generation" (2013). *Electronic Theses and Dissertations, 2004-2019*. 2877.

<https://stars.library.ucf.edu/etd/2877>

HIGH FLUX ISOLATED ATTOSECOND PULSE GENERATION

by

YI WU

B.S., University of Science and Technology of China, 2006

A dissertation submitted in partial fulfilment of the requirements
for the degree of Doctor of Philosophy
in the College of Optics and Photonics
at the University of Central Florida
Orlando, Florida

Fall Term
2013

Major Professor: Zenghu Chang

© 2013 Yi Wu

ABSTRACT

This thesis outlines the high intensity tabletop attosecond extreme ultraviolet laser source at the Institute for the Frontier of Attosecond Science and Technology Laboratory.

First, a unique Ti:Sapphire chirped pulse amplifier laser system that delivers 14 fs pulses with 300 mJ energy at a 10 Hz repetition rate was designed and built. The broadband spectrum extending from 700 nm to 900 nm was obtained by seeding a two stage Ti:Sapphire chirped pulse power amplifier with mJ-level white light pulses from a gas filled hollow core fiber. It is the highest energy level ever achieved by a broadband pulse in a chirped pulse amplifier up to the current date.

Second, using this laser as a driving laser source, the generalized double optical gating method is employed to generate isolated attosecond pulses. Detailed gate width analysis of the ellipticity dependent pulse were performed. Calculation of electron light interaction dynamics on the atomic level was carried out to demonstrate the mechanism of isolated pulse generation.

Third, a complete diagnostic apparatus was built to extract and analyze the generated attosecond pulse in spectral domain. The result confirms that an extreme ultraviolet super continuum supporting 230 as isolated attosecond pulses at 35 eV was generated using the generalized double optical gating technique. The extreme ultraviolet pulse energy was ~ 100 nJ at the exit of the argon gas target.

To my family

ACKNOWLEDGMENTS

First, I would like to thank my advisor Dr. Zenghu Chang for his guidance. I am really thankful that he brings me to this exciting research field and constantly gives me invaluable advice. I have learned a lot from my advisor about how to conduct effective research and how to properly arrange resource allocation in a project. Next I would like to give my appreciations to other group members. Dr. Hiroki Mashiko, who has been a very patient teacher for me when I started my research; Dr. Chengquan Li, who taught me to always think outside the box and Dr. Kun Zhao, who I have worked with on KLS laser and later played a vital role in setting up iFAST lab at UCF. I own Dr. He Wang many thanks since he was the one introduced me to this group and helped me started my research work at beginning. My time of working with Dr. Steve Gilbertson had taught me what is hard working. In the new iFAST lab, setting up the new laser and high power attosecond beam line relied on a large team. Xiaowei Wang, Yang Wang, Dr. Michael Chini and Eric Cunningham all have contributed their hard work to different parts of the project. For this thesis, I should especially thank Eric Cunningham and Dr. Michael Chini, if not for their encouraging and help, I would never finish it in time. In addition to those mentioned above, I would like to recognize the input of Sabih Khan, Dr. Ximao Feng, Dr. Eric Moon, Dr. Chenxia Yun, Qi Zhang, Al Rankin, Huaping Zang, Jie Li, Yiduo Zhan. Finally I want to thank people who are so important in my life. My wife Xin Xie, my father Zheng Wu and my mother Yunfang Sun, who supported me during this long journey.

TABLE OF CONTENTS

LIST OF FIGURES	x
LIST OF TABLES	xv
CHAPTER 1: INTRODUCTION	1
1.1 High Harmonic Generation	1
1.2 Isolated Attosecond Pulse Generation	5
1.3 Overview of Thesis	6
1.4 Summary of My PhD Research	7
CHAPTER 2: LASER FACILITY AT INSTITUTE FOR THE FRONTIER OF ATTOSEC- OND SCIENCE AND TECHNOLOGY LAB	9
2.1 Chirped Pulse Amplifiers	10
2.2 Pulse Stretching and Compressing	10
2.2.1 Stretcher and compressor	11
2.2.2 Multipass amplifier vs. regenerative amplifier	13
2.3 iFast 20 fs, 3.5 mJ 1 kHz Multipass CPA System	15
2.4 20 TW, 14 fs, Multi-Pass CPA System	18

2.4.1	White light generation in hollow-core fiber	19
2.4.2	300 ps Öffner type stretcher	23
2.4.3	Two-stage multipass amplifier	25
2.4.4	Numerical analysis of the 2-stage amplifier	27
2.4.5	Gain narrowing compensation filter	31
2.4.6	Dielectric mirror for high energy broadband pulse amplification	36
2.4.7	20 TW laser amplifier compressor	39
2.4.8	Pulse duration and power stability measurement	44
 CHAPTER 3: PHASE CONTROL OF SHORT PULSES		 48
3.1	Femtosecond Spectral Phase Control	48
3.2	Adaptive Phase Modulator	49
3.2.1	0.5 mJ, 5 fs Pulse from Adaptive Phase Modulator	50
3.2.2	Deformable mirror-based high-throughput phase modulator for TW laser	55
3.3	Carrier Envelope Phase	59
3.3.1	Stabilization of the carrier envelope phase in oscillator	60
3.3.2	Carrier envelope phase stabilization of chirped pulse amplifier	61
3.3.3	Carrier envelope phase stabilization for iFAST kHz CPA system	64

CHAPTER 4: HIGH FLUX ISOLATED ATTOSECOND PULSE GENERATION	68
4.1 Attosecond Gating for Isolated Attosecond Pulse Generation	69
4.1.1 Polarization gating and Two color gating	69
4.1.2 Double optical gating	72
4.2 GDOG for Single Attosecond Pulse Generation from Multi-Cycle Driving Lasers .	74
4.2.1 GDOG gate width analysis	76
4.2.2 Single atom ionization probability analysis	79
4.2.3 Attosecond Pulses from Carrier Envelope Phase Unstabilized Lasers	82
4.3 High-Flux Attosecond XUV Continuum Generation	84
4.3.1 Phase matching for enhancing attosecond pulse photon flux	86
4.3.2 GDOG gated attosecond pulse generation with TW driving laser	92
CHAPTER 5: OUTLOOK AND CONCLUSIONS	99
APPENDIX A: SOURCE CODE FOR DEFORMABLE MIRROR PHASE MODULATOR PHASE CORRECTION	100
APPENDIX B: LIST OF ACRONYMS/ABBREVIATIONS	104
APPENDIX C: COPYRIGHT PERMISSIONS	108

APPENDIX D: LIST OF MY PUBLICATIONS 113

LIST OF REFERENCES 117

LIST OF FIGURES

Figure 1.1: The 3-step model of HHG.	2
Figure 1.2: A typical HHG spectrum. After the fast decreasing of signal in the low energy region, a plateau with comparable strength was followed by an abrupt cutoff.	4
Figure 2.1: Photo of iFAST lab laser system.	9
Figure 2.2: The temporal shape of a pulse undergoing a chirped-pulse amplification process.	11
Figure 2.3: The block diagram of kHz laser	12
Figure 2.4: Schematic of a typical regenerative amplifier.	14
Figure 2.5: Vacuum chamber of kHz Ti:Sapphire crystal.	16
Figure 2.6: Schematic of kHz amplifier system.	17
Figure 2.7: Hollowcore fiber for spectrum broadening.	21
Figure 2.8: Öffner-type stretcher for >200 nm, 300 ps pulse stretching.	24
Figure 2.9: Schematic of 1st stage amplifier system.	26
Figure 2.10: Instantaneous gain $G(t)$ for the five-pass amplifier stage.	28
Figure 2.11: Output energy as a function of pass number.	29

Figure 2.12: Calculated and experimental spectra for 2nd CPA stages seeded with white light pulse from HC fiber.	31
Figure 2.13: Gaussian shaped gain curve of Ti:Sapphire crystal at cryogenic temperature.	32
Figure 2.14: Properties of gain narrowing compensation filter.	34
Figure 2.15: The kHz laser spectra with and without spectral filtering.	36
Figure 2.16: Calculated reflectivity and group delay of the broadband high-energy mirror.	39
Figure 2.17: Vacuum compressor for sub 15 fs, 20 TW beamline.	41
Figure 2.18: RF discharge grating cleaning.	43
Figure 2.19: Characterization of the 14 fs laser pulse by SHG FROG.	45
Figure 2.20: Single shot pulse energy recorded by sampling a portion of the power amplifier output with a fast photodiode.	46
Figure 2.21: Intensity profile measurement at focus of f=6.5 m mirror with a 12-bit CCD camera. The horizontal and vertical line-out show the diameter is 310 μm at half-maximum.	47
Figure 3.1: Principle of a chirped mirror. Light with a long wavelength penetrates deeper into the multilayer structure and experiences a bigger group delay.	49
Figure 3.2: The adaptive phase modulator. The white-light from HC fiber were sent to the spatial light modulator. SH generation from a BBO was used for simultaneous MIIPS and FROG measurements. G1, G2: gratings, CLM1, CLM2: cylindrical mirrors. Figure adapted from Ref. [1]	51

Figure 3.3: The MIIPS traces (a) from the first iteration; (b) from the last iteration. Figure adapted from Ref. [1].	54
Figure 3.4: A 5 fs compressed pulse measured by the FROG. Figure adapted from Ref. [1].	55
Figure 3.5: Experimental setup of the low loss deformable mirror phase modulator. . . .	57
Figure 3.6: Effect of deformable mirror phase modulator pulse compression. Left (same displacement voltage applied to all actuators): splitted FROG structure implies strong satellite pulses due to high order phase distortion. Right (optimized deformable mirror actuator voltages): narrow shape FROG trace shows close to transform limited pulse duration.	58
Figure 3.7: A f-to-2f interferometer for measuring and stabilizing the CE phase of the amplified pulse.	62
Figure 3.8: CE phase control by shifting the grating separation.	63
Figure 3.9: CE Phase stabilization for FAST kHz stage.	65
Figure 3.10: Amplifier CE phase locking by grating shaking method.	66
Figure 3.11: Temporal evolution of the interference fringes as controlling the CE phase of the amplified laser pulses by changing the PZT set point.	67
Figure 4.1: Polarization gating setup and its field components.	70
Figure 4.2: The SH field breaks the driving field symmetry, and electron ionization occurs with one cycle separation instead of half cycle separation.	73

Figure 4.3: GDOG allows even less delay between two elliptically polarized pulses comparing to DOG due to the reduced driving field amplitude.	75
Figure 4.4: Attosecond pulse streaked spectrogram from 25 fs laser pulse.	77
Figure 4.5: The experimentally obtained (a) and retrieved (b) streaking traces from a 25 fs driving laser with argon as the generation gas. (c) The retrieved temporal pulse (black line) and phase (red dotted line). (d) The measured (blue dotted line) and retrieved spectrum (black line) and phase (red line). Figure adapted from Ref. [2].	78
Figure 4.6: ADK calculation for PG, DOG and GDOG as a function of input pulse duration. The calculation assumes laser intensity of $2.8 \times 10^{14} \text{W/cm}^2$ with Argon as the generation gas.	81
Figure 4.7: Streaked spectrograms for four different values of the input CE phase. Figure(a) is π , (b) is $\pi/2$, (c) is 0, and (d) is $3\pi/2$. Figure adapted from Ref. [3].	83
Figure 4.8: Streaked spectrogram from a CE phase unlocked pulse with the reconstructed temporal profile (solid line) and phase (dashed line). Figure adapted from Ref. [3].	84
Figure 4.9: The attosecond beamline. The closer chamber on the right side of the photo is the HHG generation chamber.	86
Figure 4.10: Chamber for TW beam focusing mirror and GDOG optics.	93
Figure 4.11: Filamentation induced by focusing 14 fs driving laser through the 10 cm long gas cell filled with Ar gas.	94

Figure 4.12: Setup for attosecond XUV generation and characterization. 95

Figure 4.13: Raw single-shot XUV spectrum captured by CCD camera. 96

Figure 4.14: Single-shot XUV spectra generated in argon under different gating conditions. 97

Figure 4.15: Oscilloscope signal of the XUV photodiode measurement for the GDOG-gated XUV spectrum. 98

LIST OF TABLES

Table 2.1: Performance of the kHz Amplifier	18
Table 2.2: Summary of Optical Mirrors for Laser Amplifier	37
Table 4.1: Gate Width for Generalized Double Optical Gating	82

CHAPTER 1: INTRODUCTION

When the laser was first invented in 1960 [4, 5], the pulse duration was 10 μ s. Significant progress has been made in developing shorter and more intense light sources. The pulse duration was reduced to picosecond time scales after the invention of Q-switching and mode locking technology. Femtosecond laser sources were developed after the discovery of broadband gain media such as dye and Ti:Sapphire. Today, pulses with duration less than 5 fs can be obtained from Ti:Sapphire laser systems. With the shortening of pulse duration, extra high peak power and intensity can be obtained. The boundary was further pushed by applying the chirped pulse amplification (CPA) technique to overcome the intensity limit due to optical damage [6, 7]. A decade later, gain narrowing in the amplifying media was compensated by using thin angle tuned etalons or birefringent filters, allowing for the generation of sub 20 fs TW pulses [8, 9, 10].

These powerful laser sources opened up a new field for ultrafast science: attosecond research. Attosecond pulse generation was first realized by the process of high order harmonic generation. When a laser is focused in a rare gas with an intensity of $\sim 10^{13} - 10^{14}$ W/cm², a series of odd order harmonics of the fundamental driving laser is produced. This laser like radiation – providing excellent temporal coherence with broad spectrum bandwidth – can be provided on a laboratory tabletop setup [11]. The story line of ultrafast physics and chemistry research has been rewritten thereafter.

1.1 High Harmonic Generation

From the microscopic single atom perspective, the process of HHG can be explained by a simple three-step model. When an intense laser is focused tightly onto a target material, the bound state

electron undergoes three phases, which individually are tunneling, acceleration and eventually recombination with its parent nucleus to emit XUV radiation [12, 13, 14]. The process is illustrated in Figure 1.1.

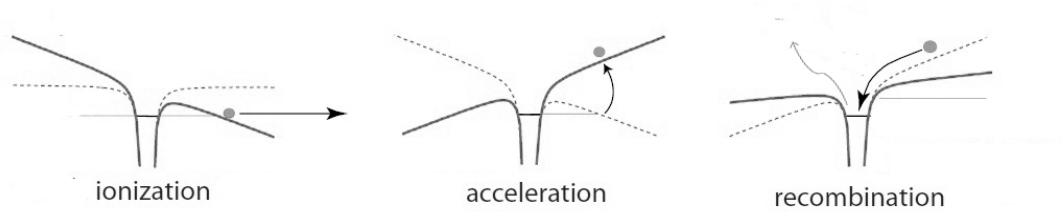


Figure 1.1: The 3-step model of HHG.

First, for HHG generation, gas phase targets (usually inert gas) are preferred due to the simplicity in the delivery and removal of the contamination. When the focused laser pulse intensity is 10^{13} W/cm² or over, the binding potential between the electron and its parent nucleus will be reduced. This modification from the oscillating laser electric field will grant the ground state bound electron the possibility of tunneling through the atomic potential well.

In order to tell if the target atom is ionized through the tunneling or the perturbative multi-photon process, the Keldysh parameter γ was introduced [15, 16, 17]:

$$\gamma = \sqrt{\frac{I_p}{2U_p}}, \quad (1.1)$$

where I_p is the ionization potential. U_p is the ponderomotive potential which is the cycle average kinetic energy of an electron in the laser field:

$$U_p = \frac{e^2 I}{2m_e \epsilon_0 c \omega^2}, \quad (1.2)$$

where m_e is the electron mass, e is the electron charge, ω is the laser frequency, and I is the laser intensity.

The Keldysh parameter γ was set up in such a way that it represents the ratio between the time required for the electron to tunnel out the potential barrier and the time during which the barrier is lowered by the laser field. When the Keldysh parameter is below 1, the ionization process is non-perturbative and the tunneling electron can be treated in a classical way.

Next, the freed electron will be pushed back by the laser's electric field after it changes its direction in one optical cycle. By Newton's law, we can calculate the kinetic energy of the returning electron is:

$$KE = U_p(1 + 2\cos^2(\omega t_0)), \quad (1.3)$$

where t_0 is the initial ionization time [18].

During the last step, the homecoming electron can recombine with the parent nucleus to release the accumulated kinetic energy as radiation in the XUV region. It was shown that the maximum kinetic energy the electron can gain is $3.17U_p$, thus the maximum photon energy possibly released is $E = I_p + 3.17U_p$, which is dependent on the target gas ionization potential, driving laser intensity and wavelength. The maximum kinetic energy sets the far end of the HHG spectrum which is the cutoff region in Figure 1.2.

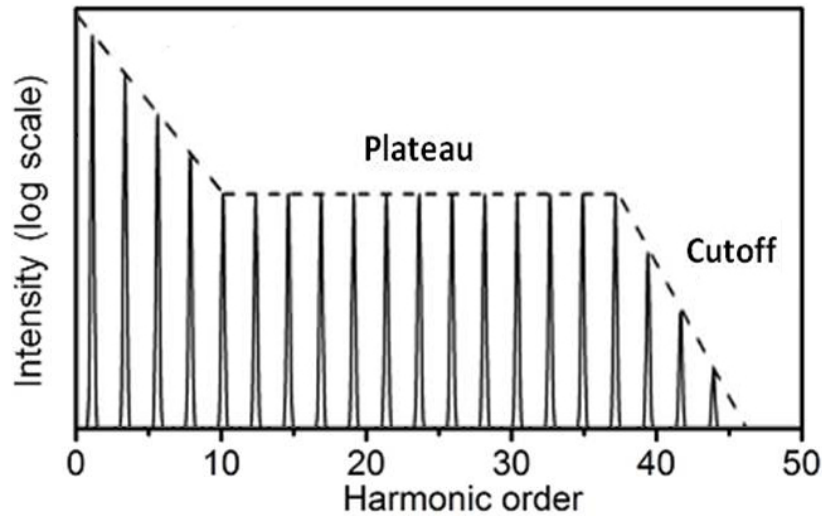


Figure 1.2: A typical HHG spectrum. After the fast decreasing of signal in the low energy region, a plateau with comparable strength was followed by an abrupt cutoff.

The HHG process can also be treated quantum mechanically based on the single active electron approximation [19, 20, 21]. However, the semi-classical 3-step model makes close enough predictions with easy to understand concepts.

On the other end, since HHG is a process involving a large amount of atoms with coherent stimulation from the driving laser, macroscopic nonlinear effects such as dispersion, absorption and ionization of the whole medium should also be taken into account in the theoretical model [22].

Another important aspect of the HHG process is phase matching, which strongly influences the HHG generation efficiency. Same as with frequency doubling second harmonic generation (SHG), phase matching in HHG requires the wave vector of the generated q th harmonic field (\mathbf{k}_q) to match

the wave vector of the fundamental laser field (\mathbf{k}_f):

$$\mathbf{k}_n = q\mathbf{k}_f. \quad (1.4)$$

In order to reach perfect phase matching, the wave vector mismatch $\Delta\mathbf{k} = \mathbf{k}_q - q\mathbf{k}_1$ should be equal to zero. The major terms contributing to phase mismatch for the q th harmonic generation are the material dispersion, focusing geometry, atomic dipole phase, plasma density, and any nonlinear effects [23]. The total result can be written as:

$$\Delta k = \Delta k_{disp} + \Delta k_{geom} + \Delta k_{dipole} + \Delta k_{plasma} + \Delta k_{other}. \quad (1.5)$$

The terms in Equation 1.5 can be used to cancel each other in order to reduce the total phase mismatch.

1.2 Isolated Attosecond Pulse Generation

During every laser cycle, the three step process occurs twice for a linearly polarized multi-cycle femtosecond laser pulse. Therefore, an attosecond pulse trains is generated with half cycle spacing between pulses [24, 25, 26]. The spacing between neighboring attosecond pulses in the train is typically 1.3 fs for the Ti:Sapphire driving laser case.

Isolated attosecond pulses are more desirable since they offer time resolution on the attosecond timescale. In order to generate isolated attosecond pulses, harmonics should be limited to generation only from half an optical cycle in a driving laser pulse.

Spectral filtering of high order harmonics by a few-cycle driving pulse was the first scheme realized

for producing an isolated attosecond pulse. Using this method, an isolated attosecond pulse as short as 80 as has been generated [27].

The HHG process has strong ellipticity dependence on the driving laser field. By controlling the ellipticity of the driving laser, the harmonic emission can be limited to the period when the laser is linearly polarized [24, 28]. For example, using the polarization gating technique, XUV emission can be confined to an isolated attosecond pulse with a broad and tunable bandwidth, producing pulses with 130 as duration [29].

1.3 Overview of Thesis

The goal of this work is to demonstrate a high intensity tabletop attosecond XUV laser source capable of generating isolated attosecond pulses at the μJ energy level.

First of all, a unique Ti:Sapphire chirped pulse amplifier laser system that delivers 14 fs pulses with over 300 mJ energy at a 10 Hz repetition rate is designed and constructed. The broadband spectrum extending from 700 nm to 900 nm was obtained by seeding a two stage Ti:Sapphire chirped pulse power amplifier with mJ level white light pulses from a gas filled hollow core fiber. It is the highest energy level a broadband pulse has ever been amplified by a chirped pulse amplifier up to current date.

Using this laser as the driving laser source, proper birefringent optics are employed to ensure isolated attosecond pulse generation using the generalized double optical gating method. Detailed gate width analysis of the ellipticity dependent pulse was performed. Calculation of electron light interaction dynamics on the atomic level was carried out to demonstrate the mechanism of isolated attosecond pulse generation.

Finally, a complete diagnostic apparatus was built to extract and analyze the generated XUV pulse in both the spectral and time domain. The result confirms that an extreme ultraviolet super continuum supporting 230 as isolated attosecond pulses at 35 eV was generated using the generalized double optical gating technique. The XUV pulse energy was ~ 100 nJ at the exit of the argon gas target.

1.4 Summary of My PhD Research

High harmonic generation driven by a high-intensity laser is currently the most efficient method for attosecond pulse generation. For this reason, it is hard to separate attosecond laser research from femtosecond laser development. When I joined the attosecond group in 2007, I began working towards improving the existing Kansas Light Source (KLS) laser system to facilitate attosecond research [30]. First, I improved the FROG setup in our lab to accurately measure pulse durations shorter than 5 fs. This work was published together with my work on adaptive phase modulation, which will be described in Chapter 3 of this thesis [1, 31]. Later, I instituted spectral filtering within the amplification stage using birefringent plates, which allowed for shorter output pulse durations from the KLS CPA system. After successfully reducing the 1 kHz, 2 mJ pulse from its original 35 fs to 23 fs, our group was able to demonstrate isolated attosecond pulse generation using driving laser pulses directly from the CPA system [32, 33, 34, 3, 35, 2].

After our group moved to the University of Central Florida in 2010, my research pursuits changed direction. Instead of making minor alterations to a pre-standing laser system, I played the leading role in establishing a whole new carrier envelope (CE) phase-stabilized, kHz-repetition rate laser system [36], which quickly became the workhorse of our attosecond research [37, 38, 39]. My focus has recently shifted further to developing a high-flux attosecond source with a uniquely-built 20 TW, 15 fs, 10 Hz laser system [40]. Beyond the expected logistical difficulties inherent to large-

scale system design, I have successfully addressed various technical challenges while building this 20 TW laser, including feedback-optimized adaptive phase modulation, multilayer mirror and filter coating design, XUV end-station and diagnostic implementation, and laser-ablated debris elimination.

CHAPTER 2: LASER FACILITY AT INSTITUTE FOR THE FRONTIER OF ATTOSECOND SCIENCE AND TECHNOLOGY LAB

The laser system for the high-flux attosecond pulse generation is located in the Institute for the Frontier of Attosecond Science and Technology (iFAST) laboratory at the Physical Science facility in the University of Central Florida [36].

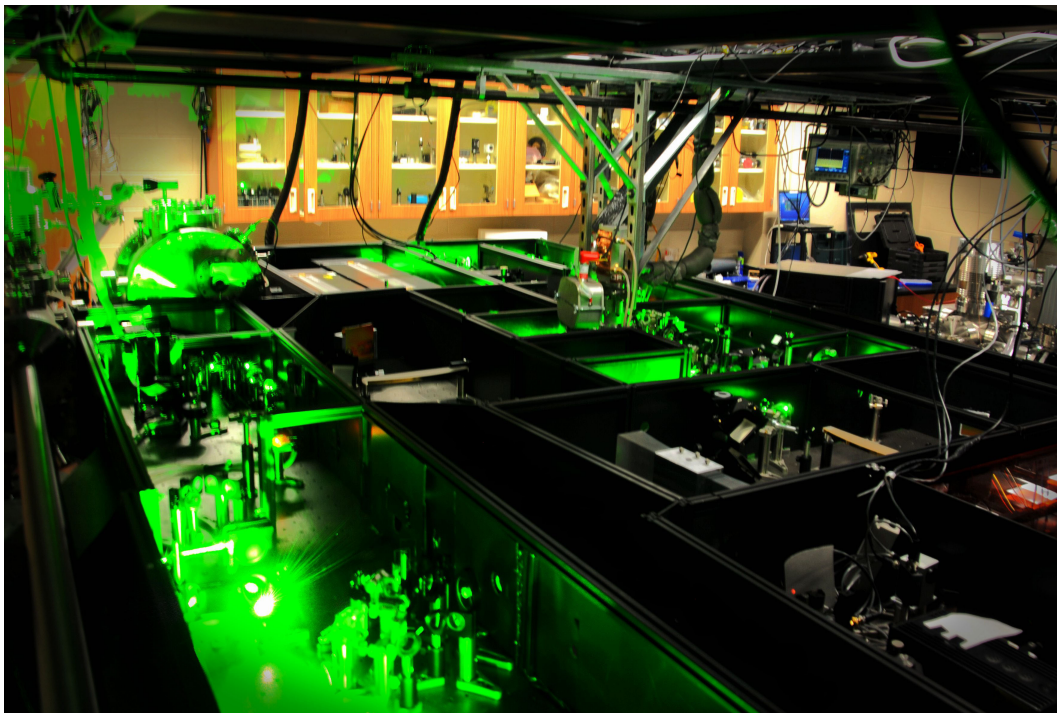


Figure 2.1: Photo of iFAST lab laser system.

This uniquely designed laser system – capable of delivering sub-15 fs, 20 TW pulse at a 10 Hz repetition rate – was put to use for attosecond science research beginning in early 2013. A high-gain

amplifier operating at a kHz repetition rate provides over 10^6 times amplification in order to raise the seeding pulse energy from nanojoule to millijoule level. Two consecutive power amplifiers working at 10 Hz are applied to boost the energy to joule level (Figure 2.1).

2.1 Chirped Pulse Amplifiers

The design of a tabletop terawatt laser systems usually starts with the seeding pulse from a mode-locked Ti:Sapphire oscillator. However, since the laser pulse energy from femtosecond oscillators is on the order of nanojoules, a gain of 10^6 or higher is required for the pulse energy to reach the level appropriate for attosecond pulse generation. Two major different types of systems are employed to carry out the amplification process: chirped-pulse amplification (CPA) [41, 42, 43] and optical parametric chirped-pulse amplification (OPCPA) [44, 45, 46]. While the option of using OPCPA offers the advantage of few-cycle laser pulses with scalable energy, the specialized pump laser technology for OPCPA is still underdeveloped. On the other hand, widely available Ti:Sapphire-based chirped-pulse amplification (CPA) laser systems are capable of achieving peak power of 100 TW or above, but their output pulses contain too many optical cycles to be used with even the least-restrictive gating schemes. In this work, a uniquely designed CPA amplifier system that delivers 14 fs, 20 TW pulses with a 10 Hz repetition rate is developed for generating high-flux isolated attosecond pulses.

2.2 Pulse Stretching and Compressing

Since the discovery of Kerr lens mode locking (KLM), ~ 5 fs pulses can be generated in Ti:Sapphire lasers [47, 48]. For femtosecond pulse amplification, the intensity of an amplified pulse will reach the damage threshold of the laser gain media before the amplification reaches saturation if the

pulse duration is too short. In order to efficiently transfer energy to pulses, the chirped pulse amplification technique is commonly used with high-power ultrafast laser systems. In a CPA system, femtosecond pulses are stretched by many orders of magnitude before undergoing the amplification process, as illustrated in Figure 2.2. Usually, the intensity is reduced by its long pulse duration so the saturation fluence of Ti:Sapphire can be reached before any damage happens to the gain media or other optics. This technique was first used on the radar microwave region until later applied to the laser [49, 7].

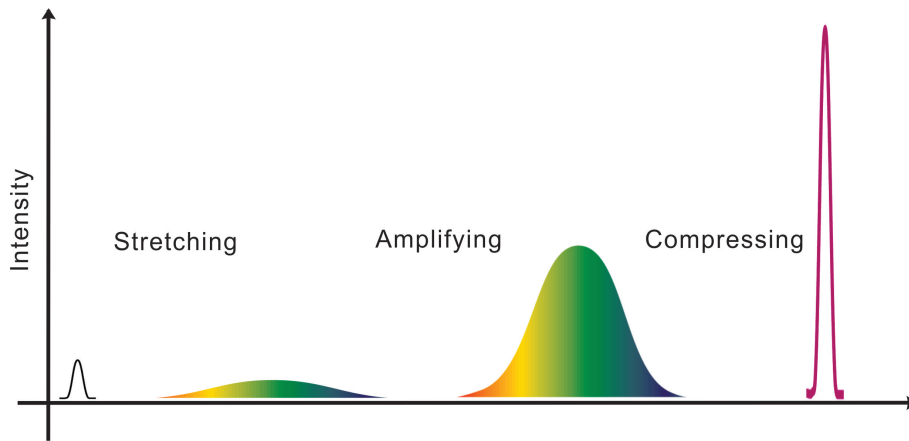


Figure 2.2: The temporal shape of a pulse undergoing a chirped-pulse amplification process.

2.2.1 *Stretcher and compressor*

To reduce the amplified beam intensity below the damage threshold, the stretched pulse duration should be at ~ 100 ps level. Therefore, over 10^4 times stretching of a femtosecond pulse is necessary, and large dispersion should be introduced. For example, to stretch an 800 nm, 15 fs transform-limited laser pulse to 300 ps, a group-delay dispersion of 1.8×10^6 fs² is required. In

order to introduce dispersion this large, a grating-pair based stretcher and compressor are preferred instead of a prism pair and glass compressor (Figure 2.3).

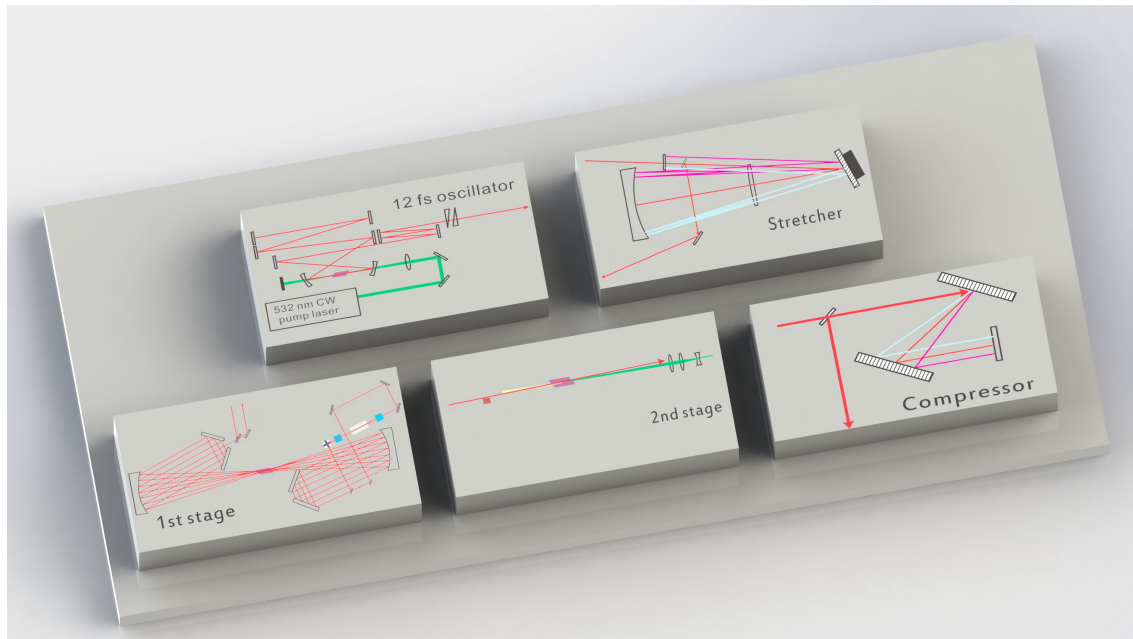


Figure 2.3: The block diagram of kHz laser

The pulse stretcher uses a telescope to create negative grating displacement. For example, in a Martinez stretcher, the dispersion is controlled by the effective distance between the second grating and the image of the first grating [50]. For different wavelengths passing through the stretcher, they are spectrally dispersed, which requires the beam to pass the stretcher for a second pass to reverse the dispersion process. The beam path for long wavelength components inside the stretcher is shorter than that of the short wavelength components. Therefore, the dispersion introduced by a pulse stretcher is positive [51]. The dispersion introduced by the pulse compressor is the exact same amount as the pulse stretcher if it is designed with same incident angle and displacement for

the gratings. The dispersion can be expressed as a function of wavelength λ :

$$\phi(\lambda) = 2 \times \frac{4\pi L}{\lambda} \sqrt{1 - \left(\frac{\lambda}{d} - \sin(\theta_{in})\right)^2} \quad (2.1)$$

where L is the grating separation, d is the spatial period of the grating groove, and θ_{in} is the incident angle [52]. The pulses are eventually compressed back to near transform-limited pulse duration to produce high intensity by introducing equivalent amount of dispersion with opposite sign.

2.2.2 *Multipass amplifier vs. regenerative amplifier*

A possible alternative to a multipass amplifier is a regenerative amplifier [53, 42, 54]. Amplification inside a regenerative amplifier is achieved by trapping the seed pulse in a laser resonator. The seed pulse stays in the cavity until it extracts all of the energy stored in the amplification medium. Pulse trapping and dumping is done using a polarizer and a Pockels cell, which works like the optical switch.

Figure 2.4 shows the layout of a regenerative amplifier (Legend Elite HE, Coherent Inc.) [55]. This regenerative amplifier was seeded with the 3 nJ, sub-7 fs output from a commercial oscillator (Rainbow from Femtolasers GmbH). The first amplification stage consists of a regenerative amplifier with 14 round trips to amplify the pulse energy to 4 mJ. The second stage is a single pass amplifier for doubling the pulse energy to 8 mJ. The Ti:Sapphire crystals in both stages are thermoelectrically cooled (TEC) to -12°C . Both stages are pumped by a 527 nm, 45 mJ pump laser running at 1 kHz (Evolution HE, Coherent Inc.). After the grating compressor, the laser system delivers laser pulses up to 6 mJ with a measured pulse duration of 30 fs. An angle tuned etalon is inserted between the oscillator and amplifier to suppress the gain narrowing effect in the amplification process [56].

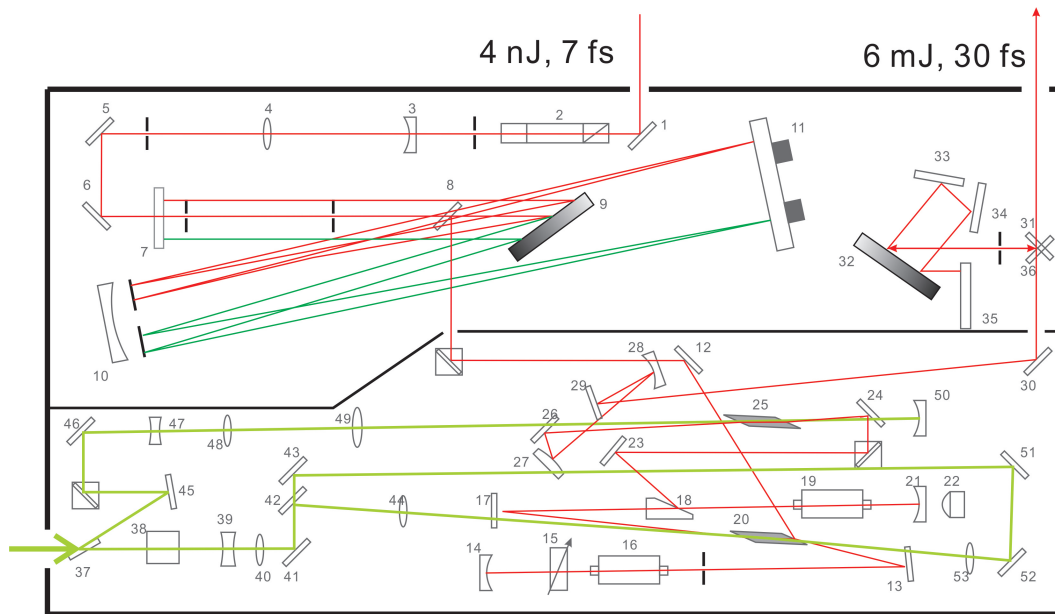


Figure 2.4: Schematic of a typical regenerative amplifier.

A regenerative amplifier simplifies the alignment requirement of a multipass amplifier and is also usually more compact. However, since every round trip the seed pulse passes through the Pockels cell in the regenerative amplifier, the material dispersions in multipass amplifiers is higher than in regenerative amplifiers. It is therefore easier to generate shorter femtosecond pulses with a multipass configuration.

In our case, the multipass layout is more preferable not only because we can achieve the shortest possible pulse duration by compressing the amplified pulse closer to its transform limited pulse duration, but also because the beam passes are well separated inside the multipass cavity so any diagnosis on the laser condition such as ASE level and signal gain can be performed easily to make sure the laser system is operating at peak performance.

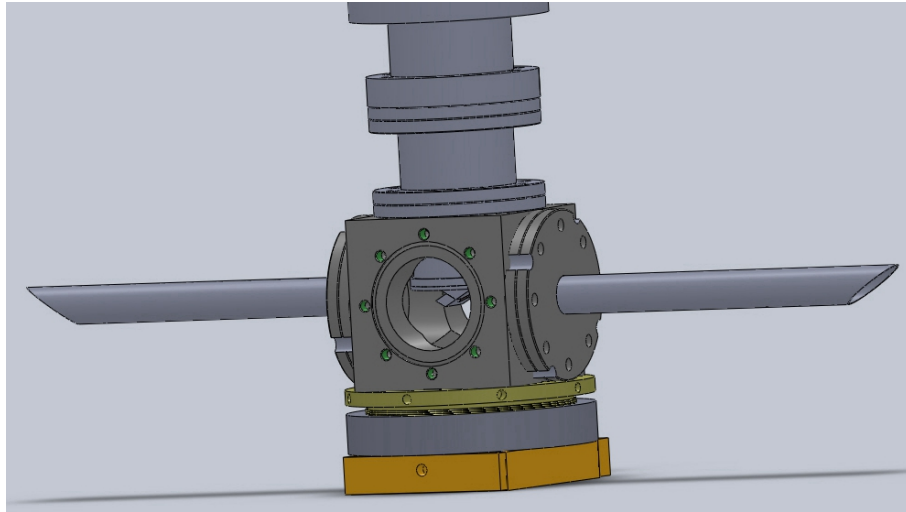
2.3 iFast 20 fs, 3.5 mJ 1 kHz Multipass CPA System

Our iFAST laser system starts with a 2-stage kHz system that delivers 20 fs, 3.5 mJ pulses at a 1 kHz repetition rate. Twelve fs pulses from a commercial oscillator (Femtsource Pro) are used to seed the amplifier [57]. Mode-locking allows for ~ 5 nJ energy output pulses at a repetition rate of ~ 80 MHz. The temporal separation of pulses in the pulse train is ~ 12 ns.

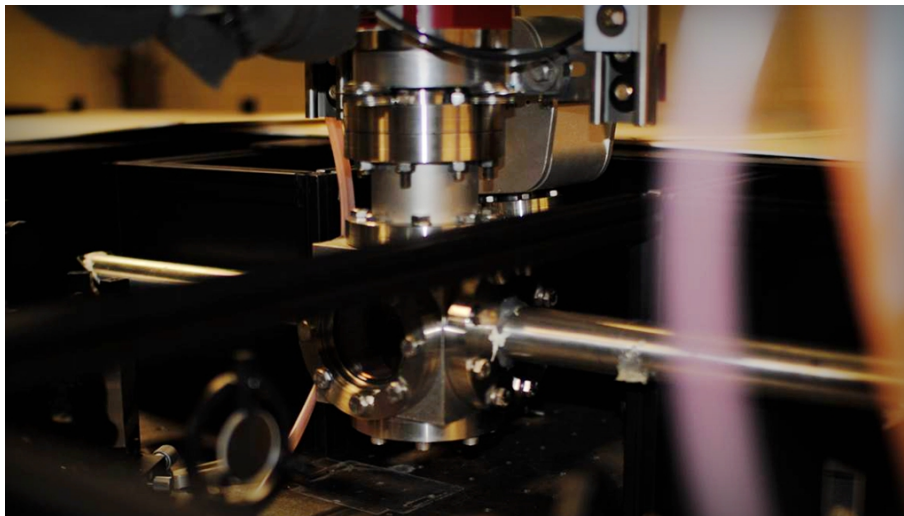
After passing through a beam splitter which reduces their magnitude by half, the 12 fs pulses are temporally stretched to 100 ps by an Öffner-type stretcher. The stretched pulses are amplified to 3 mJ through a 14-pass amplifier plus 1-pass power amplifier, as shown in Figure 2.6. A total gain of over one million times was obtained by geometrically arranging multiple passes of the seed beam through the Ti:Sapphire gain medium [58, 59, 60]. This was realized by using a pair of cavity mirrors with ROC = 2000 mm and four 45° folding mirrors. After the first 7 passes, the seed beam is directed out of the cavity for amplified spontaneous emission reduction by applying a 10 ns gate through a Pockels cell [61]. In order to separate the second 7 passes from the first ones, the beam direction is raised to a higher plane when the seed pulse is re-injected back to the amplifier. The pulses goes through the 1-pass power amplifier to double the pulse energy before final compression.

Because the quantum efficiency of the pump to signal conversion is less than 70%, the residual heat from the amplifying process will cause serious thermal lensing and other thermal effects such as thermal stress or birefringence. In order to eliminate thermal lensing and heat management issues, both stages are cryogenically cooled to below 100 K. Upon cooling from 300 K to 77 K, the thermal conductivity of the Ti:Sapphire crystal dramatically increases and its $\partial n/\partial T$ decreases [62, 63]. The cryogenic solution suppresses not only thermal lensing but also higher-order aberrations and distortions, thus simplifying the amplifier design and making the alignment requirement easier and independent of the pump power [64, 65, 66]. The cryogenic cooling was realized by attaching

the Ti:Sapphire crystal to the copper cold finger of a pulse tube based cryogenic cooler [67]. A 1 mm thick indium sheet was placed between the crystal and the copper in order to provide a good thermal contact.



(a) Design drawing of kHz Ti:Sapphire crystal vacuum chamber.



(b) Photo of vacuum chamber containing Ti:Sapphire crystal cooled at cryogenic temperature.

Figure 2.5: Vacuum chamber of kHz Ti:Sapphire crystal.

The final output pulses measured 20 fs with 3.5 mJ pulse energy after passing through a grating compressor. The grating compressor is built with two mechanically ruled gratings with line density of 1200 l/mm, optimized for a center wavelength of 760 nm [68]. During the kHz amplification stages, the gain narrowing effect is partially reduced by inserting gain narrowing compensation filters in the early passes of the 14-pass amplifier.

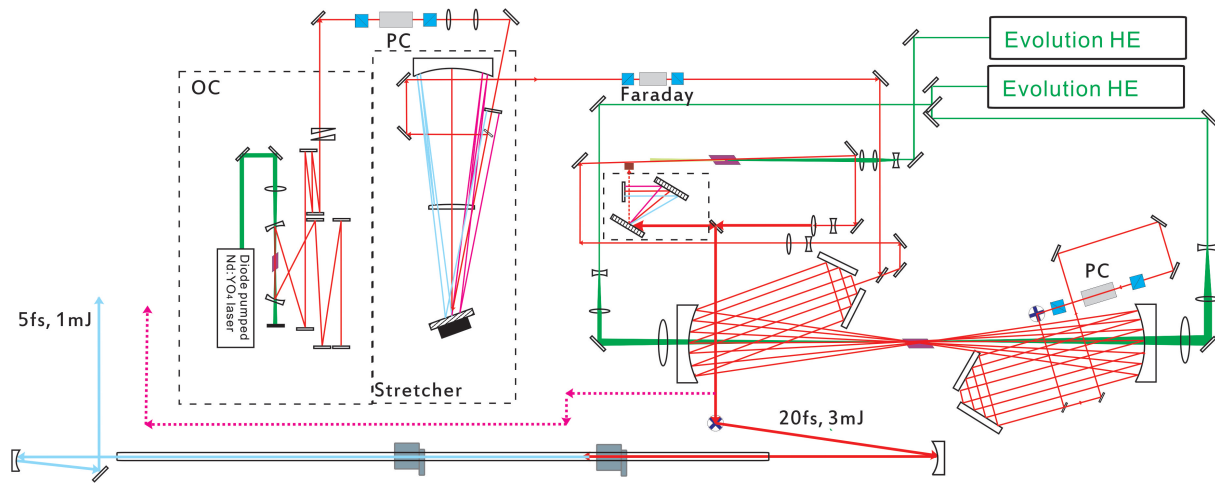


Figure 2.6: Schematic of kHz amplifier system.

In table 2.1, a summary of the pulse properties at different stages of amplification is given.

Table 2.1: Performance of the kHz Amplifier

Property	Value
Seeding pulse duration	12 fs
Seeding pulse energy	2 nJ
Stretched pulse duration	100 ps
1st stage passes	14
1st stage gain	≥ 3000000
1st stage temperature	~ 90 K
Number of anti-gain-narrowing filter used	3
2nd stage passes	1
2nd stage gain	≥ 2
2nd stage temperature	~ 90 K
ASE level	$\leq 5\%$ with seed blocked
Compressed pulse energy	3.5 mJ
Compressed pulse duration	20 fs
Power rms	$\leq 1\%$

2.4 20 TW, 14 fs, Multi-Pass CPA System

In order to scale the isolated attosecond pulse energy to the μJ level, driving lasers with higher power are required. In generalized double optical gating (GDOG), the laser field is manipulated to be linearly polarized only within a single-optical-cycle “gate” at the center of the pulse, whereas the leading and trailing edges are elliptically polarized. A linearly-polarized second-harmonic

field is added to break the field symmetry, restricting attosecond pulse generation to a single event within the gate. While the GDOG method can be applied to both few and multi-cycle lasers, the driving laser pulse duration remains a key parameter, as only the energy contained in the linearly-polarized portion of the laser contributes to the generation of the isolated attosecond pulse. If the pulse duration is too long, the leading cycles of the pulse pre-ionize many of the available atoms before the arrival of the linear gated cycle, thus reducing the conversion efficiency. This effect can be mitigated by keeping the duration of the driving laser pulse as short as possible. To this end, we developed a Ti:Sapphire laser system optimized to provide both high-energy (300 mJ) and short-duration (14 fs) pulses for implementing GDOG.

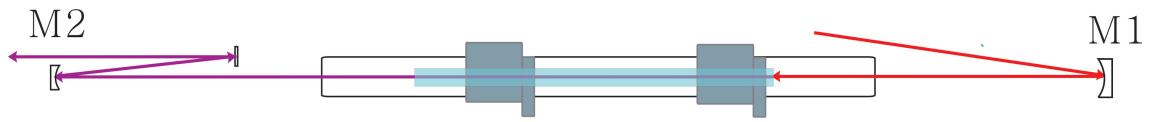
This 20 TW laser system can be divided into three parts for the ease of explanation: the kHz CPA amplifier, hollow-core fiber white light generation, and the 10 Hz power CPA amplifier.

2.4.1 White light generation in hollow-core fiber

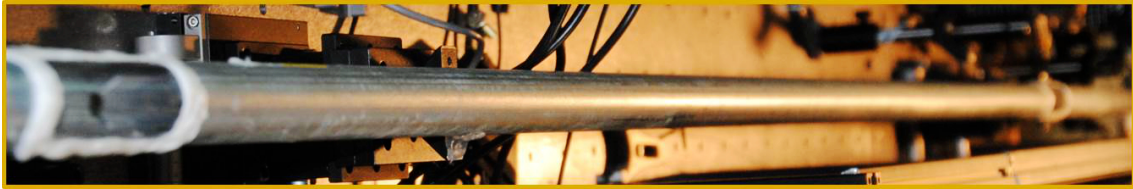
The kHz multi-pass amplifier system delivers pulses close to the transform limit of 20 fs (Sec. 2.3). Borosilicate glass hollow fibers of 150 cm length and 450 μm capillary radius are used [69, 70, 71, 72]. The fiber was kept straight in an aluminum V-groove bar, which was then placed in a pressurized 1 inch diameter steel tube. This is visible in Figure 2.7 (b). The laser beam is focused into the chamber by a 2000 mm focusing mirror through broadband anti-reflection (BBAR) coated 1 mm thick fused silica windows. The vacuum tube can be filled with several gases such as argon, krypton, and helium at different pressures. The overall throughput of the hollow-core fiber system – including coupling, fiber losses, and some residual reflection losses at the anti-reflection-coated windows – is 50% – 60%. The exiting beam is then collimated by a silver coated concave mirror with a radius of curvature of 3000 mm.

The overall bandwidth of hollow-core fiber output supports pulses shorter than 5 fs in duration.

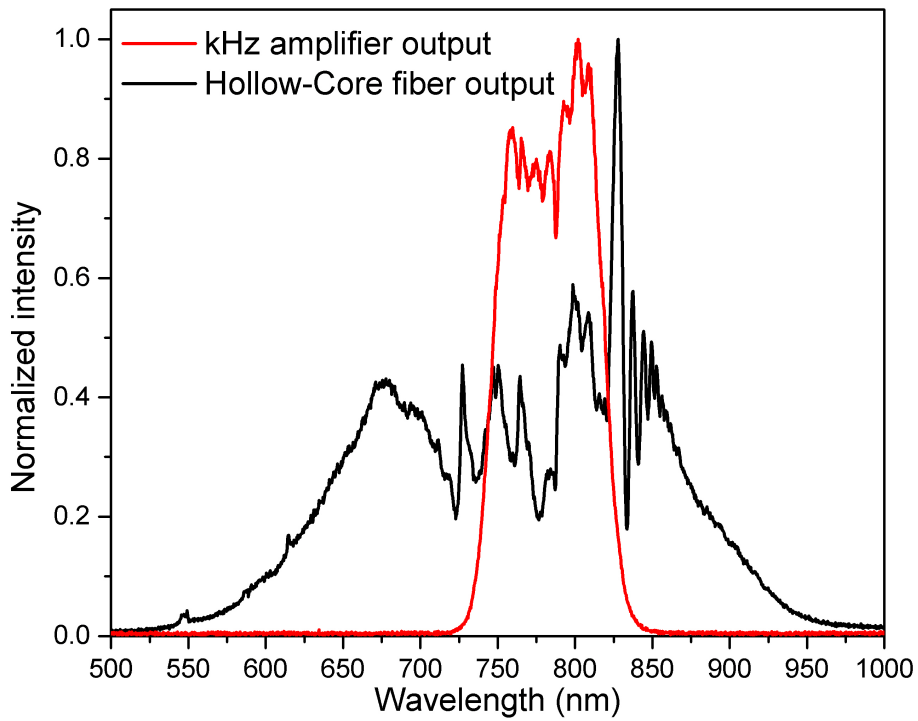
Figure 2.7 (c) shows the actual effect of spectrum broadening in the hollow-core fiber.



(a) Schematic diagram of the experimental setup. M1 is an 800 nm dielectric coated mirror of 2000 mm focal length, M2 is a silver-coated mirror with 1500 mm radius of curvature.



(b) Photo of hollowcore fiber.



(c) Laser spectrum before (red) and after hollow-core fiber (black).

Figure 2.7: Hollowcore fiber for spectrum broadening.

Spectral broadening of high energy femtosecond pulses in bulk materials usually leads to nonuniform transverse self-phase modulation due to the nonuniform transverse intensity profile. On the other hand, spectral broadening is achieved by self-phase modulation in a hollow fiber made of glass and filled with noble gases at high pressure. This allows for single mode guiding elements of large mode diameter, making the technique suitable for large pulse energies.

Wave propagation along hollow fiber guides can be thought of as occurring through grazing incidence reflections at the dielectric inner surface. Since the losses caused by these multiple reflections greatly discriminate against higher order modes, only the fundamental mode can propagate in a sufficiently long fiber. The maximum broadening $\delta\omega_{max}$ for a Gaussian pulse after a length l , at either the low or high frequency side of the spectrum, is given by:

$$\delta\omega_{max} = 0.86\gamma P_0 z_{eff}/T_0, \quad (2.2)$$

where $z_{eff} = [1 - \exp(-\alpha l)]/\alpha$, with α given by

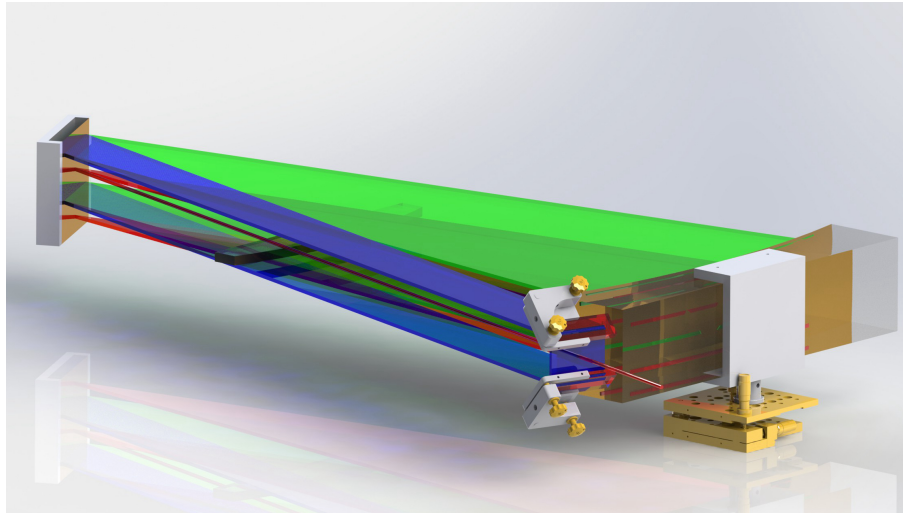
$$\frac{\alpha}{2} = \left(\frac{2.405}{2\pi}\right)^2 \frac{\lambda^2}{2a^3} \frac{\nu^2 + 1}{\sqrt{\nu^2 - 1}}. \quad (2.3)$$

Here λ is the laser wavelength in the gas medium and ν is the ratio between the refractive indices of the external glass and internal gas media. The nonlinear coefficient γ is given by $\gamma = n_2\omega_0/cA_{eff}$, where ω_0 is the laser central frequency, n_2 is the nonlinear index coefficient and A_{eff} is the effective mode area.

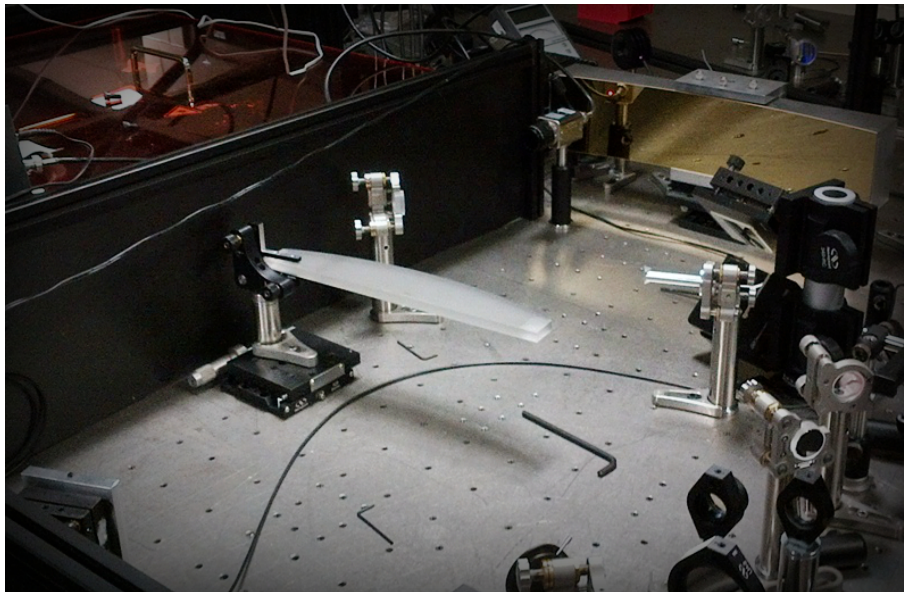
2.4.2 300 ps Öffner type stretcher

Pulse stretching for 14 fs, 20 TW level CPA amplification is challenging: the spectral width of the hollow-fiber output pulse is relatively wide (~ 200 nm), and the chirped pulse duration for 20 TW amplification requires pulse stretching beyond 100 ps to reduce the possibility of damaging laser optics. A good pulse stretcher needs to keep the output beam wavelength dependent distribution and divergence small by reducing the aberration of the telescope. The Öffner-type telescope was reported to have relatively small aberration which can be directly translated into spectral phase distortions [73, 74, 75]. The generation of 20 fs, 1 TW pulses with a 1 kHz repetition rate using an Öffner-type stretcher was reported in 2000 [10]. The Öffner-type pulse stretcher we used for our 10 Hz amplifier system has a single grating design consisting of a concave mirror and a convex mirror. Figure 2.8 (a) shows the schematic of the pulse stretcher.

Our test result shows the aberration of this telescope is relatively small. The dispersion introduced by the stretcher can be mostly compensated by compressor, which means this stretcher design is suitable for our CPA system having small material dispersions.



(a) Schematic of Öffner stretcher.



(b) Laboratory picture of 1000 mm long, 600 mm wide, 200 mm tall Öffner stretcher.

Figure 2.8: Öffner-type stretcher for >200 nm, 300 ps pulse stretching.

For an Öffner-type telescope, the foci of the concave mirror and the foci of the convex mirror coincide at the same spot, however, it is not the same case for an aberration-minimized Öffner-

type stretcher. This is because the object needing to be imaged – which is the grating in the case of an Öffner-type stretcher – is no longer at the focus of concave mirror but closer in order to introduce positive phase chirp. In order to reduce the aberration, the curvature of the convex mirror needs to be slightly increased. In our case, the concave mirror has a radius of curvature of 1000 mm, so a 500 mm curvature is needed for the convex mirror of the Öffner-type telescope, but the ray tracing result showed that an optimized radius of curvature of 505 mm will reduce the output beam wavelength dependent distribution and divergence to a minimum. In the actual alignment, the distance between the concave mirror and the grating is 900 mm, and the 505 mm curvature convex mirror location was tuned by examining the far field beam profile.

Because of the bandwidth requirement of the output seed pulse, a 110 mm × 110 mm holographic master grating with a groove density 1400 l/mm was used as the diffractive element for the stretcher. A 600 mm long by 100 mm wide gold-coated concave mirror and 300 mm long, 10 mm wide convex mirror are used to provide high reflection efficiency. The overall throughput of the stretcher is above 30%. Special care was taken to provide long term and short term stability for future CE phase stabilization experiments.

2.4.3 Two-stage multipass amplifier

The white-light continuum generated from the hollow-core fiber has a spectrum from 550 nm to 950 nm. The center mode of the spectrally-broadened pulses is used to seed the second CPA [76]. Spectra from various stages of the laser are shown in Figure 2.9.

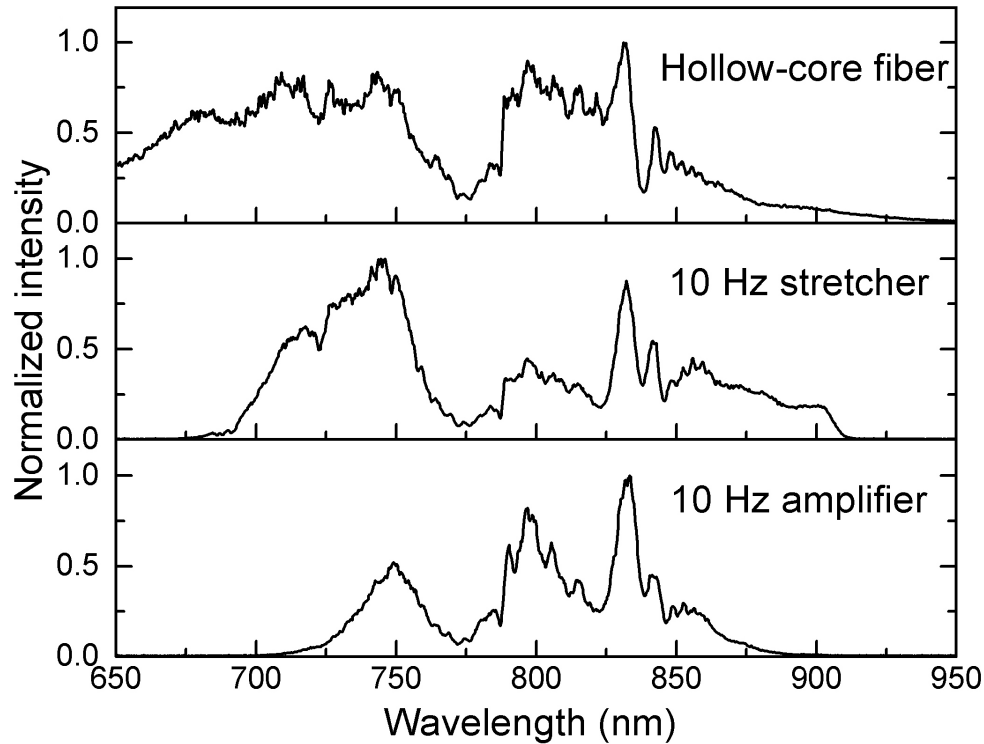


Figure 2.9: Schematic of 1st stage amplifier system.

After the Öffner stretcher, the 300 ps, 0.2 mJ positively-chirped pulses are then amplified to 30 mJ in a five-pass amplifier operating at 10 Hz. This Brewster-cut Ti:Sapphire crystal is pumped from both sides by relay-imaged portions of a Q-switched frequency-doubled Nd:YAG laser (Quanta Ray Pro 350). Specially-designed filters with a transmission minimum near 780 nm are inserted into the first three passes to alleviate gain-narrowing effects in this stage [77].

The second stage power amplifier employs a large-area, flat-cut Ti:sapphire crystal, which is pumped on one side by the remainder of the first-stage pump laser and on the other side by the full energy of another Nd:YAG laser (Quanta Ray Pro 350) with high M^2 factor. Instead of relay imaging the pump laser beams to the laser crystal, two diffractive optical elements (DOE) are used

for beam homogenization [78]. Homogenizing the profiles of the pump beams guarantees no “hot” structures are generated in the NIR pulse during amplification [79]. The clear aperture of the DOEs is 25 mm and they are anti-reflection coated for 532 nm with an overall efficiency >80%. The first pass pump absorption is 90%, with a pumped area of 10 mm diameter.

Both stages are water-cooled to room temperature, while divergent lenses are used to compensate the thermal lens. The energy of the amplified pulses can reach up to 700 mJ. The spectrum of these pulses extends from 700 nm to 900 nm, which supports 12.2 fs transform-limited pulses.

2.4.4 Numerical analysis of the 2-stage amplifier

Theoretical works that investigated spectral gain narrowing and gain saturation have been published in the past [53, 80]. The energy transport equations can be simplified as [81]:

$$I_{out}^{(n)}(t) = G^{(n)}(t)I_{in}^{(n)}(t)(1 - l), \quad (2.4)$$

where $I_{in}^{(n)}(t)$ is the input intensity and $I_{out}^{(n)}$ is the output intensity for the n th pass of the CPA amplifier and l is the loss factor. The n th pass instantaneous gain $G^{(n)}(t)$ is:

$$G^{(n)}(t) = \frac{G_0^{(n)}}{G_0^{(n)} - (G_0^{(n)} - 1)e^{-J_{in}^{(n)}/J_{sat}}}, \quad (2.5)$$

where $G_0^{(n)} = G^{(n-1)}(t_{end})$ is the final value of $G^{(n-1)}(t)$ in the last pass calculation, $J_{sat} = \hbar\omega/\sigma$ is the saturation fluence, $J_{in}^{(n)}(t)$ is the time-dependent energy fluence which is the integral of $I_{in}^{(n)}(t)$ to the present time:

$$J_{in}^{(n)}(t) = \int_{-\infty}^t I_{in}^{(n)}(t)dt. \quad (2.6)$$

The input intensity for the n th pass should be the output intensity for the $n - 1$ th pass:

$$I_{in}^{(n)}(t) = I_{out}^{(n-1)}(t). \quad (2.7)$$

The same is done for the fluence:

$$J_{in}^{(n)}(t) = J_{out}^{(n-1)}(t). \quad (2.8)$$

Solving Equations 2.4-2.8 gives the gain saturation in every single pass.

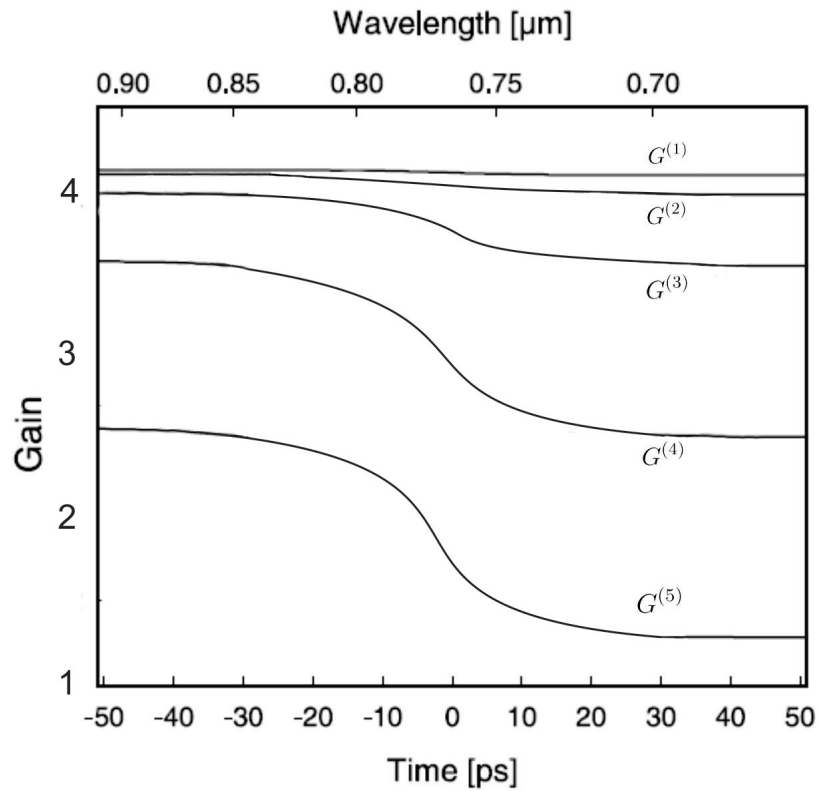


Figure 2.10: Instantaneous gain $G(t)$ for the five-pass amplifier stage.

Figure 2.10 shows the instantaneous gain for the five individual passes in the 1st 10 Hz amplifier

stage. The wavelength dependent gain is also displayed. Since the pulse was positively stretched in chirped pulse amplification, spectral red-shifting caused by the gain saturation can easily be understood from the same figure.

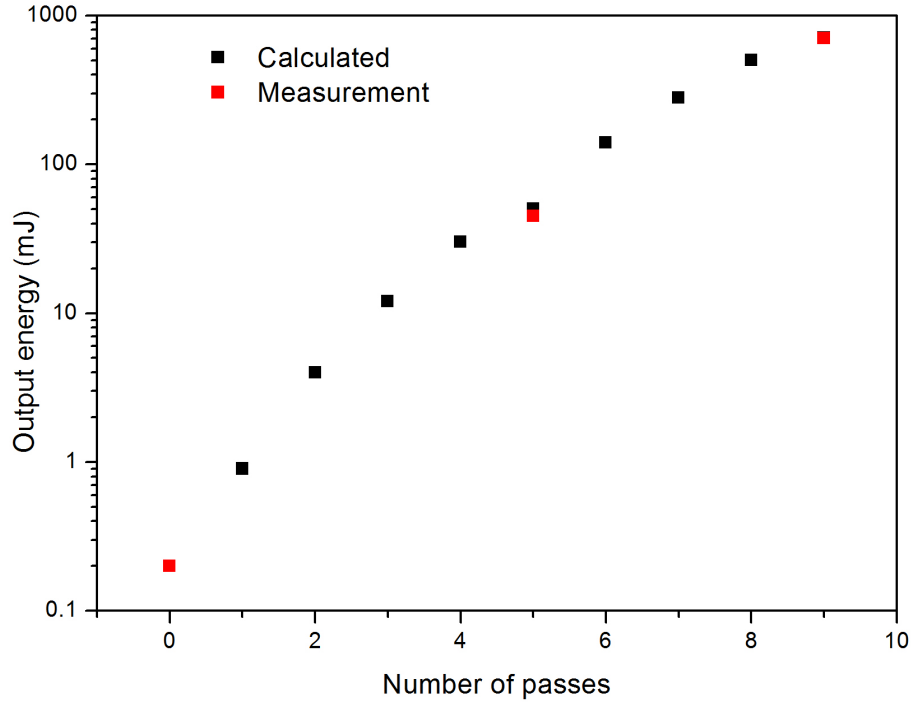


Figure 2.11: Output energy as a function of pass number.

Figure 2.11 shows the calculated output energy for the total 9 passes of the 2nd CPA system. The seed energy and the energy after each amplifier is shown for comparison.

In the frequency domain, the atomic gain coefficient $\alpha_m(\omega)$ due to the atomic transition is given by [80]

$$\alpha_m\omega = \frac{1}{2}\sigma N \frac{1}{1 + [2(\omega - \omega_a)/\Delta\omega_a]^2}, \quad (2.9)$$

where ω_a is the atomic transition frequency, $\Delta\omega_a$ is the atomic linewidth, σ is the emission cross section, and N is the population inversion density. The small signal power gain is:

$$G(\omega) = \exp(2\alpha_m(\omega)l) = \exp\left(\sigma Nl \frac{1}{1 + [2(\omega - \omega_a)/\Delta\omega_a]^2}\right). \quad (2.10)$$

For the multipass amplification, the output spectrum $I_{out}^{(n)}(\omega)$ with the input spectrum $I_{in}^{(n)}(\omega)$ and the gain $G^{(n)}(\omega)$ for the n th pass is:

$$I_{out}^{(n)}(\omega) = G^{(n)}(\omega)I_{in}^{(n)}(\omega). \quad (2.11)$$

The form of final amplified pulse spectrum $I_{out}(\omega)$ with regard to the seed pulse spectrum $I_{in}(\omega)$ is given by:

$$I_{out}(\omega) = I_{in}(\omega) \prod G^{(n)}(\omega). \quad (2.12)$$

Taking account of the gain saturation as shown in Figure 2.10, the amplified pulse spectra for the 2-stage multipass amplifier was calculated with four spectral shaping filters inserted. Figure 2.12 shows the calculated and measured amplified pulse spectrum. As the result of starting with high energy broadband HC fiber output as the input pulse together with multiple anti-gain-narrowing filters during the amplification process, the spectrum between 700 nm to 900 nm was well preserved after amplification to joule-level pulse energy. The good agreement between the calculated and experimental spectra validates this calculation method.

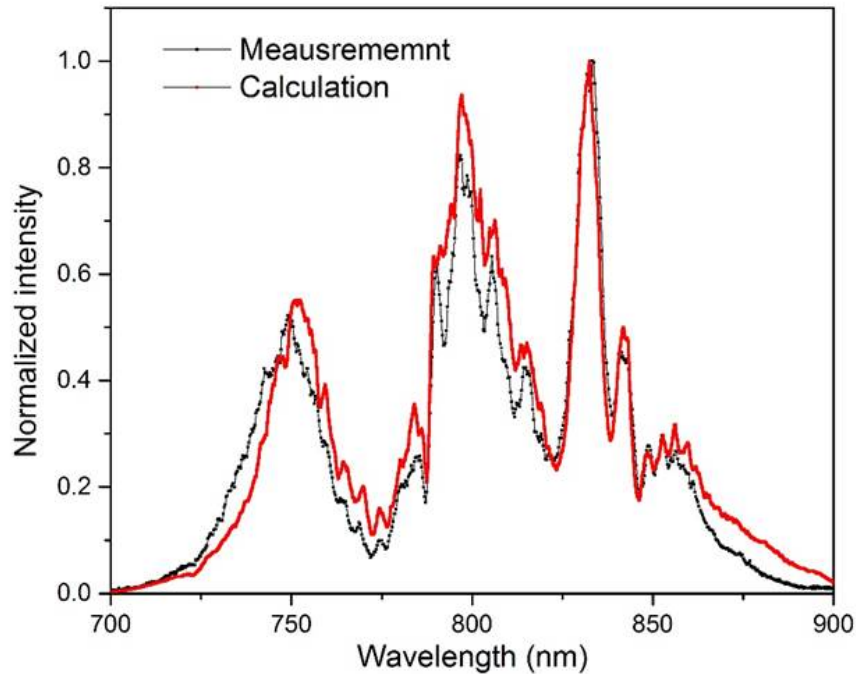


Figure 2.12: Calculated and experimental spectra for 2nd CPA stages seeded with white light pulse from HC fiber.

2.4.5 Gain narrowing compensation filter

Gain narrowing has long been a problem in CPA systems where the seed beam passes through the Ti:Sapphire gain medium many times to achieve sufficient amplification [82]. Since the Ti:Sapphire single pass gain is a Gaussian shaped curve centered at 800 nm at room temperature (780 nm for cryogenically cooled crystal) 2.13, the repeated passes result in a narrowed output spectrum which limits the compressed pulse duration, eventually reducing the peak intensity and the possible utility of the pulses.

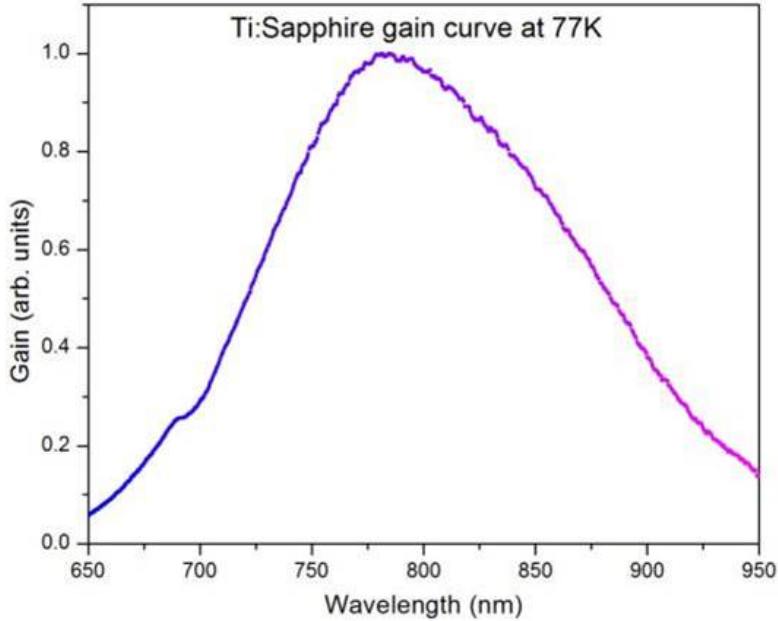


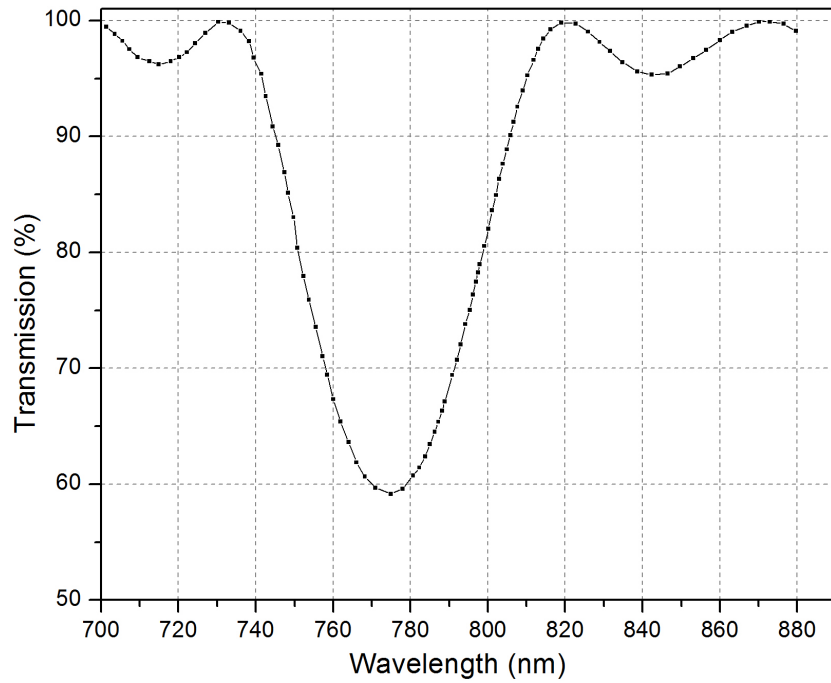
Figure 2.13: Gaussian shaped gain curve of Ti:Sapphire crystal at cryogenic temperature.

In the past, angle tuned etalons [56], birefringent filters [8] and dielectric multilayer filters [81, 83] have been used to flatten the gain shape. However, the gain shape results achieved by etalons or birefringent filters are not ideal, since they cannot completely compensate for the Ti:Sapphire gain shape. More importantly, for power amplifiers, whose later passes usually operate near saturation, etalons or birefringent filters usually dig too big of a spectral hole, which degrades the final output spectrum. In many cases of CPA development, this was the reason filters were included only in earlier passes but not in later passes [8, 84].

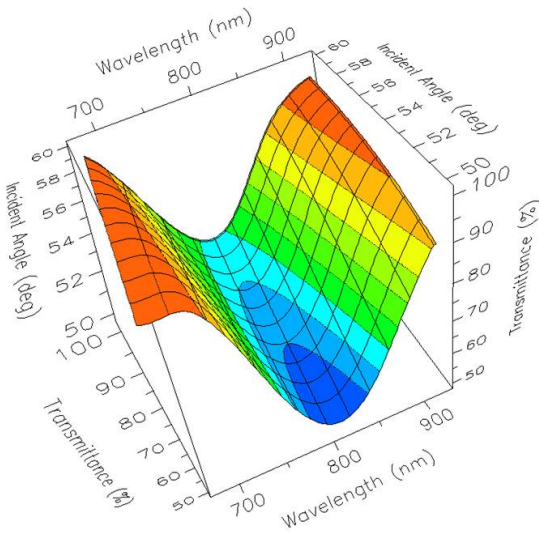
In this work, we chose to use dielectric multilayer filters to provide sufficient gain narrowing compensation since well designed dielectric multilayer filters have proved capable of alleviating gain

narrowing for an amplification bandwidth of more than 200 nm in a terawatt-class CPA system[85]. For us, in order to achieve direct amplification of sub-15-fs pulses at the 10 to 100 TW level, the key is to design a proper loss profile for a gain narrowing compensation filter (GNC).

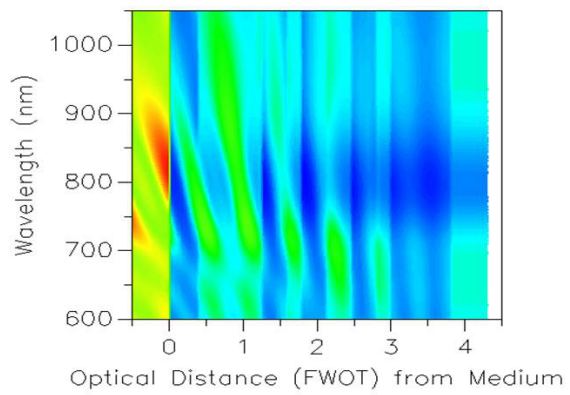
A quarter wave stack of $\text{HfO}_2/\text{SiO}_2$ layer structure was used to provide the required high damage threshold for our TW laser system. The incident angle of the dielectric multilayer filters were chosen at close to Brewster angle of 56° to eliminate the need of an AR coating on the other side of the substrate. The filter transmission curve and other layer properties are shown in Figure [?].



(a) Designed transmission curve for Ti:Sapphire CPA GNC filter.



(b) The angle dependent transmittance.



(c) The relative field intensity inside the filter.

Figure 2.14: Properties of gain narrowing compensation filter.

The curve of our GNC filter matches the gain profile of Ti:Sapphire over a wavelength range from 700 nm to 950 nm and becomes zero outside this region. This is shown in Figure 2.14. The film composition was calculated using the iterative algorithm with the dumped least squares method [86]. According to the simulation on an amplifier gain model, this design will provide the most spectrum broadening without sacrificing much single pass gain.

A similar filter design was used in the kHz laser system to reduce gain narrowing. Filters inserted at three different locations were passed eight times total. The final compressed pulse duration was reduced to 20 fs instead of 33 fs when no filter was used.

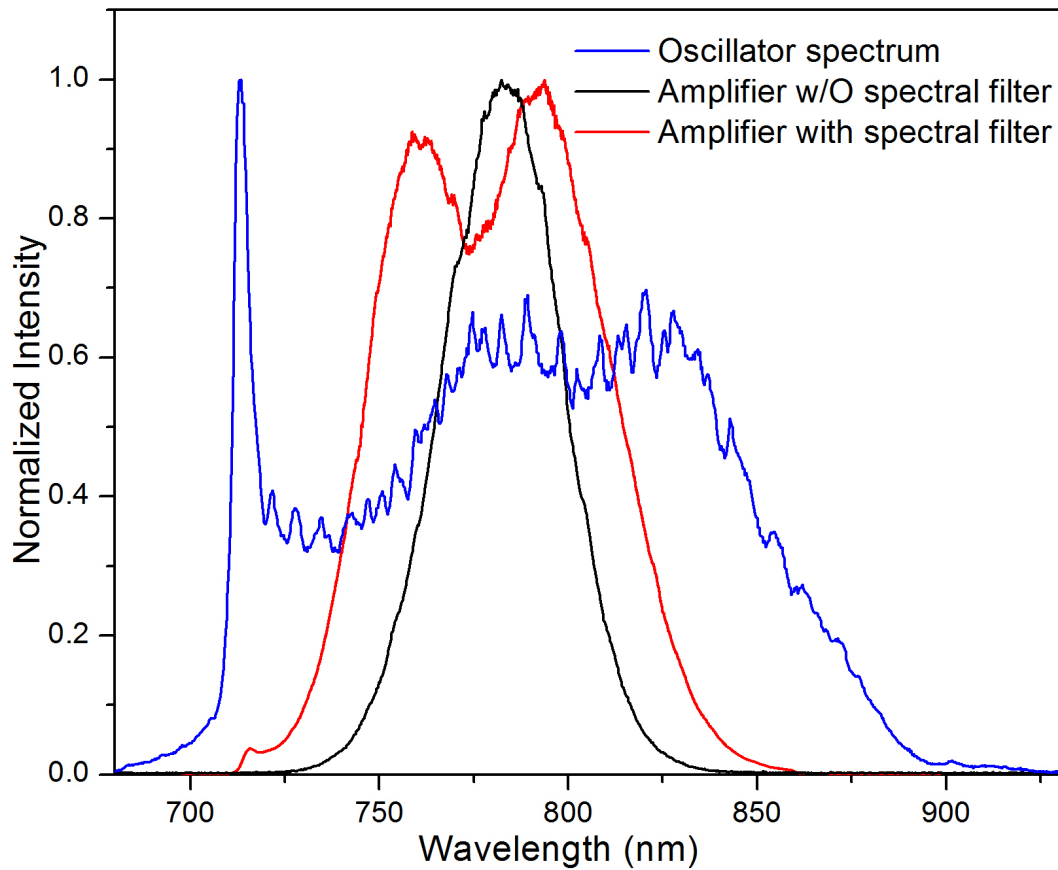


Figure 2.15: The kHz laser spectra with and without spectral filtering.

2.4.6 Dielectric mirror for high energy broadband pulse amplification

For CPA systems, mirror selection is a critical part of the design. Due to the high loss and low damage thresholds of metal coating, metallic mirrors are not commonly used in the amplifier stages even though they are very broadband. On the other side, multilayer dielectric mirrors can provide almost 100% reflectivity at a designed wavelength with a high damage threshold; however, single stack structured multilayer dielectric mirrors carries a limited bandwidth usually due to limited selection of the high refractive index material in the layer design [87, 88]. For example, the CVI

Melles Griot TLMB high damage mirror, which is commonly used to reflect the amplified pulses in CPA lasers, has a damage threshold of 1.3 J/cm^2 for 46 fs pulses. At normal incidence, the loss is less than 1%, but its bandwidth can only support 740 nm to 860 nm – less than the bandwidth required for amplifying a sub 15 fs pulse. On the other hand, the measured bandwidth of the CVI Melles Griot TLM2 broadband mirror is $\sim 200 \text{ nm}$ for s-polarized light, meaning it can support 15 fs lasers [89]. However, the damage threshold is low ($\sim 100 \text{ mJ/cm}^2$ for 8 ns pulses), which is not sufficient for joule-level amplified pulses when the beam size is $\sim 1 \text{ cm}$. Table 2.2 is a summary of multilayer dielectric mirrors used in building the CPA system. Some of the table values are empirical since the coating result is highly dependent on the coating material supply, the coating process, and the layer structure error in a single coating run.

Table 2.2: Summary of Optical Mirrors for Laser Amplifier

Maker	Model	Bandwidth (@800 nm, 45°, $\geq 99\%$)	Damage Threshold (for 10 ns pulse)
CVI Melles Griot	Protected Silver	400 nm to 20 μm ($\geq 95\%$)	$\leq 0.05 \text{ J/cm}^2$
CVI Melles Griot	TLM1	$\geq 100 \text{ nm}$	$\geq 20 \text{ J/cm}^2$
CVI Melles Griot	TLM2	$\sim 200 \text{ nm}$	$\geq 0.1 \text{ J/cm}^2$
CVI Melles Griot	TLMB	$\geq 150 \text{ nm}$	$\geq 6 \text{ J/cm}^2$
Newport	Low GVD Broadband	$\geq 200 \text{ nm}$	$\sim 1 \text{ J/cm}^2$
Laser Components	HR800	$\sim 200 \text{ nm}$	$\geq 0.5 \text{ J/cm}^2$
Sigma Koki	FLM1	$\sim 200 \text{ nm}$	$\sim \text{TLM1}$
Sigma Koki	FLM2	$\geq 250 \text{ nm}$	$\sim \text{TLM2}$

TW level sub-15 fs CPA amplification not only requires mirrors with high damage threshold and high reflectivity, but also a broad bandwidth to support the wide spectrum required for the pulse

duration. By arranging broadband $\text{TiO}_2\text{-SiO}_2$ coatings underneath another stack of high-damage threshold coatings ($\text{ZrO}_2\text{-SiO}_2$) to reduce the intensity on the broadband coatings, this mirror can survive high input laser intensity while providing broadband reflectivity at the same time [90].

The bandwidth of this hybrid structured broadband high-energy mirror is almost equivalent to that of a commercial broadband mirror, while its damage threshold of $>1 \text{ J/cm}^2$ for 100 fs pulses is also comparable to that of the commercial high energy mirror.

Even though there is usually a trade-off between the two features, the mirror structure is further optimized to provide *both* high damage threshold *and* low dispersion. The mirror reflectivity and phase group delay is show in Figure 2.4.6. ZrO_2 was replaced with HfO_2 to increase the bandwidth and damage threshold for the high damage threshold layers. This increase in the laser-induced damage threshold can essentially be explained by the wider band gap of HfO_2 as compared to ZrO_2 [91]. The mirror provides high reflectivity with a sufficiently broad spectral width to support sub 15 fs pulses for s-polarized light at 45° incidence.

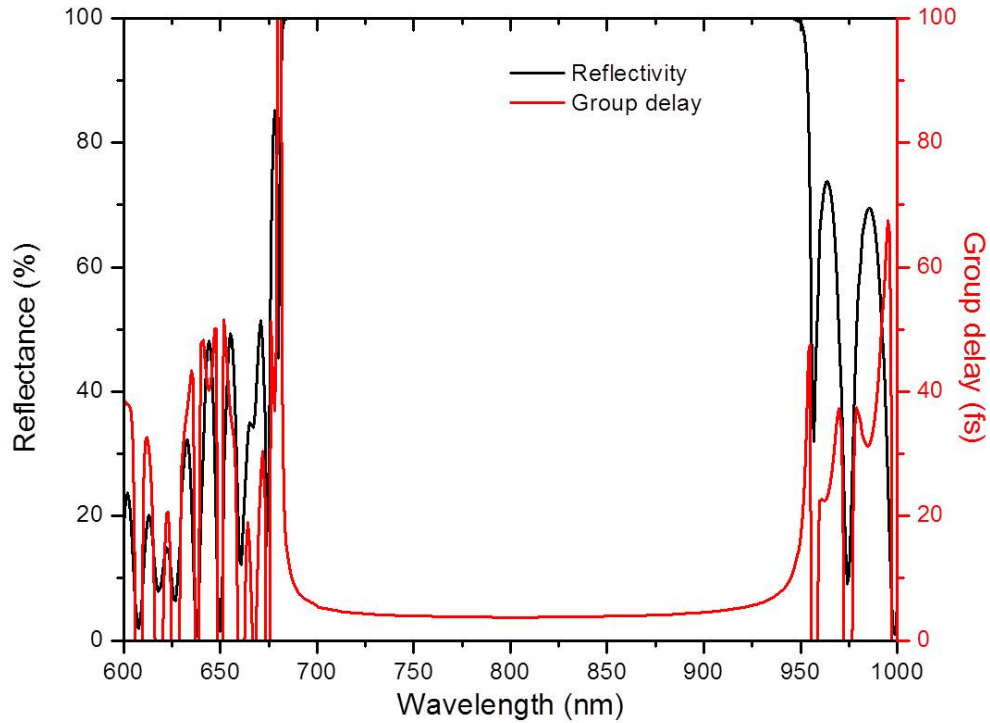
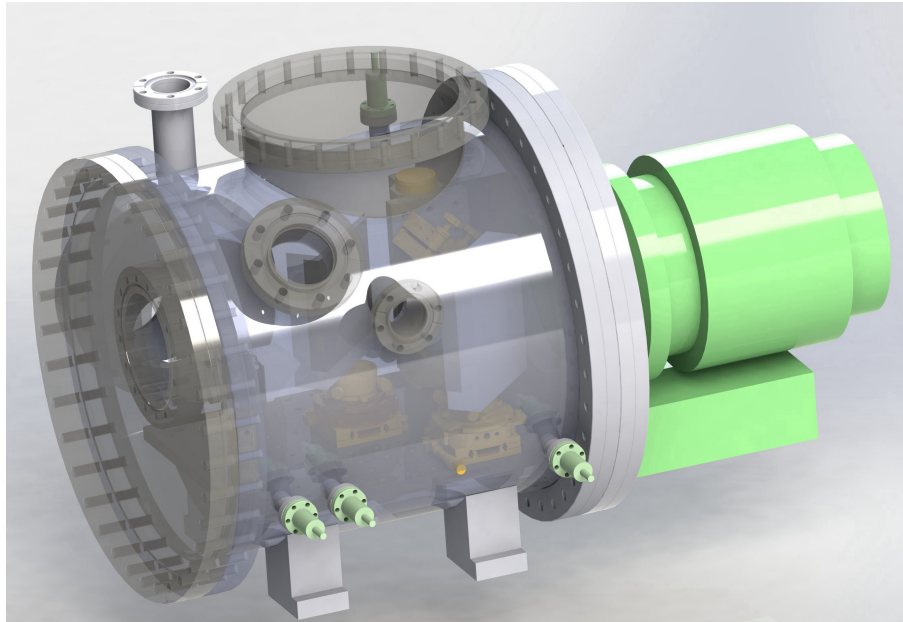


Figure 2.16: Calculated reflectivity and group delay of the broadband high-energy mirror.

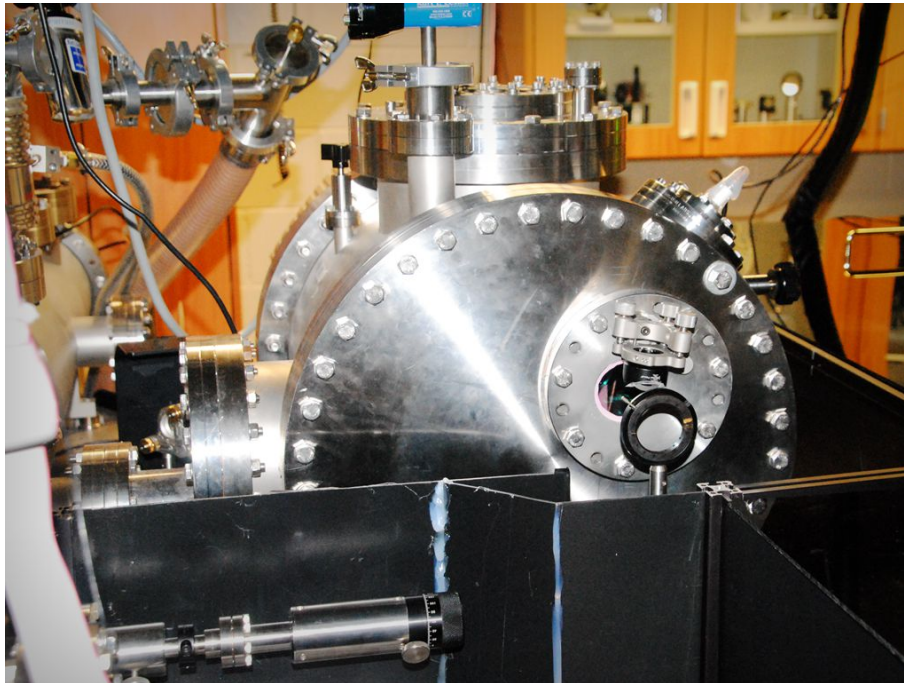
2.4.7 20 TW laser amplifier compressor

To prevent laser beam degradation from non-linear effects during propagation, the amplified 700 mJ laser beam is expanded to a diameter of 35 mm before it is sent under vacuum to a pulse compressor. The vacuum compressor uses a pair of 1400 l/mm gratings (110 mm × 110 mm) and has an overall throughput of 50%. The energy of the pulse was 350 mJ for a 700 mJ input, which indicates that the peak power of the laser reached 20 TW. Even higher power (30 TW) is expected once the current gratings are replaced with a larger-dimension, higher-throughput pair capable of accom-

modating the 700 mJ input. The compressor is kept in vacuum to avoid nonlinear effect resulting from the interaction between the compressed 20 TW laser pulse and air, as shown in Figure 2.17.



(a) Compressor chamber design with optics.

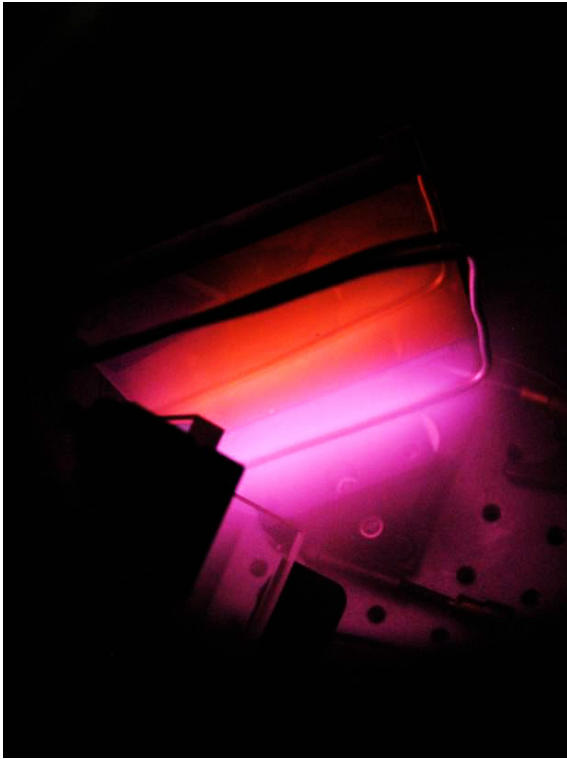


(b) Photo of the vacuum compressor.

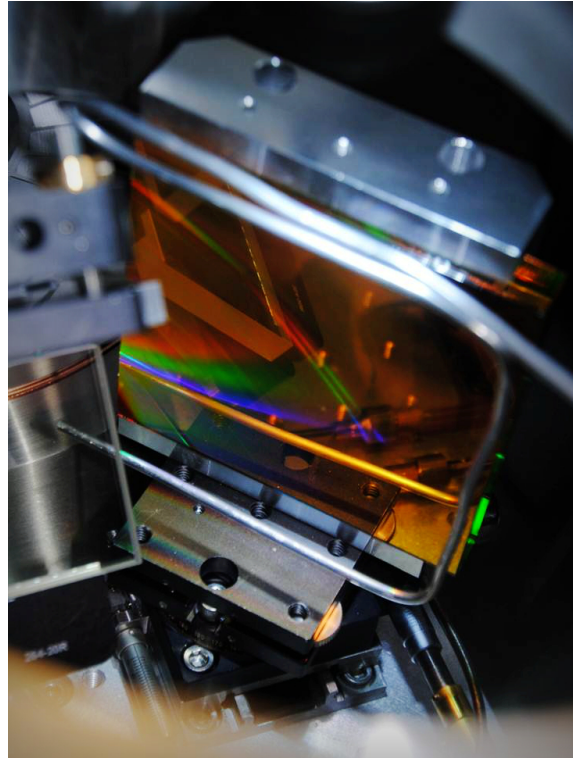
Figure 2.17: Vacuum compressor for sub 15 fs, 20 TW beamline.

However, because of the high intensity carried by the laser beam, organic substances trapped in the chamber are cracked, and carbon is deposited on the area irradiated by the laser beam. This is particularly troublesome in the case of gold coated gratings, which cannot be wiped clean as can be done to dielectric coatings. The carbon layer absorbs energy and the throughput of the system reduces when the laser operation as time adds up.

In order to clean the carbon deposition, we designed a cleaning system based on a radio frequency discharge. This is an established technique in many ultra-clean manufacturing environments, like the microprocessor industry for example, where it has several advantages over other cleaning techniques [92, 93]. One of the advantages of such a cleaning system is the direct installation along the beam line which not only allows a fast and reproducible cleaning of the optics, but also obsolesces the need to remove them from the beam line.



(a) RF glow discharge in O_2 -Ar gas mix in the compressor chamber.



(b) Photo of the grating after the cleaning procedure. The cleaning time was about 30 min.

Figure 2.18: RF discharge grating cleaning.

The procedure is based on the generation of a radio frequency (RF) discharge inside a vacuum chamber filled with a mixture of argon (neutral gas) and oxygen (active gas). The produced plasma leads, through charged particle bombardment, to the oxidation of the layers thereby forming CO and CO_2 .

We verified the cleaning process by cleaning the first grating, which the compressed femtosecond beam hits on, in our compressor chamber by the RF plasma discharge. Before cleaning, imprints of the laser beam were clearly visible; after cleaning, the imprints close to the antenna could no longer be seen. The overall transmission efficiency of the compressor was measured to be recovered

back to over 50%.

2.4.8 Pulse duration and power stability measurement

As a nonlinear process, HHG strongly depends on the quality of the driving laser. In order to ensure optimal generation conditions, efforts have been made to improve the condition of pulse duration, pulse energy stability and beam focus profile.

After the two stage power amplifier, the pulse spectrum extends from 700 nm to 900 nm, which supports 12.2 fs transform limited pulses. In order to compress the pulse to the shortest pulse duration possible, the separation and incident angle of the compressor gratings were first fine-tuned manually to obtain a spectral phase that changed only gradually over any narrow range. The high-order phase distortions were further compensated by the low-loss, 4f-zero-dispersion adaptive phase modulator which will be introduced in Section 3.2.2.

A pulse duration of 14 fs was obtained by optimizing the deformable mirror shape in the adaptive phase modulator. The measured and retrieved FROG traces of the pulse are represented in Figure 2.19 (a) and (b) respectively. Figure 2.19(c) is the retrieved pulse shape (solid line) and phase (dashed line). Figure 2.19(d) shows retrieved power spectrum (solid black line) and phase (dashed line) with the independently-measured spectrum (solid red line).

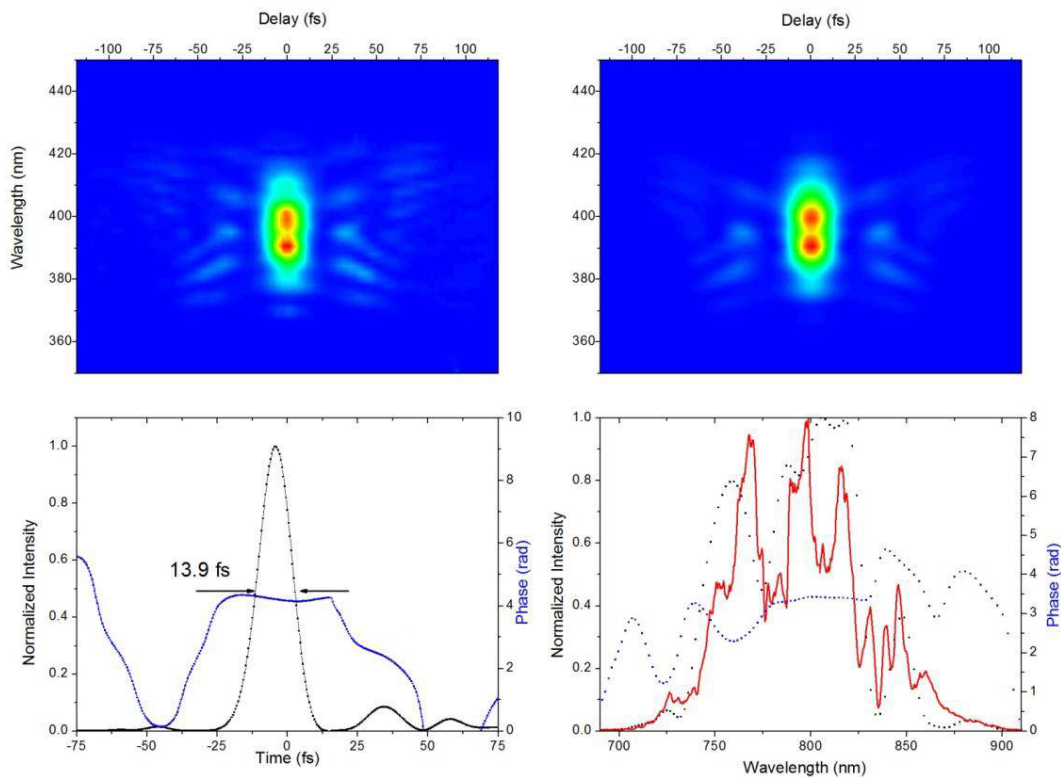


Figure 2.19: Characterization of the 14 fs laser pulse by SHG FROG.

The long term stability of the amplified pulse energy measured around 220 mJ after compression has a rms/mean of 1.6%, whereas the shot-to-shot fluctuation is for 99% of all laser pulses over 6 hours (Figure 2.20). For a laser system based on flash lamp powered pump lasers, such a stability can be reached since the both the power amplifier stages, including the front end kHz system, are all working in the designed saturation range of the gain media.

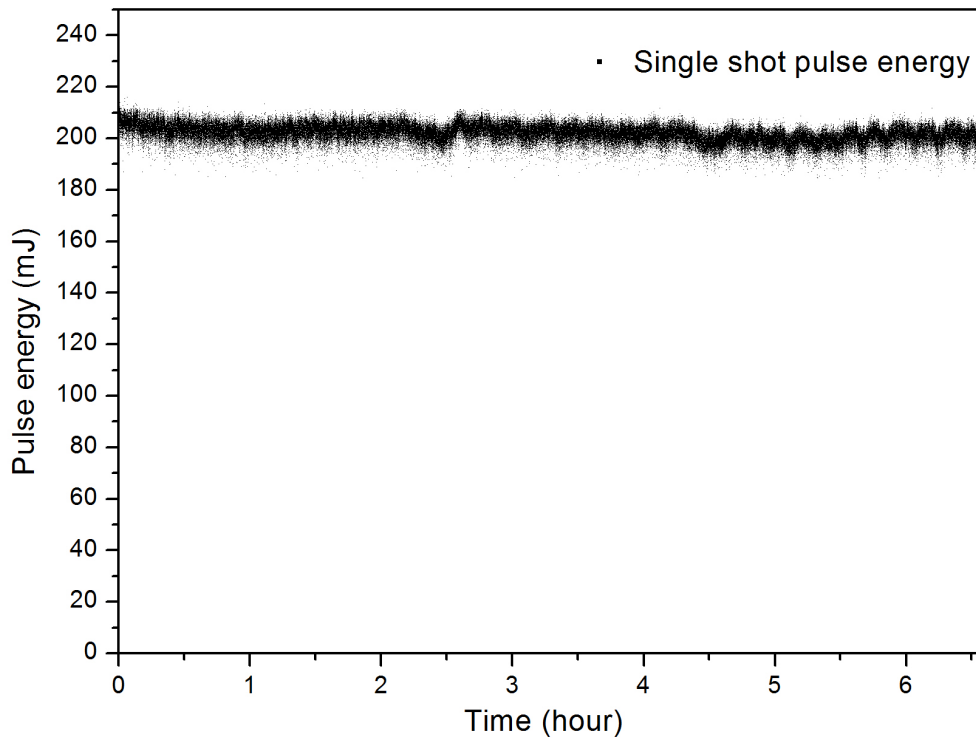


Figure 2.20: Single shot pulse energy recorded by sampling a portion of the power amplifier output with a fast photodiode.

The laser beam focus profile was another important beam parameter checked after completion of the laser construction. Since a long focal length concave mirror was used to create a loose focus to improve HHG efficiency [94], the diameter of the focal spot was 0.31 mm (FWHM). The focal spot profile shown in Figure 2.21 was fairly good considering no wavefront correction system was used. This is thanks to the small crystal thicknesses in the power amplifier stages and the good surface quality of the holographic master gratings used in the stretcher and compressor [95].

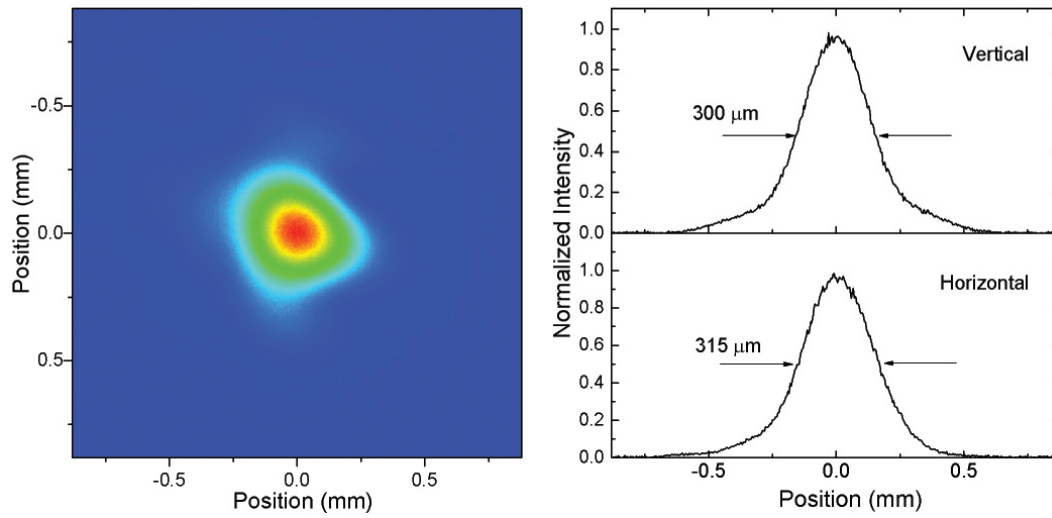


Figure 2.21: Intensity profile measurement at focus of $f=6.5$ m mirror with a 12-bit CCD camera. The horizontal and vertical line-out show the diameter is $310 \mu\text{m}$ at half-maximum.

CHAPTER 3: PHASE CONTROL OF SHORT PULSES

It is beneficial to use the shortest available laser pulses for isolated attosecond pulses generation: the shorter the driving laser pulse, the higher the concentration of overall pulse energy in every half optical cycle. In order to reach the ideal gating result, dispersion control of few-cycle pulses is critical. In the past, considerable progress has been made, including schemes with chirped mirror compressors [96, 97], acousto-optic programmable dispersive filters (AOPDF) [98, 99], and adaptive phase control through spatial phase modulators [100, 101].

The adaptive phase control of the spectral phase of femtosecond laser pulses makes it possible to compress pulses with minimal phase distortion. In the research I have conducted, spatial phase modulators based on liquid crystal technology and deformable mirrors have been applied for adaptive phase correction for 5 fs and 15 fs pulse widths, respectively, to allow sub-optical cycle precision in controlling the gating for attosecond XUV generation [40].

3.1 Femtosecond Spectral Phase Control

Few-cycle pulses have broad frequency spectra, and their pulse duration and shape are very sensitive to dispersion. For example, a 10 fs Gaussian pulse will be stretched to 31.2 fs after propagating in air for 5 m, which is over three times the original pulse duration.

For the white-light generated in the hollow-core fiber, chirped mirrors are the most frequently used dispersion control method. The multilayer coating of chirped mirrors allows the different wavelength components of the incident white-light to penetrate and reflect back from different depths [96, 102]. By arranging the wavelength dependent depths, group delay dispersion (GDD) can be manipulated over the spectral range.

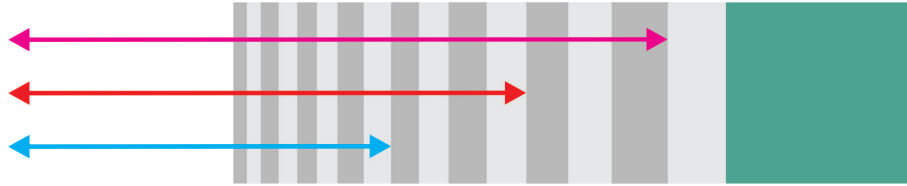


Figure 3.1: Principle of a chirped mirror. Light with a long wavelength penetrates deeper into the multilayer structure and experiences a bigger group delay.

Chirped mirror compressors carry very high throughput. However, the maximum GDD allowed by a chirped mirror is limited. For example, chirped mirror pairs for compressing sub 10 fs pulses usually carry a GDD of negative 50 fs^2 [103]. Nevertheless, the dispersion introduced by a given set of chirped mirrors can only be changed by a discrete amount, thus making it difficult to accommodate the day-to-day change of the alignment-sensitive white light pulses.

On the other side, an acousto-optic interaction in an anisotropic birefringent medium (such as in an AOPDF) can be used to compensate residual high-order phase errors and flatten the gain narrowing profile in a CPA system. A three-stage, 1-kHz amplifier system delivering 0.3 TW sub 10 fs were reported using this technology [76]. However, the efficiency of an AOPDF is lower than other spectral phase control methods ($<50\%$ for over 200 nm bandwidth) [104].

3.2 Adaptive Phase Modulator

On the other hand, adaptive phase modulators provide higher flexibility and a broader bandwidth of phase control. Pulses with duration of 2.8 fs were obtained by using a similar phase modulator [1]. However, the energy of such extremely short pulses is only $0.5 \mu\text{J}$, which is orders of magnitude

away from the energy needed for attosecond pulse generation. The energy deficiency is the result of the high loss of the phase modulator and the limited input laser energy.

3.2.1 0.5 mJ, 5 fs Pulse from Adaptive Phase Modulator

In order to obtain millijoule-level few-cycle pulses, an adaptive phase modulator with improved throughput is used to compress the white light pulses from the hollow-core fiber.

The mJ energy level pulse from the HC fiber had a octave span bandwidth covering 500 nm to 1000 nm. In order to judiciously modify the individual spectral phase of different wavelength, a zero dispersion 4-f system consisting of silver coated gratings and cylindrical cavity mirrors was used to create a Fourier plane for the laser pulse. A 640-pixel liquid crystal SLM (Jenoptik SLM-S640) was placed at the Fourier plan [105]. The setup is shown in Figure 3.2.1. The broadband laser pulses from the hollow-core fiber was angularly dispersed by the first grating. Cylindrical mirrors were used instead of spherical mirrors to reduce the laser intensity on the liquid crystal pixels of the SLM. Using this phase modulator, the chirp at each frequency point could be modified by programming the refractive index of each pixel of the SLM. The overall throughput of the phase modulator was $\sim 50\%$, which mostly comes from the loss of the silver-coated gratings (80%) and SLM (90%).

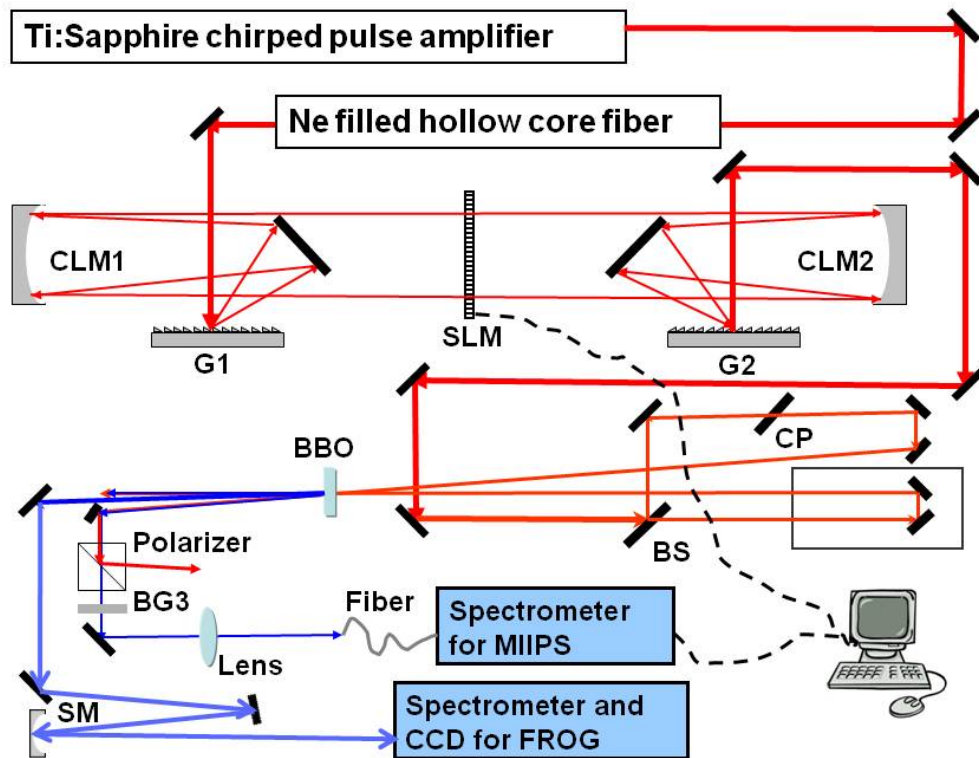


Figure 3.2: The adaptive phase modulator. The white-light from HC fiber were sent to the spatial light modulator. SH generation from a BBO was used for simultaneous MIIPS and FROG measurements. G1, G2: gratings, CLM1, CLM2: cylindrical mirrors. Figure adapted from Ref. [1]

The type I phase matched second harmonic signal from a 5 μm thick BBO crystal was used in the process of optimizing the phase of the white light pulse. Multiphoton intrapulse interference phase scan method (MIIPS) was chosen over an evolutionary algorithm approach since it has proven to be more efficient for correcting the spectral phase of an octave-spanning laser pulse [106, 107].

In order to perform the MIIPS method, second harmonic spectra were recorded at the same time that the SLM modulated the spectral phase of the fundamental pulses. A periodic sinusoidal phase function $f(\omega) = \alpha \cos(\gamma\omega - \delta)$ was used to scan across the bandwidth of the pulse as the measurement proceeded. Here, ω is spectrum frequency, and α and γ are two parameters that need to be chosen properly. (In our case $\alpha = 5$, $\gamma = 7$ fs).

The sum of the unknown pulse phase $\Phi(\omega)$ and the modulated phase $f(\omega)$ is given by $\phi(\omega) = \Phi(\omega) + f(\omega)$. The SHG signal as a result of the combined phase can be expressed as

$$I(\omega) = \left| \int |E(\omega + \Omega)| |E(\omega - \Omega)| \times \exp\{i[\phi(\omega + \Omega) + \phi(\omega - \Omega)]\} d\Omega \right|^2. \quad (3.1)$$

The SHG signal reaches a maximum when $\phi(\omega + \Omega) + \phi(\omega - \Omega)$ is zero. The Taylor expansion of the phase sum around ω is

$$\phi(\omega + \Omega) + \phi(\omega - \Omega) = 2\phi_0 + \phi''(\omega)\Omega^2 + \dots + \frac{2}{(2n)!} \phi^{2n'}(\omega)\Omega^{2n}. \quad (3.2)$$

The maximum SHG signal occurs for $\Phi''(\omega) = -f''(\omega)$. By changing the δ value in the modulated phase function, one can scan the applied GDD $f''(\omega) = \alpha\gamma \cos(\gamma\omega - \delta)$ for each frequency ω .

By searching the SHG peak position in the MIIPS trace for each SH frequency 2ω , $\Phi_1''(\omega) = -f_1''(\omega) = -\alpha\gamma \cos(\gamma\omega - \delta)$ is retrieved from the MIIPS pattern for the first iteration. The phase $\Phi_1(\omega)$ can be integrated from $\Phi_1''(\omega)$. $\Phi_1(\omega)$ is only a close guess of $\Phi(\omega)$ since there are high order terms we have ignored in the process. In order to retrieve the phase more accurately, more iterations are required to map the phase. We start the second iteration with $-\Phi_1(\omega)$ applied to the SLM, and the measured phase value $\Phi_2(\omega)$ is the phase difference $\Phi(\omega) - \Phi_1(\omega)$. Using the measured phase difference, a better guess of $\Phi_2(\omega) + \Phi_1(\omega)$ can be used to start next iteration.

After several iterations, the retrieved phase difference $\Phi_m(\omega)$ becomes constant and the retrieved phase $\sum \Phi_m(\omega)$ should converge to $\Phi(\omega)$.

The first iteration of the MIIPS pattern is shown in Figure 3.3(a). Figure 3.3(b) shows the MIIPS pattern in the final iteration. The evenly spaced SH trace is a good indication of a well compressed pulse close to the transform-limited duration [106].

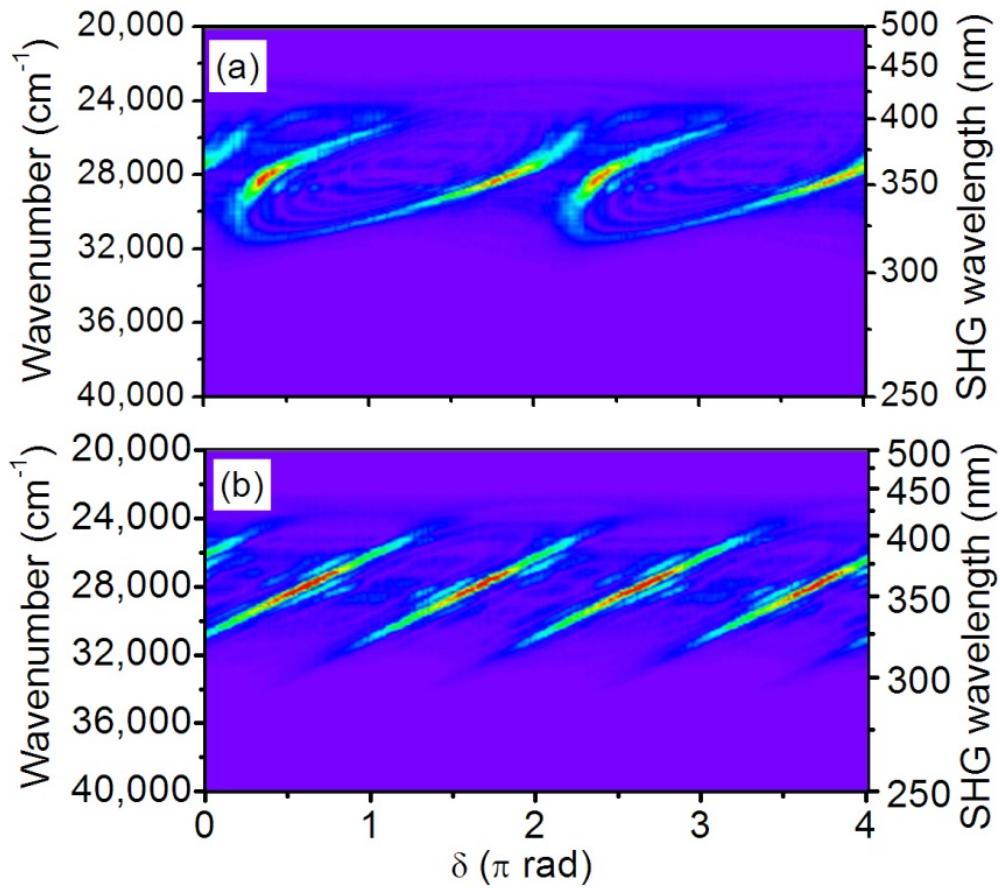


Figure 3.3: The MIIPS traces (a) from the first iteration; (b) from the last iteration. Figure adapted from Ref. [1].

The pulse duration of the MIIPS compressed pulse was measured by the SHG-FROG [108, 109]. Since few-cycle pulses can be easily distorted by dispersion introduced by propagation in air, the FROG measurement shares the same crystal as the MIIPS. In order to retrieve a pulse duration as short as sub 5 fs pulses, the FROG setup is upgraded by using a silver coated spherical mirror

instead of a lens to image the SHG into the spectrometer to avoid the chromatic aberration. The measured and reconstructed FROG patterns are shown in Figure 3.2.1(a) and (b). The retrieved pulse duration is 5.1 fs as shown in Figure 3.2.1(c), and the spectral phase in 3.2.1(d) shows the chirp was well compensated by MIIPS.

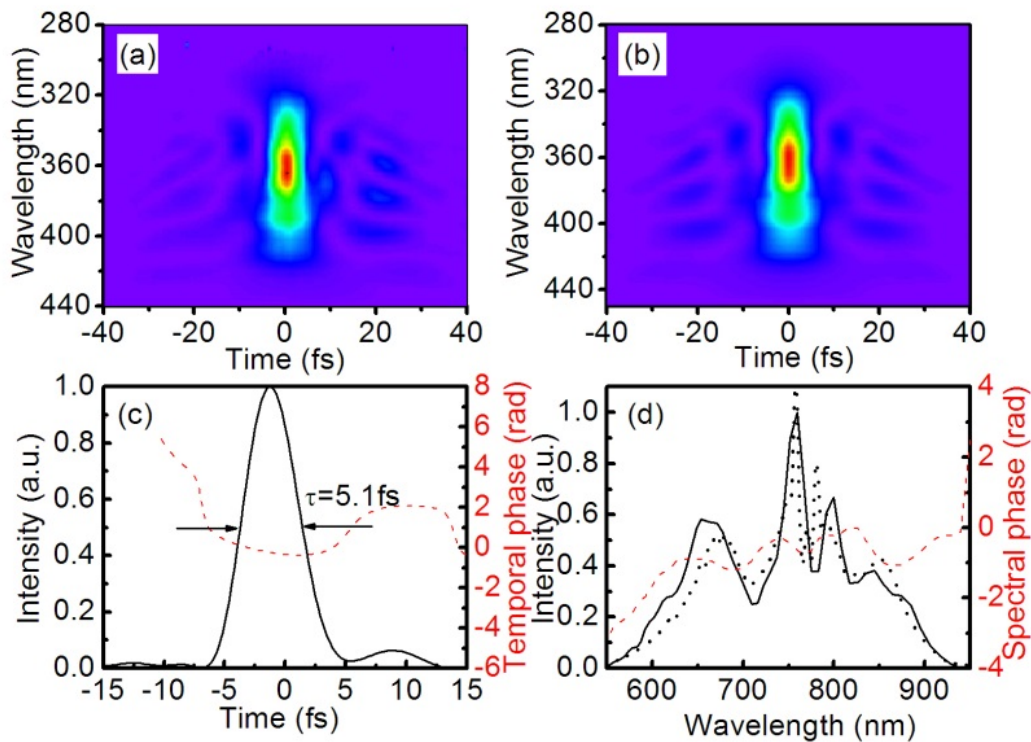
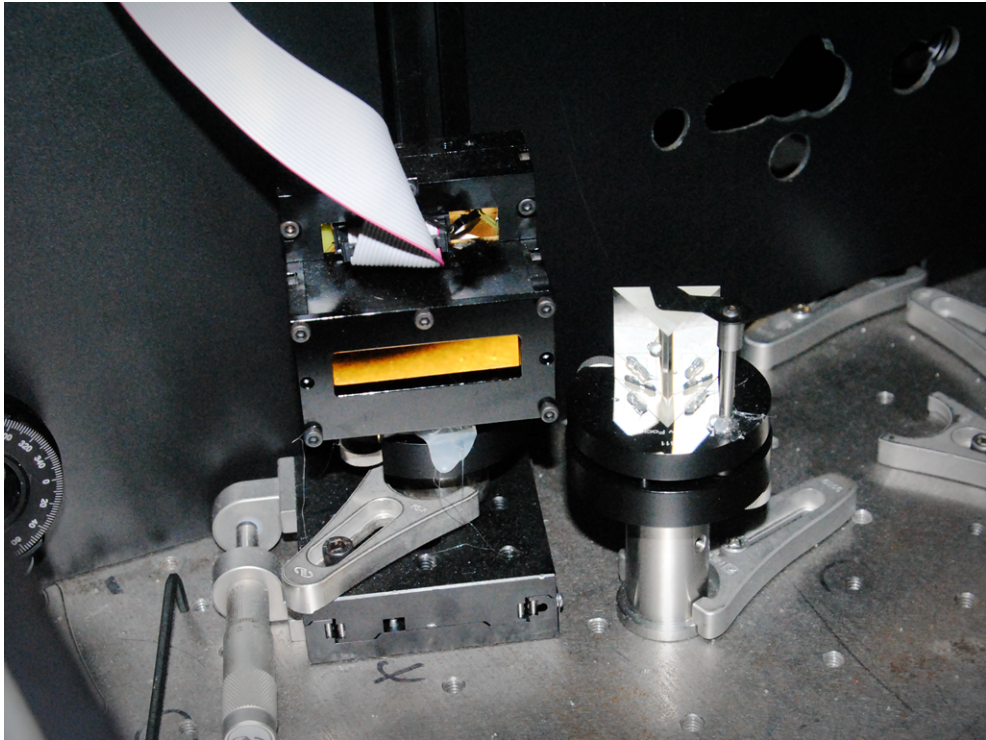


Figure 3.4: A 5 fs compressed pulse measured by the FROG. Figure adapted from Ref. [1].

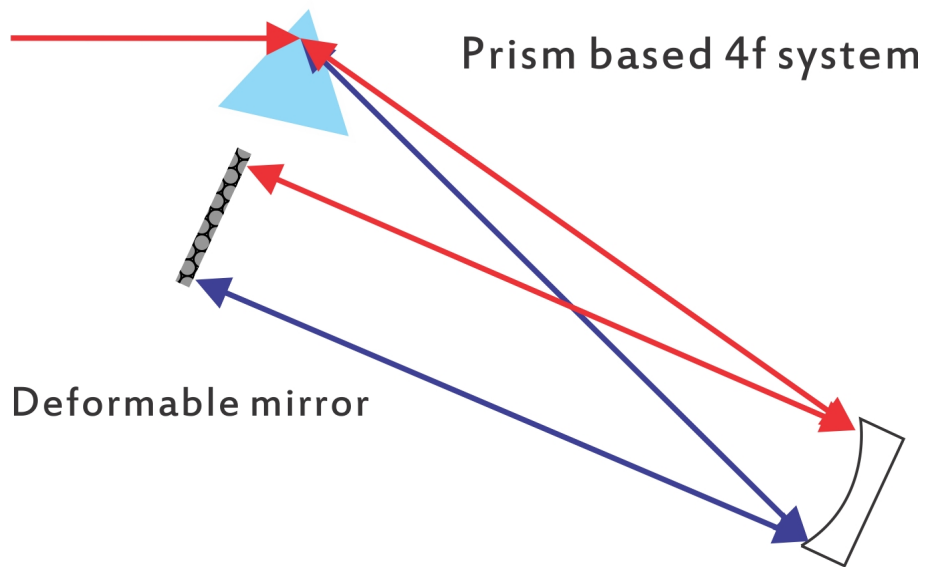
3.2.2 Deformable mirror-based high-throughput phase modulator for TW laser

The pulse compression process can also be aided by a deformable mirror based phase modulator. In this case, the beam is directed into a single shot SHG-FROG for pulse duration measurement.

Inside the final pulse compressor, the separation and incident angle of the gratings are fine tuned manually to obtain a spectral phase that changes only gradually over any narrow range. This is done so that the high order phase distortions can be compensated by the $4f$ -zero-dispersion adaptive phase modulator [110, 111]. This is located between the pulse stretcher and the first amplification stage. In the phase modulator, the laser beam is angularly dispersed by a Brewster angle cut SF10 prism and recollimated onto a 50 mm long, 20 channel bare gold coated linear piezoelectric deformable mirror (OKO Technologies) using a dielectric coated mirror with a focal length of 1.5 m [112]. We chose piezoelectric deformable mirror over membrane based deformable mirror to avoid damage due to high laser intensity [113]. The optical layout is shown in Figure 3.5. The overall transmission of such a phase modulator reaches 85% for a bandwidth over 200 nm.



(a) Picture of OKO piezoelectric deformable mirror with 2 rows of 10 actuators.



(b) Prism based low loss zero dispersion $4 - f$ system.

Figure 3.5: Experimental setup of the low loss deformable mirror phase modulator.

For optimizing the pulse compression, the FROG traces were processed as the fitness function for a simple genetic algorithm [114], which controlled the voltages applied to the 20 deformable mirror actuators.

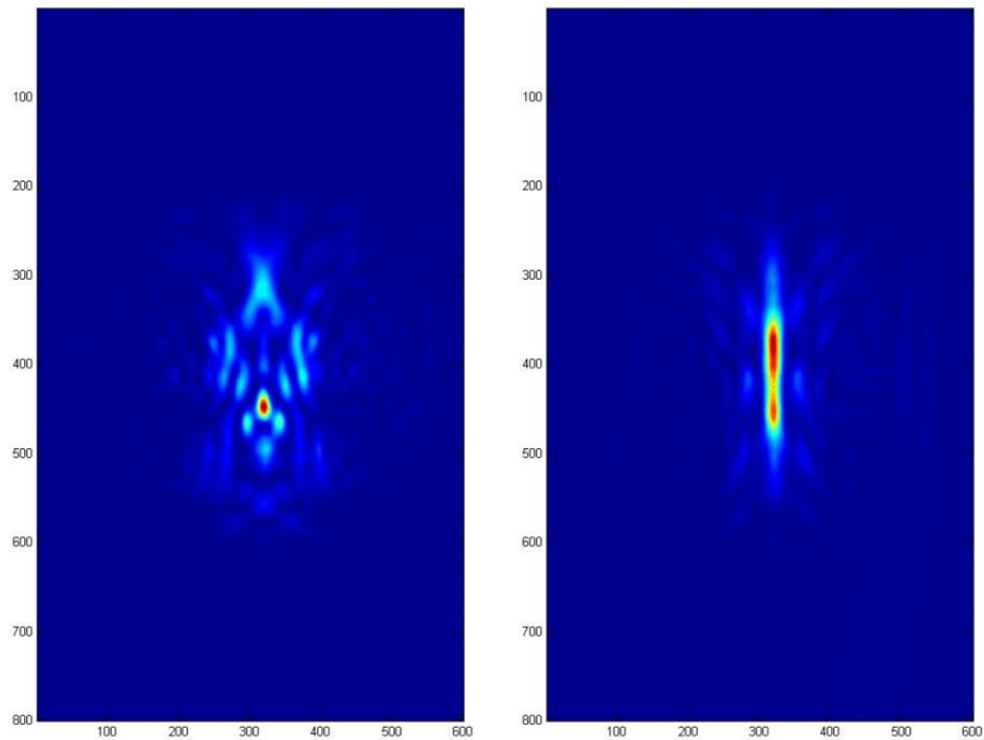


Figure 3.6: Effect of deformable mirror phase modulator pulse compression. Left (same displacement voltage applied to all actuators): splitted FROG structure implies strong satellite pulses due to high order phase distortion. Right (optimized deformable mirror actuator voltages): narrow shape FROG trace shows close to transform limited pulse duration.

After running the algorithm to convergence (usually ~ 20 iterations), a pulse duration of 14 fs can

be obtained, as displayed in Figure 2.19.

3.3 Carrier Envelope Phase

The process of HHG is highly dependent on the CE phase of the driving laser used [20, 115]. For sub-cycle gating for the generation of isolated attosecond pulses, it is more important to have the driving laser source CE phase locked [116, 117, 118].

For an ultrafast optical pulse, its electric field at a fixed point in space can be expressed as:

$$\varepsilon(t) = E(t)\cos[\omega_0 t + \varphi_{CE}], \quad (3.3)$$

where $E(t)$ is the envelope of the pulse, ω_0 is the frequency of carrier wave. The CE phase φ_{CE} is defined as the offset between the phase of the carrier wave and the envelope position or, in other words, the peak of the pulse envelope and the peak of the electric field.

With few-cycle pulses, the relative position between the pulse envelope and its underlying electric-field carrier has a dramatic influence on high field processes such as above threshold ionization (ATI) and HHG [119, 120, 121]. When using few-cycle pulses to produce single attosecond pulses through HHG, the CE phase has to be stabilized to guarantee the generation of isolated attosecond pulses [122].

Up to the time of this thesis, the CE phase of the iFAST lab 1 kHz CPA system has been successfully stabilized by the grating shaking method. Work has been carrying on to actively lock the CE phase of the 10 Hz, 20 TW laser system.

3.3.1 Stabilization of the carrier envelope phase in oscillator

Carrier-envelope phase stabilization in the oscillator is achieved by a commercially available phase detecting and locking system (Menlo Systems XPS 800). The CE phase detection is done by the f-to-2f self-referencing method.

For a Kerr lens mode locked (KLM) femtosecond Ti:Sapphire oscillator, the CE phase change between consecutive pulses due to different phase velocity and group velocity:

$$\Delta\varphi_{CE} = \Delta\varphi_g - \Delta\varphi_p = \omega_0 \left[\frac{L_0}{\nu_g(\omega_0)} - \frac{L_0}{\nu_p(\omega_0)} \right] = -2\pi L_0 \left. \frac{dn}{d\lambda} \right|_{\omega_0}, \quad (3.4)$$

where $\nu_g(\omega_0)$ is the group velocity, $\nu_p(\omega_0)$ is the phase velocity at the central carrier wave frequency ω_0 , L_0 is the length of the dispersive medium inside the oscillator cavity, and n is the refraction index of the dispersive medium, which in our case is mostly from the Ti:Sapphire crystal and air.

The self-referencing method is carried out first by spectrally broadening the 12 fs oscillator output through a photonic crystal fiber (PCF) to reach an octave-spanning spectrum. Then its low frequency spectrum component is frequency doubled to beat with the high frequency spectrum to produce f_0 [123, 124]. The frequency difference between the f and $2f$ components is the offset frequency, which is the frequency domain counterpart of CE phase.

$$f_0 = 2f_n - f_{2n} = 2(nf_{rep} + f_0) - (2nf_{rep} + f_0). \quad (3.5)$$

The CE phase is stabilized by locking the offset frequency to a quarter of repetition rate ($f_{rep}/4$) by modulating the pump power sent to the Ti:Sapphire crystal, since changing the pump laser power will modify the refractive index of the Ti:Sapphire crystal and thus the group and phase velocities

of laser pulse [125, 126]. This pump laser modulation is achieved by acousto-optic modulator (AOM) on a very fast time scale.

3.3.2 Carrier envelope phase stabilization of chirped pulse amplifier

From the CE phase-stabilized oscillator, the pulses with the same CE phase are selected by the Pockels cell for amplification. The CE phase of amplified pulses are measured by single-shot non-linear spectral interferometry [127]. The pulses are focused into a sapphire crystal to generate a white light continuum, whose long wavelength components are frequency doubled to overlap and interfere with its short wavelength parts. The setup for measuring amplified pulse CE phase is shown in Figure 3.7 [128]. Relative CE phase for each individual amplified pulse can be extracted from the interference fringes using the standard algorithm of Fourier transform spectral interferometry (FTSI) [129].

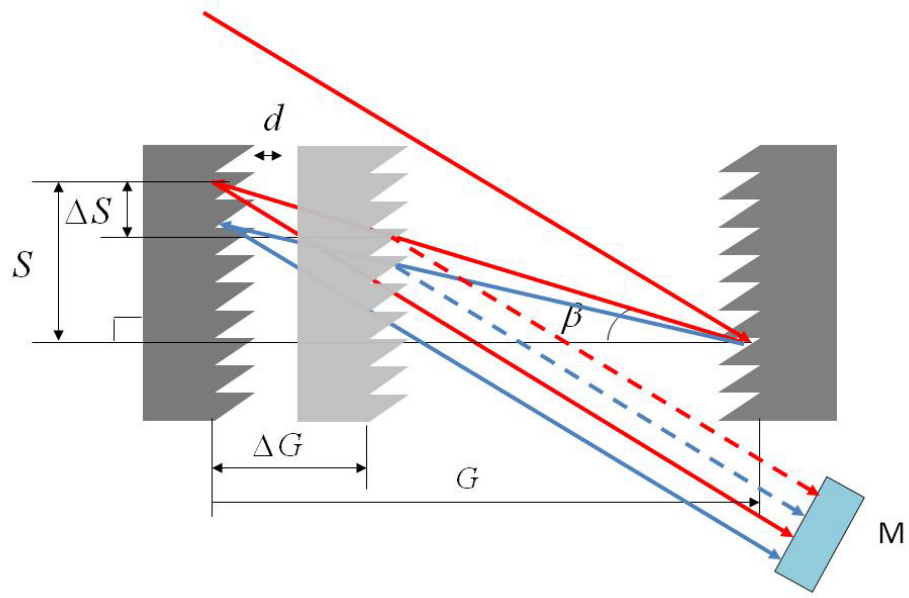


Figure 3.8: CE phase control by shifting the grating separation.

The input electric field of a laser pulse in the frequency domain is given by:

$$\tilde{E}(\omega) = U(\omega) \exp[i(\varphi_{CE} + \varphi(\omega))], \quad (3.6)$$

where $\varphi(\omega)$ is the spectral phase, $U(\omega)$ is the spectral amplitude. For this analysis, the pulse is assumed to be transform limited which gives $\varphi(\omega)$ zero [130]. The spectral phase of the pulse after it propagates through the grating compressor is given by:

$$\varphi(\omega) = -\frac{\omega}{c}P'(\omega) + \varphi_c(\omega), \quad (3.7)$$

where P' is the optical path length and

$$\varphi_c(\omega) = 2\pi \frac{G}{d} \tan[\beta(\omega)] \quad (3.8)$$

where G is the perpendicular distance for gratings, d is the grating line density, and $\beta(\omega)$ is the diffraction angle in Figure 3.8. Since stretcher and compressor usually have the grating incident angle close to the Littrow angle, that makes $\tan[\beta(\omega)] \approx 1$. Thus the CE phase change with regard to grating movement ΔG is:

$$\Delta\varphi_{CE} = 2\pi \frac{\Delta G}{d} \tan[\beta(\omega)] \approx 2\pi \frac{\Delta G}{d} \quad (3.9)$$

For a grating with line density of 1200 l/mm, it was estimated that less than 1 μm of grating movement would cause the CE phase to change by $\sim 2\pi$ [131].

3.3.3 Carrier envelope phase stabilization for iFAST kHz CPA system

The setup for stabilizing the CE phase of the amplified laser pulses is shown in Figure 3.9. In the setup shown, the pulses from the oscillator were split by a 50:50 beam splitter. Half of the oscillator output was spectrally broadened by a photonic crystal fiber (PCF) before entering a f-to-2f setup to measure its CE phase value, while the other half went through the Pockels cell in order to select a 1-kHz pulse from the 80 MHz pulse train for the amplifier stages. The pulses then entered the Öffner stretcher to stretch to ~ 100 ps in order to avoid damaging the optics due to high intensity. The stretcher grating is mounted on a PZT mount for the grating shaking CE phase control scheme. The pulses then entered a 15-pass amplifier pumped by two Q-switched ND:YLF lasers. A double-pass Treacy compressor consisting of two gratings compressed the pulses to ~ 20 fs with a pulse

energy of 3.5 mJ [132].

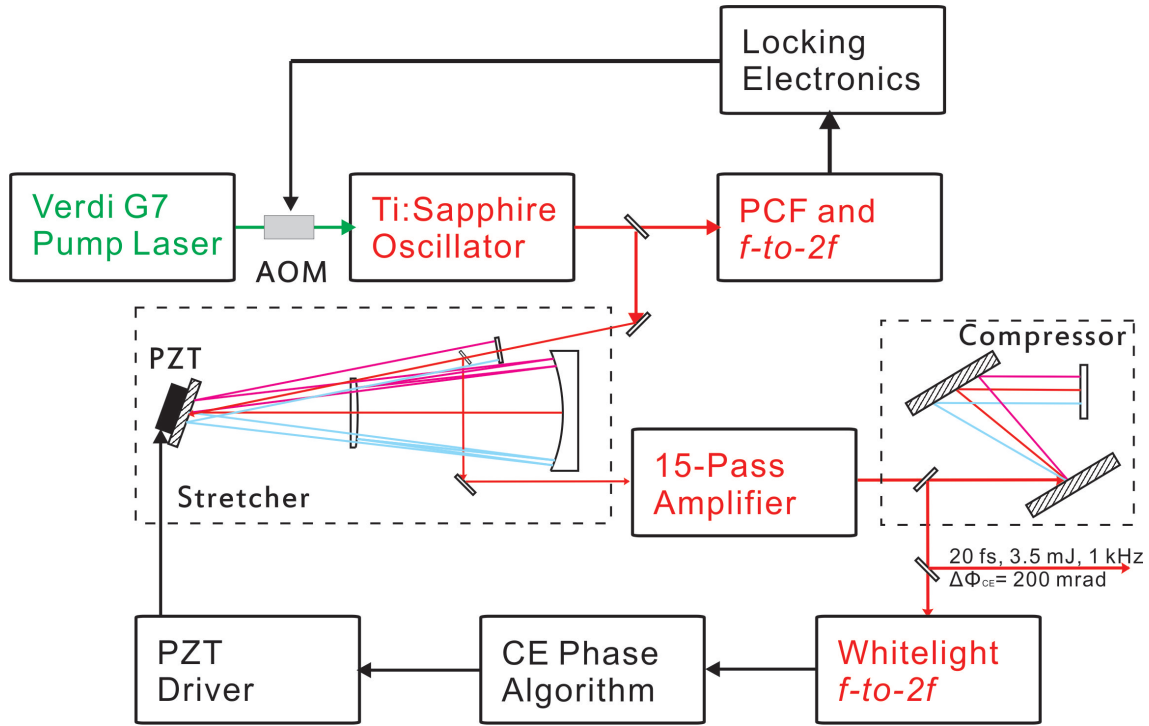
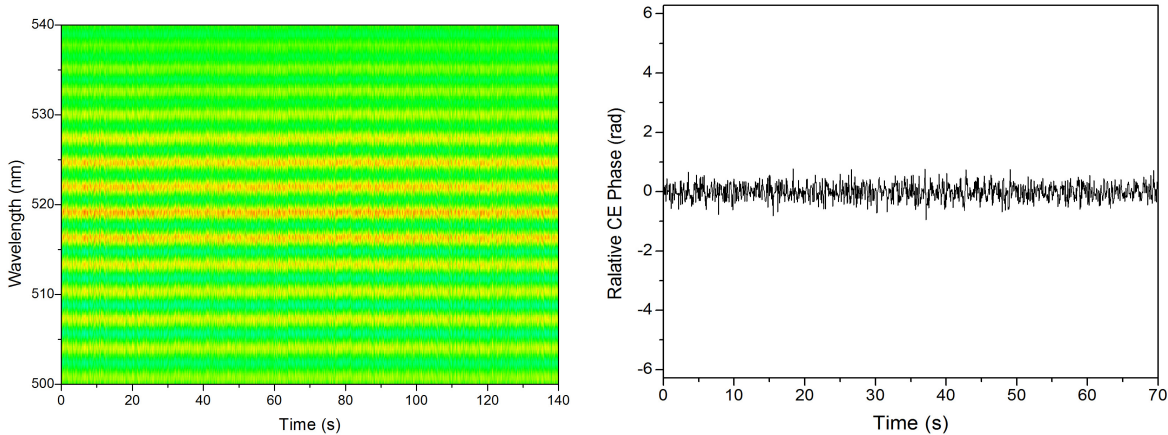


Figure 3.9: CE Phase stabilization for FAST kHz stage.

The output of the amplified laser pulses was sampled by a 5% beam splitter and sent to the f -to- $2f$. The fringe pattern was collected by the spectrometer and sent to a computer running a CE phase measurement algorithm. The error signal was sent to a PZT driver, which provided the driving voltage for the PZT in the stretcher; thus the grating separation could be varied to correct the CE phase drift. The result of the active PZT feedback control is shown in Figure 3.10, showing a CE phase rms error signal of 200 mrad for 50 ms integration time.



(a) Amplifier f-to-2f interference fringes

(b) Measured CE phase error when the feedback control was active.

Figure 3.10: Amplifier CE phase locking by grating shaking method.

Carrier-envelope phase control is not limited only to passively locking the CE phase at a fixed value, but more importantly to the variation of the CE phase to a desired time-dependent pattern. Sometimes scanning the CE phase over a certain range is more desirable for experiments that study the relationship between CE phase and the CE phase dependent physical processes. Figure 3.11 shows such a manipulation is performed over 7π CE phase by applying a modulation voltage to the PZT.

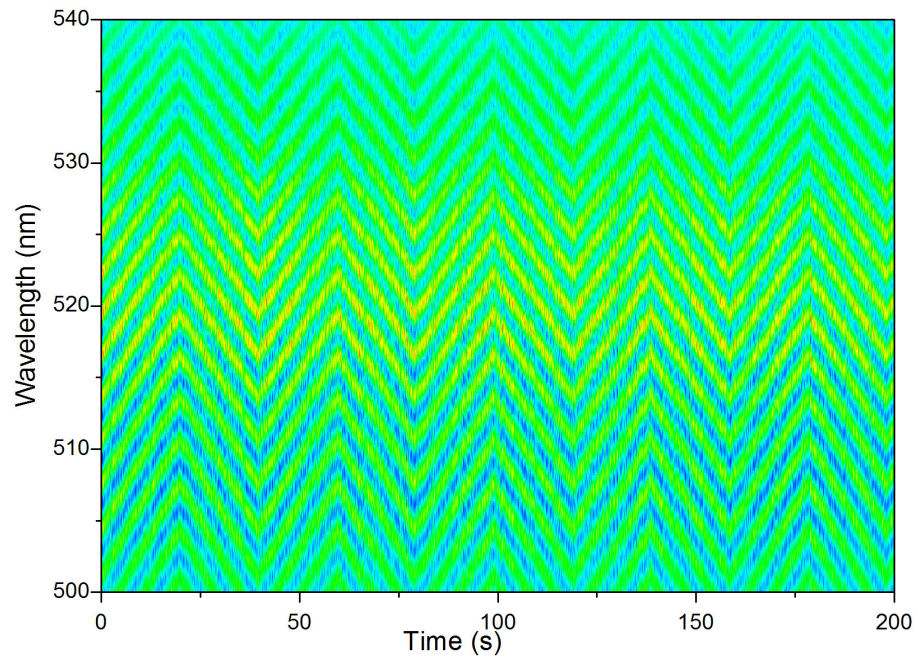


Figure 3.11: Temporal evolution of the interference fringes as controlling the CE phase of the amplified laser pulses by changing the PZT set point.

CHAPTER 4: HIGH FLUX ISOLATED ATTOSECOND PULSE GENERATION

The first isolated attosecond pulse was generated in 2001 by spectrally filtering HHG near the cutoff range using a Zr filter [133]. In this study, 7 fs, 0.5 mJ visible light pulses were used as the driving laser source [134]. Ideally, in order to increase the output energy of attosecond pulse, the first step is to increase the driving laser pulse energy. However few-cycle laser pulses are difficult to generate, especially in the high energy region. In 2008, our group developed the double optical gating (DOG) technique, which can be used to generate single attosecond pulses from 8 fs to 12 fs driving laser sources [135]. One year later, the generalized double optical gating (GDOG) technique further extended the boundary. Single attosecond pulses were produced directly by 28 fs pulses generated from a CPA laser system [2].

So far, all the attosecond experiments have been performed by combining one very weak (nJ energy level) attosecond pulse with a stronger femtosecond visible or near infrared pulse. The latter pulse is used to measure the birth of photoelectrons by streak field momentum kicks [136, 137] or to act as the pump pulse in transient absorption [138, 139]. Both experiments have limitations because of the high field effects of the femtosecond pulse and its considerably longer time duration relative to the attosecond pulse. Generating isolated attosecond pulses with sufficiently high pulse energies (100 nJ to 1 μ J) to perform attosecond-attosecond pump-probe measurements will make it possible to use one pulse to initiate a process and a second attosecond pulse to probe the time dynamics of the electron-correlation, either in transient absorption or by photoelectron spectroscopy. Two key reasons to pursue attosecond to attosecond measurements are to perform attosecond measurements on highly correlated materials for the first time and to extend attosecond x-ray dynamics measurements to solid-state semiconductor, magnetic, and plasmonic systems [140].

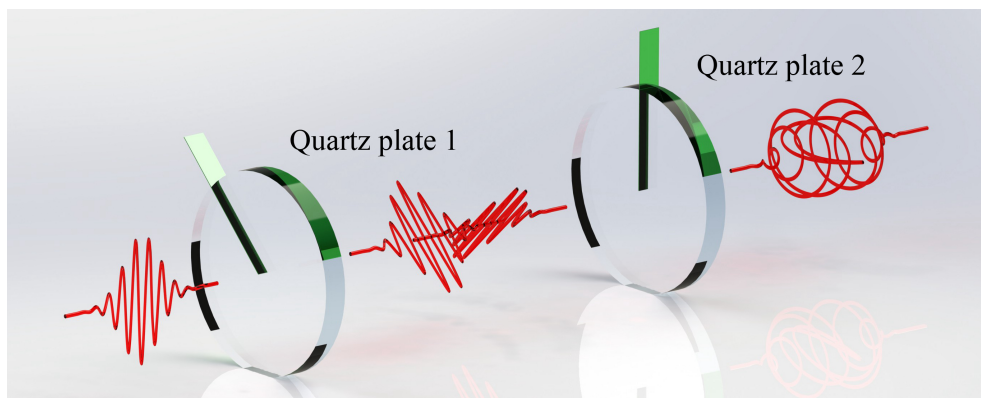
4.1 Attosecond Gating for Isolated Attosecond Pulse Generation

The field of attosecond science has progressed in recent years from the various gating techniques developed for generating isolated attosecond pulses. Three of the most common gating techniques – polarization gating (PG) [116, 141, 117, 142], two-color gating [143, 29], and DOG [144, 135, 145, 146] – allow the use of multicycle driving lasers to generate isolated attosecond pulses. Each gating method limits the attosecond pulse generation process by altering incident electric field to affect one of the three steps in the 3-step model.

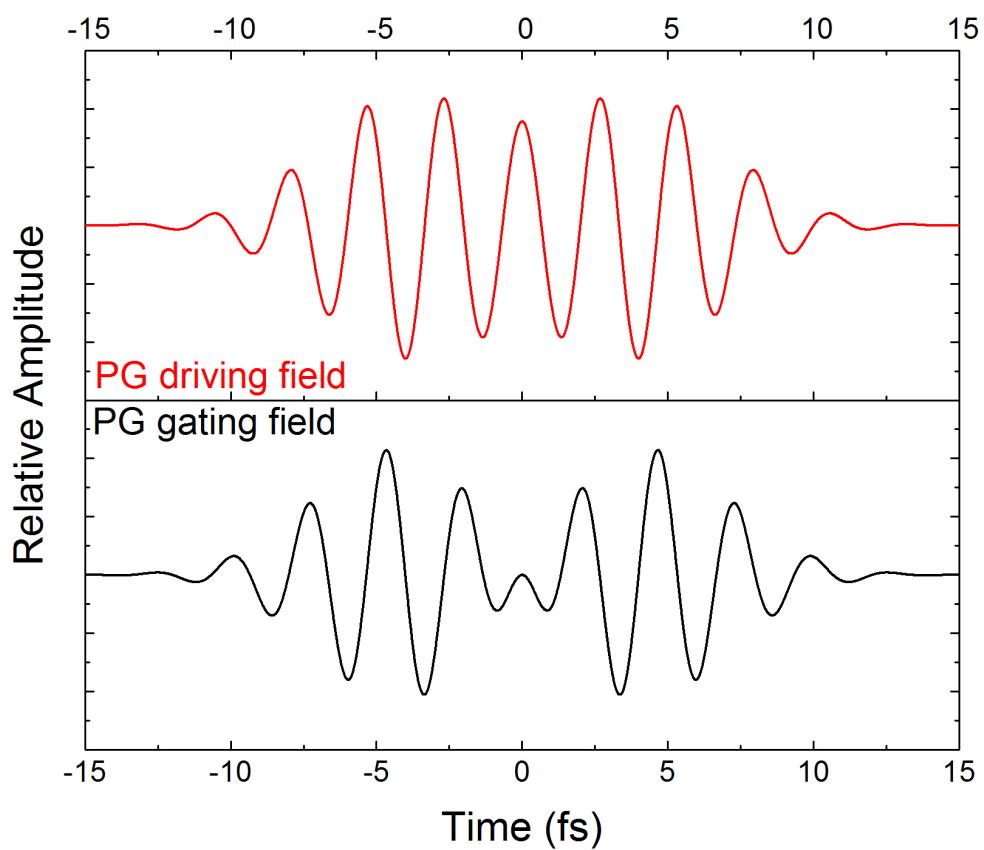
4.1.1 *Polarization gating and Two color gating*

It was shown that HHG yield exhibits strong dependence on the ellipticity of the generating laser [147, 148, 28]. As in the 3-step model, electrons accelerated linearly away from and towards the parent ion are most likely to recombine and emit high-order harmonics. If instead a circularly polarized electric field accelerates the electrons, then the recombination probability is very low, and attosecond pulse generation is prevented. By manipulating the ellipticity of the driving laser source, attosecond pulse generation can be limited to a single half cycle of the laser field, even when using a multi-cycle driving laser.

In order to implement polarization gating, birefringent optics are used to create a laser pulse that is only linearly polarized at one half cycle. Here, electron recombination is more probable, and an attosecond pulse is generated [116, 149]. Such a scheme is demonstrated in Figure 4.1.



(a) Optical components for polarization gating.



(b) Driving field (red line) and gating field (green line) components for polarization gating.

Figure 4.1: Polarization gating setup and its field components.

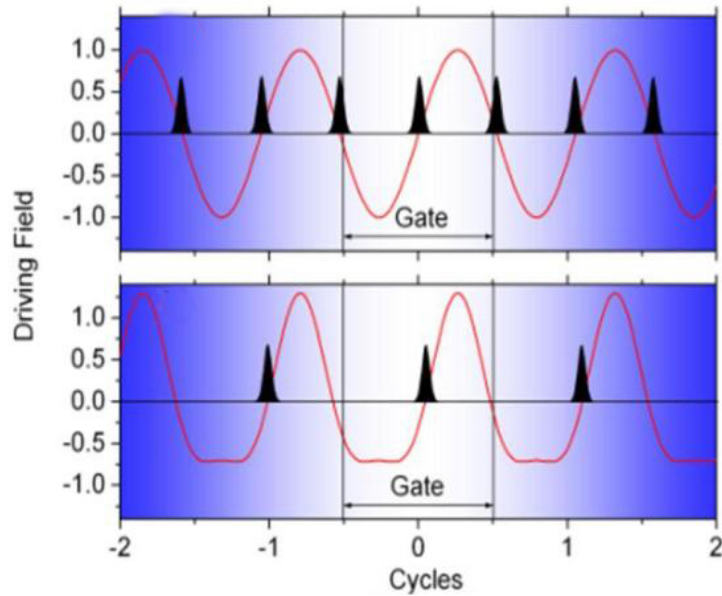
When a linearly-polarized pulse incidences on a full wave quartz plate with its optical axis axis rotated to 45° to the input driving laser polarization, two orthogonally polarized pulses – one along the ordinary axis and one along the extraordinary axis of the quartz plate – are created with a slight delay from one another. The quartz plate thickness is chosen such that the two pulse are slightly overlapped. Then a zero order quarter wave plate is set so that its optical axis is between the two pulses polarization, which changes the orthogonal linearly-polarized pulses to oppositely-rotating circularly-polarized pulses. The superposition of these two pulses in the overlap region gives a short period of linear polarization useful for single attosecond pulse generation. Polarization gating has been demonstrated to be successful at generating isolated ~ 130 as pulses using phase-stabilized 5-femtosecond driving pulses [29].

One the other hand, adding a second harmonic field to the fundamental driving laser will also change the electron trajectory when it is pulled away by the laser field from the parent ion during the HHG process. The two-color gating technique [142, 143, 150] is developed on this idea to reduce the periodicity of attosecond pulse generation from half-cycle to full-cycle separation. This can be understood by superimposing the second harmonic field on top of driving laser, since the period of the SHG is two times of that of the fundamental, the electric field going one direction gets enhanced while the other one is reduced. Since tunneling ionization is a nonlinear process, a small difference in the generation condition can lead to a significant change in the yield of free electrons. By adjusting the field strength of the SHG, the burst of tunneling ionization in the 3-step model can be limited to every other half cycle of the fundamental driving field. Attosecond pulse generation at the neighboring half cycles is suppressed because fewer free electrons are available for recombination.

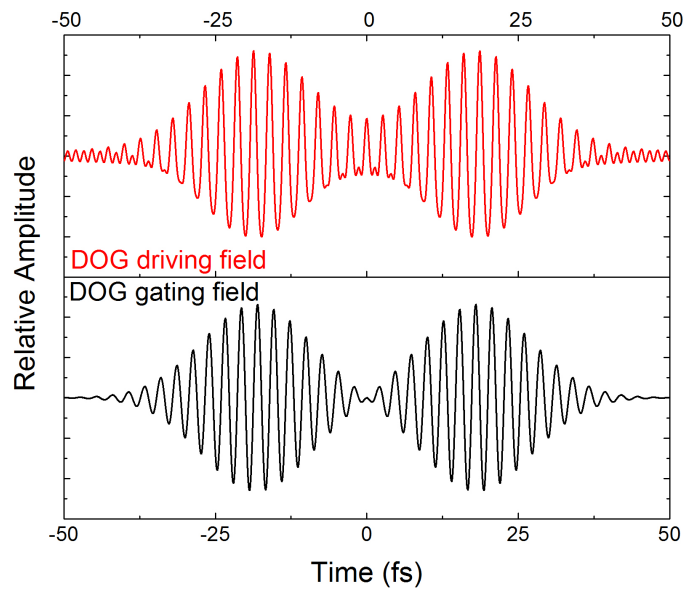
4.1.2 *Double optical gating*

Both PG and two color gating method require few-cycle femtosecond laser pulses with precisely controlled CE phase for single attosecond pulse generation. For generating 80 as attosecond pulses, a CE phase locked, 3.3 fs driving laser was used [27]. The requirement of CE phase stabilized few-cycle laser pulses restricts the attosecond science research.

The double optical gating (DOG) method was introduced a few years ago by our group to reduce this requirement [135, 146]. As a combination of PG and two color gating, DOG adds a weak second harmonic field to the driving field of PG. This allows attosecond pulse generation at full cycle separation instead of half cycle, which releases the half cycle constraint on the width of the polarization gate. This method is illustrated in Figure 4.2. With the DOG method, driving lasers with much longer pulse duration can be used to produce single attosecond pulses than previously allowed by the PG method. In the scenario of same driving pulse duration, DOG allows a wider gate width, which means the delay between the two counter-rotating pulses can be reduced. Reduced delay will not only suppress the depletion of the gas target as a result of less pulse energy in the leading edge, but also preserve more pulse energy in the linear gate allowing higher XUV photon yield [146].



(a) Attosecond pulse train in linear driving field with one color (a) and two color (b).



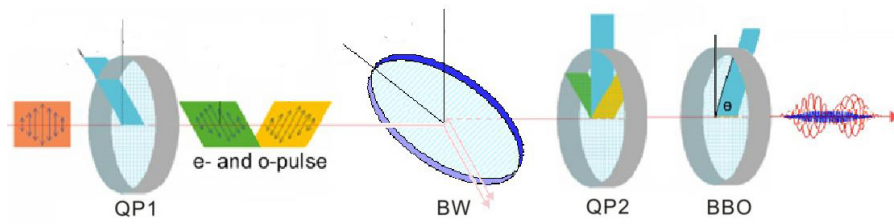
(b) DOG driving field (red) and gating field (black).

Figure 4.2: The SH field breaks the driving field symmetry, and electron ionization occurs with one cycle separation instead of half cycle separation.

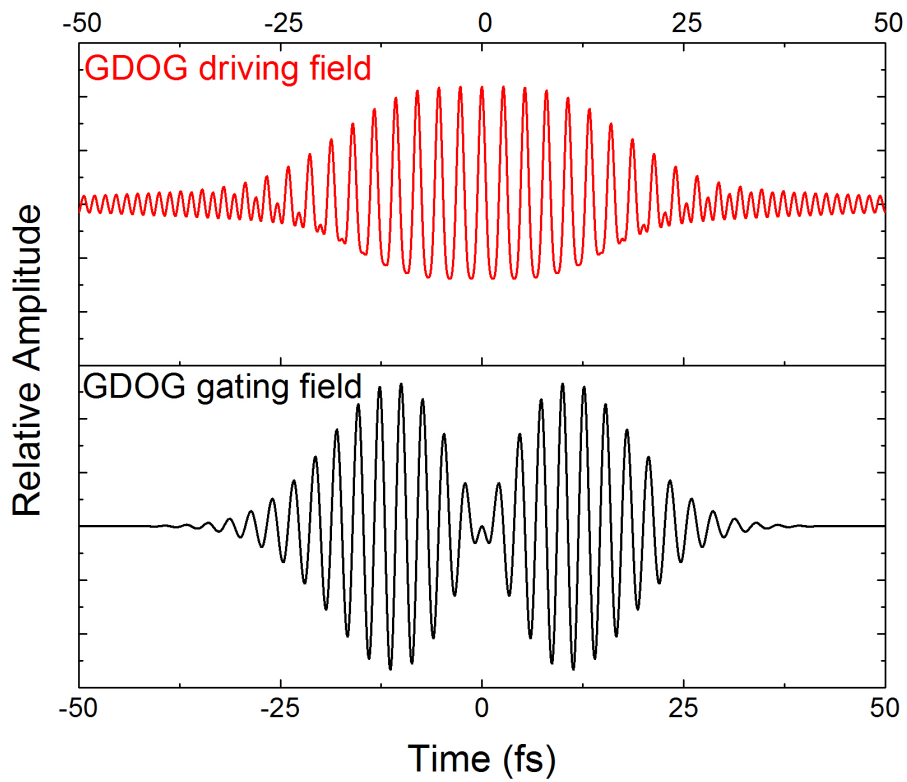
While these pulses are substantially easier to generate and work with experimentally, they still require a hollow-core fiber and chirped mirror compressor after the CPA amplifier for pulse duration compression to below 10 fs. As a result of limited driving laser energy, the flux of the isolated attosecond pulses is ~ 100 pJ to 1 nJ. For nonlinear attosecond physics and attosecond pump–attosecond probe experiments, the flux should approach the μ J level.

4.2 GDOG for Single Attosecond Pulse Generation from Multi-Cycle Driving Lasers

Generalized double optical gating (GDOG) is the variant of DOG to adapt attosecond pulse generation for multi-cycle driving lasers. One or more Brewster windows are inserted after the DOG first quartz plate to create a superposition of right and left elliptically-polarized pulses as in Figure 4.3. The GDOG scheme was found to reduce the leading edge ionization further than circularly polarized pulses by virtue of the introduced ellipticity [33].



(a) Implementation of generalized double optical gating.



(b) GDOG driving (red) and gating field (black).

Figure 4.3: GDOG allows even less delay between two elliptically polarized pulses comparing to DOG due to the reduced driving field amplitude.

4.2.1 GDOG gate width analysis

The ellipticity dependent pulse for the generalized double optical gating can be decomposed into two orthogonally polarized components known as the driving field (equation 4.1) and the gating field (equation 4.2). The gating field is zero at the center of the pulse, while the driving field is not zero. This resulting in a one cycle or shorter linear polarized laser field, its length is the gate width for the attosecond pulse generation.

$$E_{drive}(t) = E_0\varepsilon[e^{-2\ln(2)(\frac{t-T_d/2}{\tau_p})^2} + e^{-2\ln(2)(\frac{t+T_d/2}{\tau_p})^2}]\cos(\omega_0t + \varphi_{CE}), \quad (4.1)$$

$$E_{gate}(t) = E_0\varepsilon[e^{-2\ln(2)(\frac{t-T_d/2}{\tau_p})^2} - e^{-2\ln(2)(\frac{t+T_d/2}{\tau_p})^2}]\sin(\omega_0t + \varphi_{CE}), \quad (4.2)$$

where ε is the ellipticity of elliptically polarized pulses generated by the GDOG optics, τ_p is the laser pulse duration, φ_{CE} is the CE phase, ω_0 is the carrier frequency, and T_d is the delay between the left and right elliptically polarized pulses created by the first quartz plate. The time dependent ellipticity of the pulse $\xi(t)$ is the ratio between the gating field and the driving field:

$$\xi(t) = \min \left[\frac{\left| 1 - e^{-4\ln(2)\frac{T_d}{\tau_p^2}t} \right|}{\varepsilon \left[1 + e^{-4\ln(2)\frac{T_d}{\tau_p^2}t} \right]}, \frac{\varepsilon \left[1 + e^{-4\ln(2)\frac{T_d}{\tau_p^2}t} \right]}{\left| 1 - e^{-4\ln(2)\frac{T_d}{\tau_p^2}t} \right|} \right]. \quad (4.3)$$

The Taylor expansion $\xi(t)$, equation 4.3, at the center of the pulse where the laser field is linear:

$$\xi(t) = \left| 2\ln(2) \frac{T_d}{\varepsilon\tau_p^2 t} \right|. \quad (4.4)$$

Solving equation 4.4 for t is the gate width equation:

$$\delta t_G = \varepsilon \frac{\xi_{th}}{\ln(2)} \frac{\tau_p^2}{T_d}, \quad (4.5)$$

where $\xi_{th} \approx 0.2$ is the threshold ellipticity for HHG in Ar. As an example, for a 25 fs laser pulse with center wavelength of 780 nm, the calculated T_d is ~ 47 fs for $\varepsilon = 0.65$, which is equivalent to the delay between the fast and slow axis for a 1260 μm thick quartz plate. The GDOG method was shown to work with the 28 fs direct output of a CPA amplifier, and pulses of 148 as in duration were recorded [32].

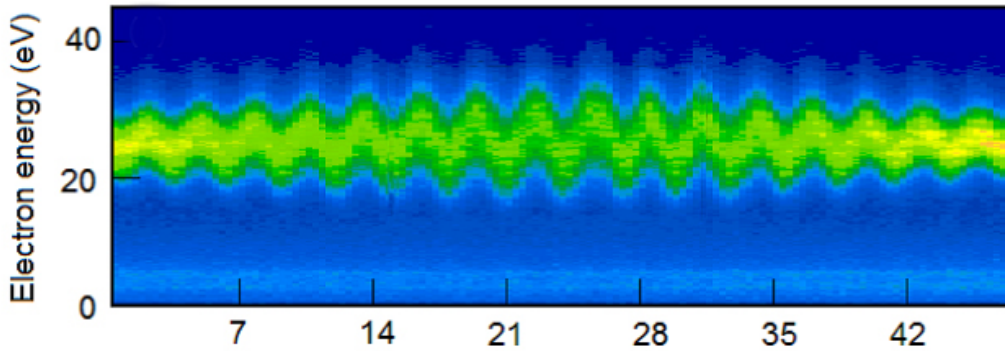


Figure 4.4: Attosecond pulse streaked spectrogram from 25 fs laser pulse.

Figure 4.4 shows streaking trace for attosecond pulse measurement from a 25 fs laser pulse using attosecond streak camera [151]. The full temporal characterization of this pulse is shown in Figure 4.5. The pulse duration of 163 as is close to the transform limited pulse duration [2].

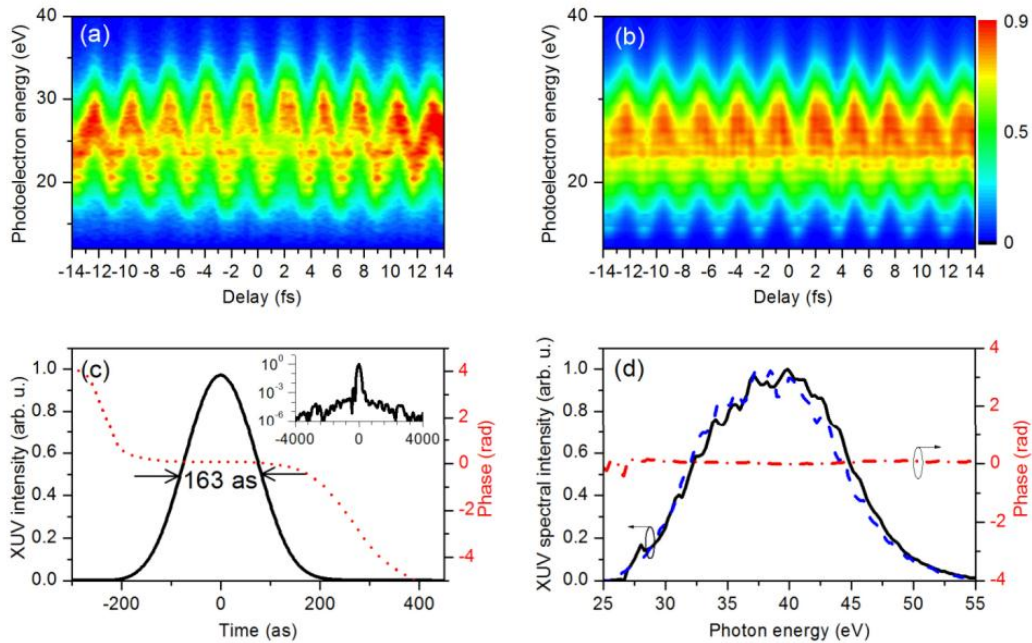


Figure 4.5: The experimentally obtained (a) and retrieved (b) streaking traces from a 25 fs driving laser with argon as the generation gas. (c) The retrieved temporal pulse (black line) and phase (red dotted line). (d) The measured (blue dotted line) and retrieved spectrum (black line) and phase (red line). Figure adapted from Ref. [2].

The GDOG method generated attosecond pulses with 170 pJ pulse energy from a driving laser pulse energy of ~ 1 mJ. Since the pulse energy of CPA amplifiers can reach tens of joules, GDOG is scalable to use higher driving laser energies. If the GDOG method were applied to PW driving lasers, the attosecond pulse energy could achieve previously unattainable levels.

4.2.2 Single atom ionization probability analysis

In order to generate the appropriate gate width with polarization gating, double optical gating or generalized double optical gating, a large portion of the input laser pulse is sacrificed. The leading and trailing edges of the pulse do not contribute to the HHG process but deplete the ground state of the gas target.

Since the returning electrons must recombine with the ground state for the XUV emission according to the three step model, the HHG flux is voided when the ground state is no longer populated. The generation of a harmonic with the frequency Ω is governed by the Fourier transform of the dipole transition matrix element [152]:

$$D(\Omega) = \int_{-\infty}^{\infty} \exp(i\Omega t) d(t) dt, \quad (4.6)$$

where the dipole transition matrix element is given by:

$$d(t) = \int \Psi_f(\mathbf{r}, t) * \hat{d}_e \Psi_i(\mathbf{r}, t) d^3t, \quad \hat{d}_e = \epsilon \cdot \mathbf{r}. \quad (4.7)$$

For HHG, Ψ_i is the ground state. If the laser intensity causes too much ground state depletion $d(t) = 0$, then there will be no XUV flux generated in the gate.

To quantify when the ground state is depleted, an ADK calculation was conducted for polarization gating, double optical gating and generalized double optical gating over different input pulse durations [153]. For a single atom excited by an intense laser field, the average ionization rate over

one optical cycle is:

$$W(t) = I_p |C_{n^*l^*}|^2 G_{lm} \left(\frac{4(2I_p)^{3/2}}{E(t)} \right)^{2n^* - |m| - 1} \exp \left(\frac{-2(2I_p)^{3/2}}{3E(t)} \right), \quad (4.8)$$

where

$$|C_{n^*l^*}|^2 = \frac{2^{2n^*}}{n^* \Gamma(n^* + l^* + 1) \Gamma(n^* - l^*)}$$

$$G_{lm} = \frac{(2l + 1)(l + |m|)!}{2^{|m|} |m|! (1 - |m|)!}$$

Figure 4.6 shows a plot of the ionization probability as a function of input laser pulse duration. The calculation assumes the gas target is argon, and the intensity of the laser in the gate width is $2.8 \times 10^{14} \text{ W/cm}^2$. In the half cycle gate width (1.3 fs) PG case, the red curve in Figure 4.6 shows that once the pulse duration of the input laser is greater than 6 fs, the target is fully ionized by the leading edge of the PG gated pulse. Thus, no HHG flux will be generated in the PG case with pulse duration greater than 6 fs. The DOG method requires the gate width to one full optical cycle (2.6 fs) for isolated attosecond pulse generation, as a result, the driving pulse duration can be increased as compared to half-cycle gate widths. The blue curve in Figure 4.6 indicates that DOG can work with pulses as long as 12 fs. Since even less delay is required for GDOG as compared to DOG, the reduction of delay between the two counter-rotating pulses further reduces the leading edge depletion as seen by the black curve in Figure 4.6. It is clearly seen that GDOG method should work for pulses longer than 15 fs. Since the ionization probability for GDOG is less than PG or DOG for all pulse duration, the target will be less depleted which eventually leads to a higher attosecond XUV flux.

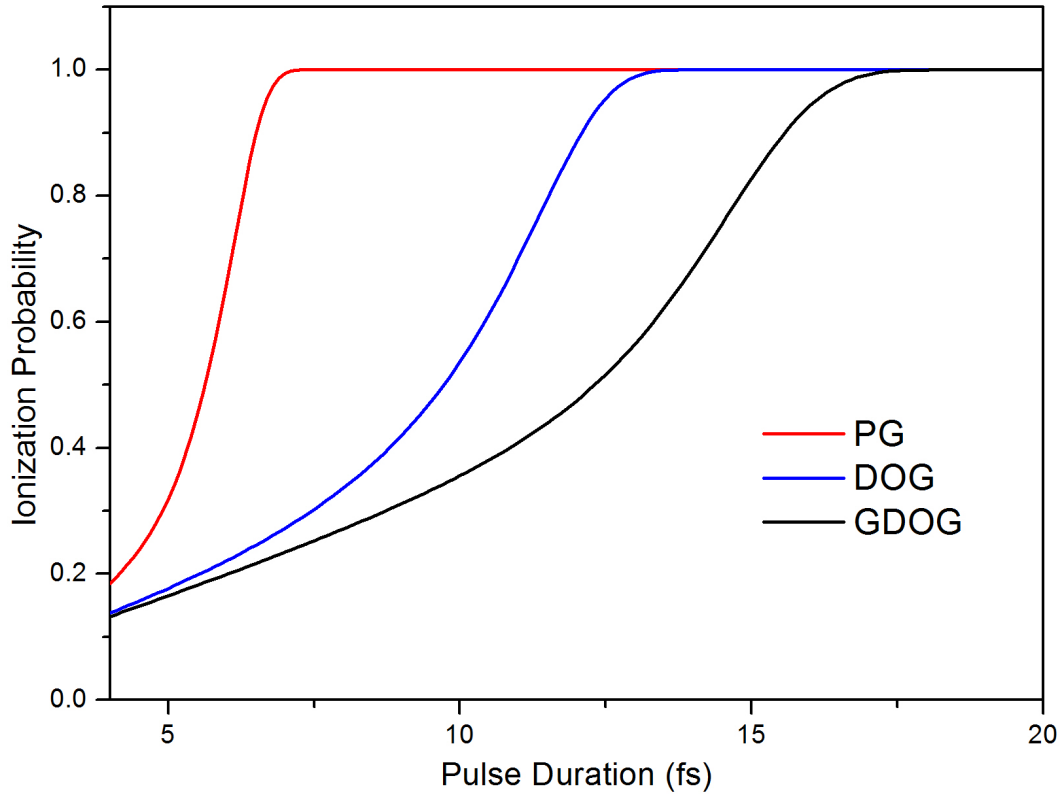


Figure 4.6: ADK calculation for PG, DOG and GDOG as a function of input pulse duration. The calculation assumes laser intensity of $2.8 \times 10^{14} \text{W/cm}^2$ with Argon as the generation gas.

The values in Table 4.1 are the required delays for several values of the input pulse duration as calculated by the gate width equation. The gate width is half optical cycle in all cases and $\epsilon = 0.6$.

Table 4.1: Gate Width for Generalized Double Optical Gating

τ_p (fs)	10.8	11.7	12.5	13.3	14	14.7	15.3	15.9	16.5
T_d (fs)	15.6	18.2	20.8	23.4	26	28.6	31.2	33.8	36.4
T_d (cycle)	6	7	8	9	10	11	12	13	14

4.2.3 Attosecond Pulses from Carrier Envelope Phase Unstabilized Lasers

In the process of scaling up the attosecond pulse energy by increasing the driving laser power, the CE phase requirement becomes harder to satisfy since high power laser systems usually operate at lower repetition rate. Such systems lack enough CE phase sampling to provide real time feedback for the phase locking mechanism [154, 155]. However, due to the nonlinear nature of the HHG process, the spectrum of an attosecond pulse can be significantly different with different CE phase value of the driving laser pulse [146, 149]. To overcome this problem, choosing a much narrower gate width – even less than one optical cycle – can make sure only one single attosecond pulse is generated.

For a gate width of ~ 1 fs, optical cycles far from the gate have nearly no chance of generating attosecond pulse. This leaves only one optical cycle closest to the gate the possibility to complete the 3-step process of attosecond pulse generation. However, HHG flux yield would be different since the ionization, propagation, and recombination probabilities vary for different CE phase value.

In order to validate this theory, streaking traces of single attosecond pulses generated by double optical gating were taken at four different CE phases. Figure 4.7 shows these traces generated

using a 9 fs driving laser and the DOG technique. The fringe pattern shifts their peak position for each CE phase value as expected. More importantly, at each value of CE phase, the XUV spectrum remains continuum but the signal level is different.

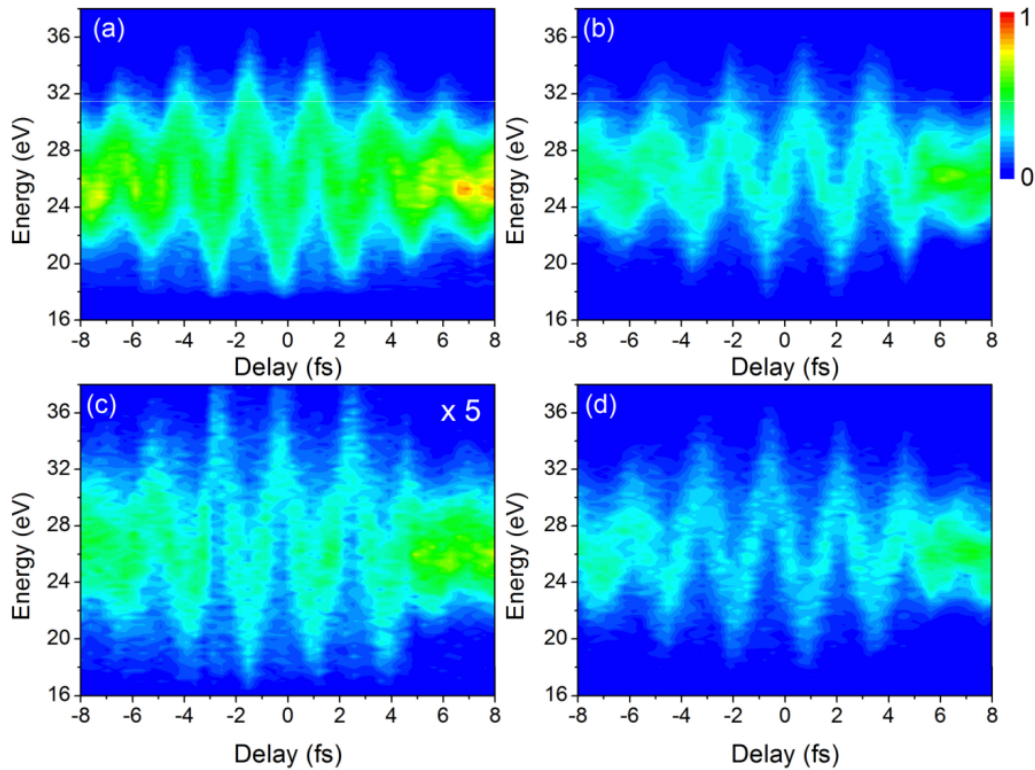


Figure 4.7: Streaked spectrograms for four different values of the input CE phase. Figure(a) is π , (b) is $\pi/2$, (c) is 0, and (d) is $3\pi/2$. Figure adapted from Ref. [3].

As a proof of the CE phase effect, Figure 4.8(a) shows a streaked trace for the case of the CE phase being unlocked. In Figure 4.8(b), the frequency-resolved optical gating for complete reconstruction of attosecond bursts (FROG-CRAB) retrieved pulse duration and phase, measuring it to be the same as the locked case [156, 157]. The uncertainty of the carrier wave peak position to the pulse envelope is the explanation for the extra cycle in the CE phase unlocked streaking trace [3].

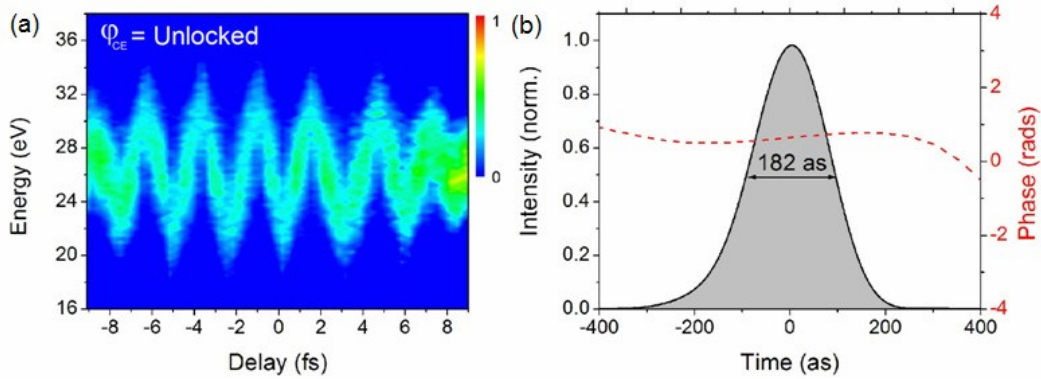


Figure 4.8: Streaked spectrogram from a CE phase unlocked pulse with the reconstructed temporal profile (solid line) and phase (dashed line). Figure adapted from Ref. [3].

The DOG technique was capable of generating isolated attosecond pulses with ~ 5 nJ of pulse energy [146]. In order to conduct attosecond nonlinear experiments or attosecond pump – probe experiments, this is a starting point. By combining this GDOG method together with TW or even PW class laser systems, the isolated attosecond pulse energy can be greatly increased.

4.3 High-Flux Attosecond XUV Continuum Generation

The target of building a 20 TW level, sub 15 fs laser is to increase the yield of attosecond XUV generation through scaling up driving laser energy. However, isolated attosecond pulse generation with a TW driving laser is not trivial.

First, the focusing geometry commonly used with kHz mJ level driving laser systems is no longer valid: if a short focal length is used, the laser intensity in the focal spot area far exceeds $< 10^{15} \text{ W/cm}^2$. The target gas will be fully ionized at the laser pulse leading edge.

Second, the metal foil filter commonly used to block kHz residual driving laser would no longer be able to withstand the laser damage from TW level pulses.

Third, in order to avoid laser damage to XUV optics, the experiment can only be performed far away from the XUV where the residual driving laser diverges. For kHz experiments, toroid mirrors are usually used for XUV beam focusing since a grazing incidence angle increases the reflection efficiency of the XUV [158]. However, if the source is too far away from the target location, strong coma aberration will appear when focusing. The reduced XUV focal spot quality will eventually result in low on-target XUV intensity or poor resolution of the XUV spectrometer.

In order to adapt the XUV generation scheme to our powerful driving laser source, a long focal length mirror ($f=6.5$ m) was used, and the end-to-end distance of our XUV beam line is close to 15 m as in Figure 4.9.

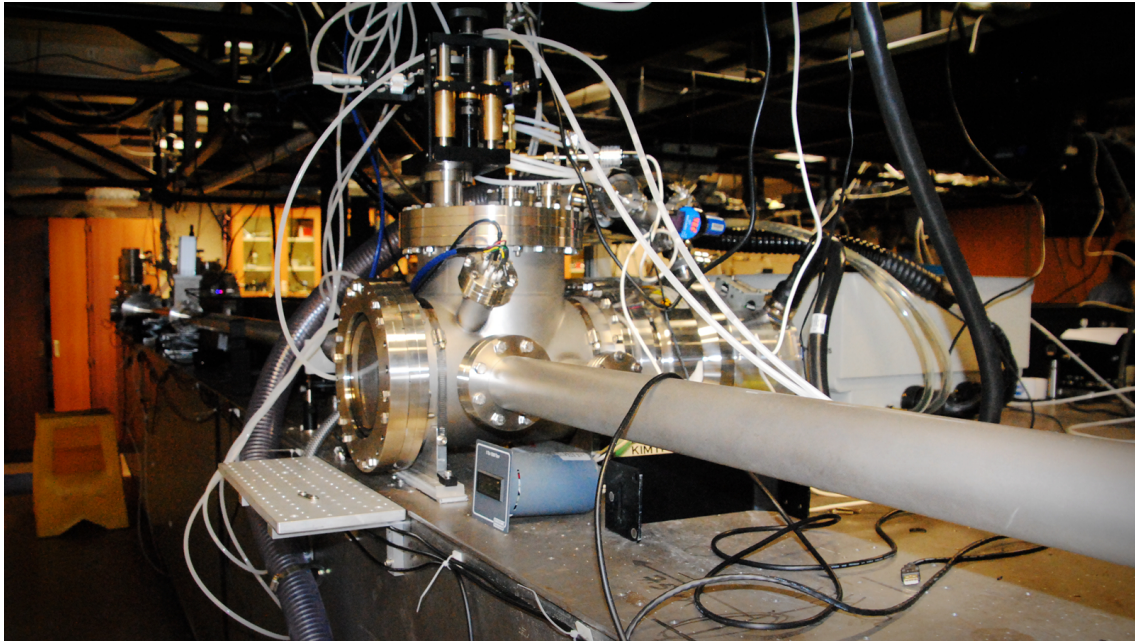


Figure 4.9: The attosecond beamline. The closer chamber on the right side of the photo is the HHG generation chamber.

4.3.1 *Phase matching for enhancing attosecond pulse photon flux*

High harmonic generation is a macroscopic process involving a large number of atoms. The HHG photon yield can only be scaled up when the attosecond XUV fields emitted by atoms located at different positions in the propagation direction of the driving laser are in phase so that they add up constructively. Improving the length over which the attosecond fields are phase matched – known as the coherent length – is one of the active areas of high harmonic and attosecond pulse generation research.

To estimate phase mismatch, we must start with what factors are contributing to Δk , as shown

in Eq. 1.5. The major terms contributing to phase mismatch for q th harmonic generation are the material dispersion, focusing geometry, atomic dipole phase, plasma density, and any nonlinear effects:

$$\Delta k(\omega) = \Delta k_{disp}(\omega) + \Delta k_{geom}(\omega) + \Delta k_{dipole}(\omega) + \Delta k_{plasma}(\omega) + \Delta k_{other}(\omega). \quad (4.9)$$

The phase mismatch due to dispersion in neutral medium is,

$$\Delta k_{disp}(\omega) = (n(\omega_f) - n(q\omega_f)) \frac{q\omega_f}{c} (1 - \eta), \quad (4.10)$$

where n is the refractive index and η is the ionization level due to laser intensity [159]. Since the gas refractive index for the IR driving laser wavelength is always larger than that of XUV wavelength, the resulting phase mismatching is always a positive number. There are ways to manipulate the refractive index by mixing of different gases or the application of controlling light fields [160].

Due to the high intensity of the input driving laser, a certain amount of neutral atoms will be ionized, and the free electrons will exist for a long time compared to the duration of the laser pulse (fs \ll several ns). This leads to a change in the refractive index due to plasma generation [161]:

$$n_{plasma}(\omega) = \sqrt{1 - \left(\frac{\omega_p}{\omega}\right)^2}, \omega_p = \sqrt{\frac{e^2 n_e}{\epsilon_0 m_e^*}}, \quad (4.11)$$

where ω_p is the plasma frequency, n_e is the number density of electrons, e is the electric charge, m_e^* is the effective mass of the electron, and ϵ_0 is the permittivity of free space.

The phase mismatching from the plasma contribution is

$$\Delta k_{plasma}(\omega) = qk_{plasma}(\omega_f) - k_{plasma}(q\omega_f) = \frac{\omega_p^2(1 - q^2)}{2qc\omega f}. \quad (4.12)$$

It is easy to see that the phase mismatching from plasma is a negative value.

The focusing geometry of the driving laser is another source of phase mismatching. The Gouy phase shift of the focused Gaussian beam is

$$\zeta(z) = \tan^{-1}\left(\frac{z}{z_R}\right) \approx \frac{1}{z_R}, \text{ for } z \ll z_R, z_R = \frac{\pi w_0^2}{\lambda}, \quad (4.13)$$

where z_R is the Rayleigh length. The resulting phase mismatching due to this Gouy phase shift is:

$$\Delta k_{geom} = qk_{geom}(\omega_f) - k_{geom}(q\omega_f) = \frac{q}{z_R(1 + (\frac{z}{z_R})^2)} > 0. \quad (4.14)$$

For generating attosecond pulses using TW or PW laser systems, loose focusing geometries are usually employed so that the resulting geometrical phase mismatching is small.

As discussed previously, the Fourier transform of the dipole matrix element governs the generation of a harmonic [162]. It was shown previously that the dipole moment can be written in terms of the quasi-classical action S as [163, 20, 164]:

$$\vec{x}(t) \propto \int_0^\infty \exp^{-iS(\vec{p}, t, \tau)} d\tau, \quad (4.15)$$

where τ is the time the electron makes the transition to the continuum with the canonical momentum $\vec{p} = \vec{v} + \vec{A}(t)$, t is the electron recombine time. The quasi-classical action $S(\vec{p}, t, \tau)$ describes

the motion of an electron moving freely in the laser field with a constant momentum \vec{p} :

$$S(\vec{p}, t, \tau) = \int_{\tau}^t \left(\frac{mv(t')^2}{2} + Ip \right) dt'. \quad (4.16)$$

The Fourier transform of Equation 4.15 gives the signal of the q th harmonic:

$$x_q = A_q \exp^{i\Phi_q}, \quad (4.17)$$

where A_q is an amplitude and $\Phi_q = (-S_q + \omega_q t)$ is the atomic dipole phase. Since there are both long and short trajectories, the dipole phase term can have two values. Since the action is primarily determined by the ponderomotive energy, for example $S(\vec{p}_s, t_s, \tau_s) \simeq U_p \tau_s + \dots$, the classical action integral Equation 4.16 can be written with a linear relationship to the laser intensity [20]. This simplifies the atomic phase to:

$$\Phi_i(r, z, t) = -\alpha_i I(r, z, t), \quad (4.18)$$

where the i refers to trajectories and α is the slope of the phase as a function of the intensity. From the atomic dipole phase term, the atomic wave vector mismatch Δk_{atom} can be calculated by differentiating Equation 4.18 with respect to the longitudinal position z :

$$\Delta k_{atom} = q\alpha I \left(\frac{2zz_r^2}{(z_r^2 + z^2)^2} \right). \quad (4.19)$$

Now every terms in Equation 4.9 has been derived. The result can be used to estimate the photon number generated for a particular harmonic order. The output energy for certain high harmonic orders is proportional to the square of the field strength of the corresponding harmonic. The field

strength of the q th harmonic in the one-dimensional model is given by:

$$dA_q(z)/dz = N_0 d(q\omega_0) F_q, \quad (4.20)$$

where $d(q\omega_0)$ is the induced atomic dipole moment, F_q is the phase-matching factor, and ω_0 is the frequency of fundamental driving laser. The phase-matching factor corresponds to $\exp^{i\Delta k z}$, where Δk is the total phase mismatch 4.9. If the absorption during propagation is ignored, the photon number N_q of the q th harmonic can be expressed as [165]:

$$N_q \propto N_0^2 L_{med}^2 |d(q\omega_0)|^2 \left[\frac{\sin(\frac{\Delta k L_{med}}{2})}{\frac{\Delta k L_{med}}{2}} \right], \quad (4.21)$$

where L_{med} is the medium length and N_0 is the neutral gas density. From Equation 4.21, the HHG photon yield is proportional to the squares of the gas density and the medium length under the phase matched condition. With increased coherent length, it is important to consider the effect of the gas target absorption [166]. The number of photons generated for the q th harmonic order can be estimated as [167]:

$$N_q \propto N_0^2 |d(q\omega_0)|^2 \frac{4(L_{abs} L_{coh})^2}{L_{coh}^2 + (2\pi L_{abs})^2} \times [1 + \exp(-\frac{L_{med}}{L_{abs}}) - 2 \cos(\frac{\pi L_{med}}{L_{coh}}) \exp(-\frac{L_{med}}{2L_{abs}})], \quad (4.22)$$

where $L_{coh} = \frac{\pi}{\Delta k}$ is coherence length, $L_{abs} = 1/2\alpha$ is absorption length, and α is the absorption coefficient for the q th harmonic. From Equation 4.22, it is evident that the coherence length should be longer than the absorption length to increase HHG photon yield. When the coherence length is much longer than both the absorption length and the medium length, the HHG photon yield follows:

$$N_q \propto |d(q\omega_0)|^2 z_0 (N_0 L_{med})^2 \propto S_{spot} (PL_{med})^2, \quad (4.23)$$

where S_{spot} is the spot size of the driving laser pulse at the generation location point and P is the target gas pressure. From Equation 4.23, the photon number generated in the HHG process is proportional to the driving laser beam size and the squares of the medium length and pressure. The photon yield is also proportional to the square of the dipole strength which follows [168]:

$$d(q\omega_0) \propto (1 - \eta)I_0^5, \quad (4.24)$$

where η is the ionization probability. The driving laser intensity should be maintained to avoid fully ionizing the generation gas.

In order to increase the interaction length between the laser pulse and the target gas without introducing too much phase mismatch from the Gouy phase shift, extending the Rayleigh length is one good option. Since the Gouy phase is given by

$$\Delta k_{gouy} = \frac{q}{z_R(1 + (\frac{z}{z_R})^2)} \quad (4.25)$$

increasing the Rayleigh length will reduce the Gouy phase shift. However, increased interaction length will also bring in additional effect from the geometry term in the phase matching equation. Thus, the gas pressure needs to be adjusted to cancel the geometrical phase shift of the driving laser to maintain a good phase-matched condition. Experimentally, this condition was realized by keeping a constant PL_{med} product. Furthermore, the energy of high harmonics will also benefit from the increase of the spot size of the driving pulses [169]. However, the driving laser intensity should be maintained in this process by increasing the pulse energy.

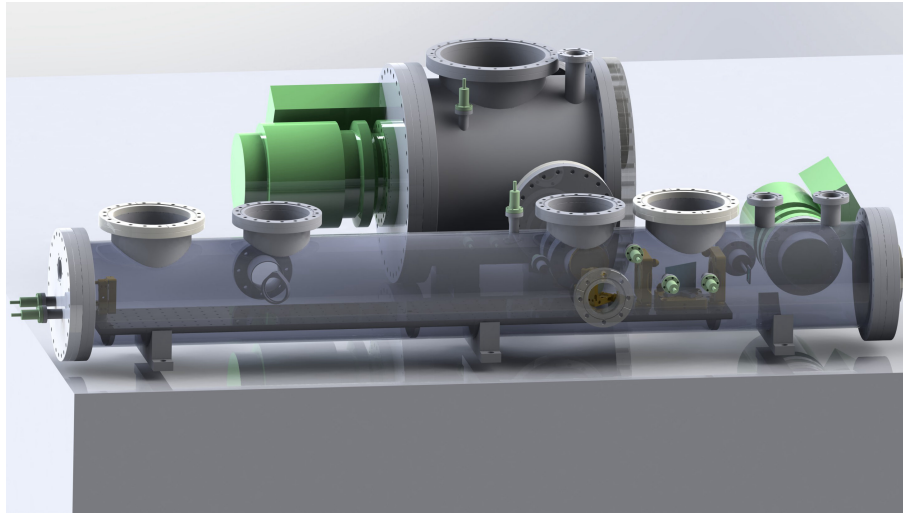
Other than loose focusing for HHG phase matching, alternative approaches have been proposed, such as a HHG in a hollow fiber. Additional terms like waveguide dispersion is included to address

the phase matching condition in the hollow fiber case [170]. In the long focusing limit, the loosely focused geometry becomes equivalent with the guided geometry [171]. In our experiment, to increase the spot size and the interaction length, the pump pulse was loosely focused with a 6.5 m dielectric coated concave mirror. The optimized gas pressure and medium length product was $\sim 500 \text{ torr} \times \text{mm}$.

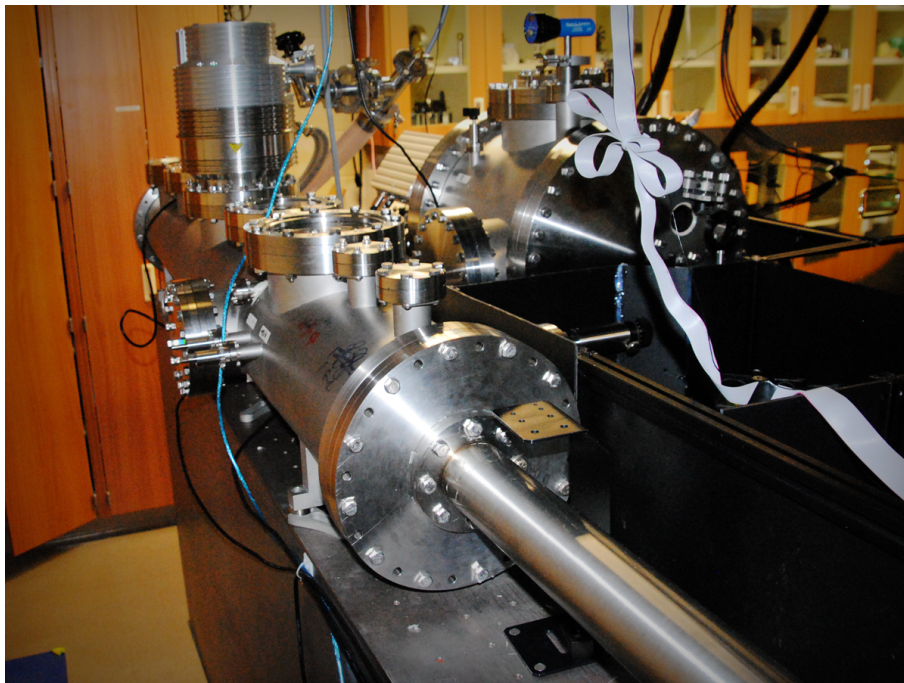
4.3.2 *GDOG gated attosecond pulse generation with TW driving laser*

For isolated attosecond pulse generation, the laser intensity in the gas target must be kept below the ionization saturation intensity, which is $< 10^{15} \text{ W/cm}^2$ for argon. Therefore, the high-power laser beam is loosely focused with a 6.5 m-focal length mirror. Figure 2.21 shows the focal spot profile with a line-out in both the vertical and horizontal direction. The diameter of the focal spot is 0.31 mm (FWHM). The corresponding long confocal length allows the usage of a long gas cell with low gas density, which showed high conversion efficiency in producing coherent femtosecond XUV pulses with HHG [94].

The laser field for GDOG is obtained by transforming the 14 fs linearly-polarized field with a set of birefringent optics. To achieve a gate width less than one optical cycle, the laser pulses are sent through a 1.070 mm quartz plate, three 0.3 mm BK7 Brewster windows, a 0.440 mm quartz plate, and a 0.141 mm barium borate crystal (BBO) located directly after the focusing mirror.



(a) Schematic drawing



(b) Laboratory photo

Figure 4.10: Chamber for TW beam focusing mirror and GDOG optics.

After the GDOG optics, the focused laser beam enters a 100 mm-long gas cell, where attosecond

pulses were generated in argon gas held at a pressure of 4 torr. Both ends of the cell were sealed with glass windows, each having 1 mm-diameter holes through which the NIR beam and XUV beam can pass.

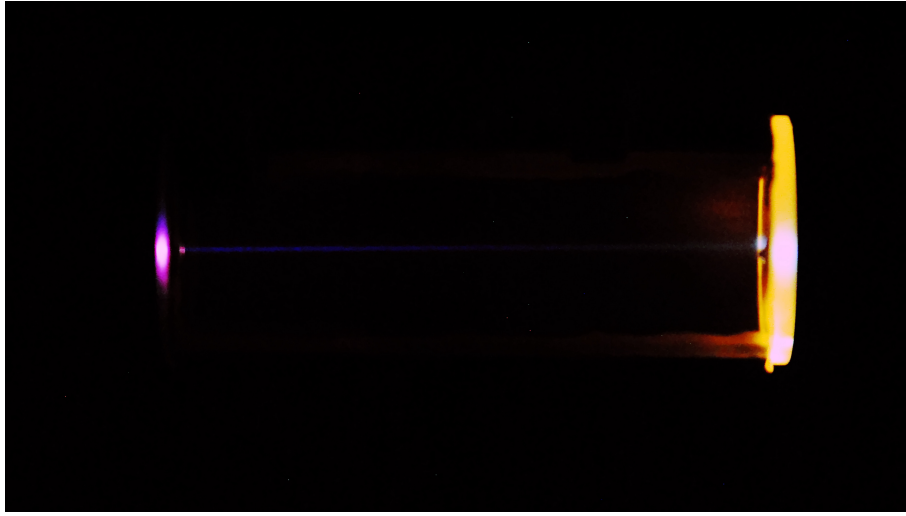
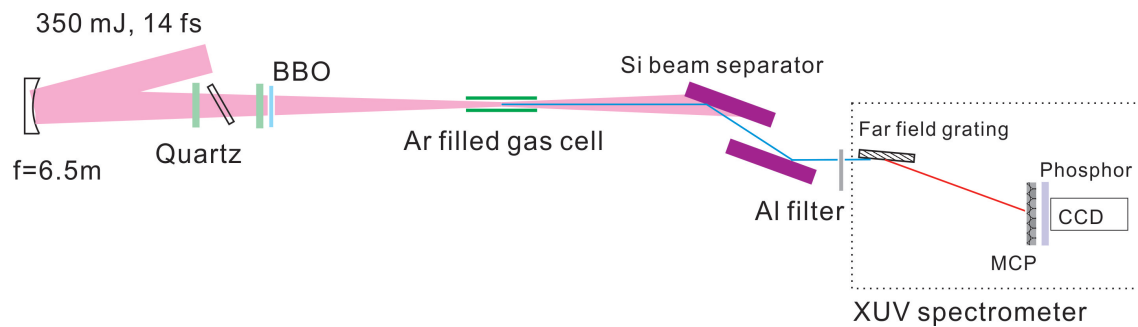
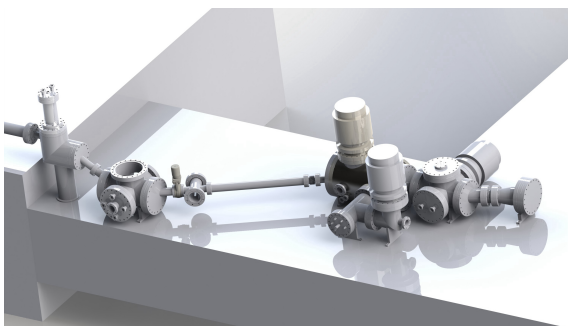


Figure 4.11: Filamentation induced by focusing 14 fs driving laser through the 10 cm long gas cell filled with Ar gas.

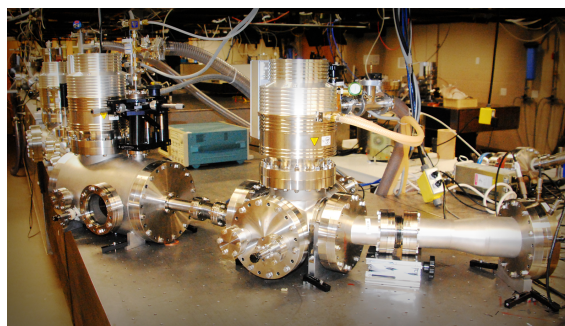
To eliminate the residual driving laser that propagates collinearly with the XUV light, the output beam from the gas cell was filtered by two silicon mirrors set at the Brewster angle of the NIR driving laser [172].



(a) Schematic of the attosecond pulse generation and measurement experiment.



(b) Design schematic of XUV spectrometer.



(c) Photo of XUV spectrometer chamber.

Figure 4.12: Setup for attosecond XUV generation and characterization.

A high resolution XUV grating spectrometer was used to measure the XUV spectra under various gating conditions. A grazing incidence, aberration corrected concave grating (Hitachi 001-0640 XUV) was used to form the flat field spectrograph [173, 174]. The dispersed XUV spectra was converted to fluorescence by a microchannel plate (MCP) and phosphor detector and finally captured shot-to-shot by a fast CCD camera working at a 10 Hz rate [175, 176, 177].

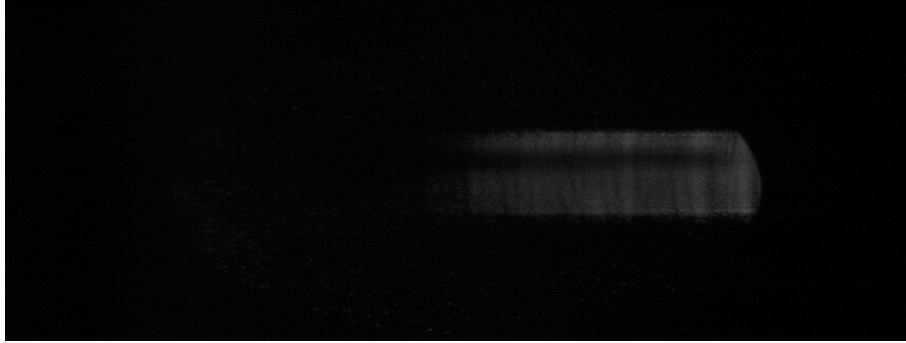


Figure 4.13: Raw single-shot XUV spectrum captured by CCD camera.

Figure 4.14 shows single-shot HHG spectra of argon while using no gating (800 nm linearly-polarized pulse), two-color gating (a second-harmonic field added to the linear fundamental field), and GDOG. As expected, well-resolved odd harmonics were generated when no gating was applied, and both odd and even harmonics appeared with the two-color laser field. These peaks merged to a continuum for every laser shot under the GDOG field – even without locking the carrier-envelope phase of the driving laser [178]. If the dispersion of the XUV spectrum were to be compensated to the Fourier-transform limit by an appropriate method, the corresponding pulse duration would be 230 as [37].

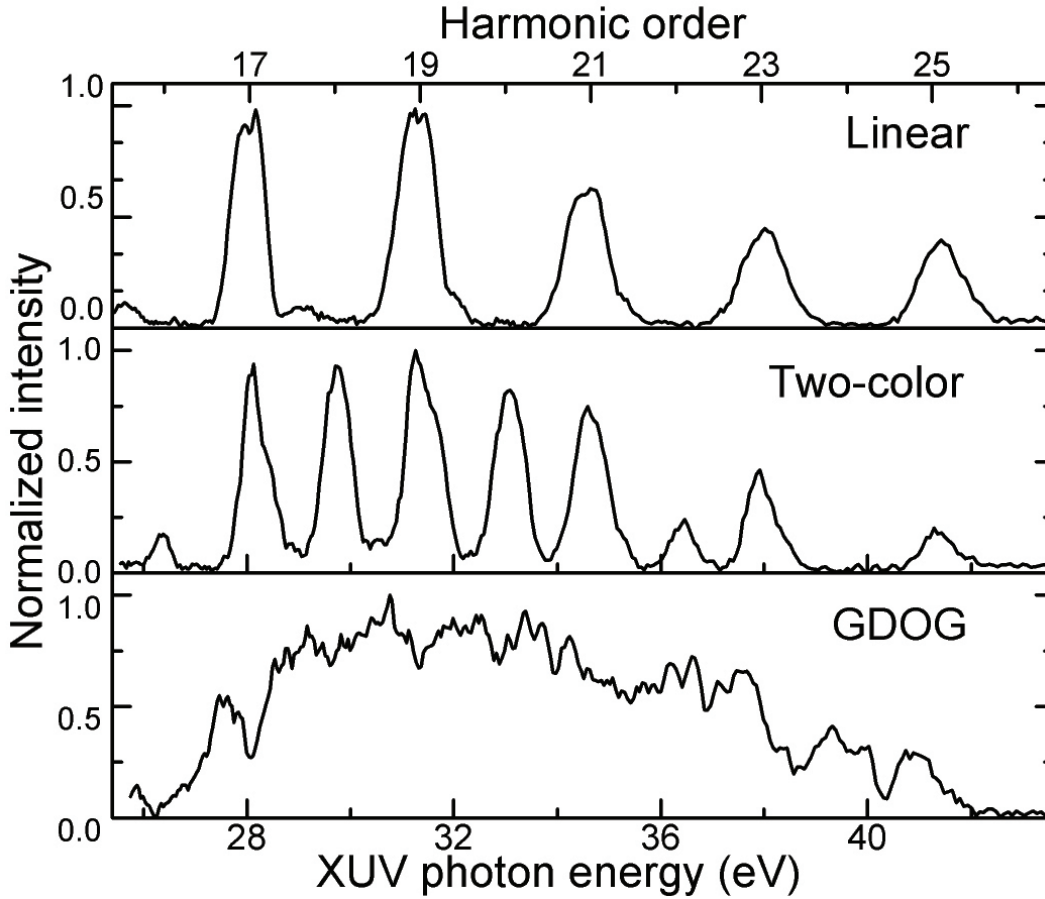


Figure 4.14: Single-shot XUV spectra generated in argon under different gating conditions.

In order to measure absolute XUV photon flux, an XUV photodiode has been used (AXUV576C, Opto Diode Corp [179]). This 24 mm by 24 mm size XUV photodiode is sensitive to XUV wavelengths from 200 to 0.07 nm with internal quantum efficiency of 100%. When the diode is exposed to photons with energy greater than 1.12 eV (the band gap width of silicon), one electron-hole pair is created per 3.63 eV. Mathematically, $N_e = E_{ph}/3.63$, where N_e is the number of electrons collected across the photodiode and E_{ph} is the energy of the XUV photon.

The photodiode was placed in vacuum after two 300 nm-thick aluminum filters. The signal from

the detector was recorded by a fast oscilloscope (Figure 4.15). The energy of the XUV pulse was measured to be 0.5 nJ. No photodiode signal from the residual driving laser was detected when the generation gas in the target is turned off. The measured XUV pulse energy corresponds to an estimated pulse energy at the exit of the gas cell of 100 nJ, assuming a 50% reflectance off each of the two silicon mirrors and a 2% total transmission through the two filters with 20 nm oxidation layers [180]. This result was verified that the energy signal went to zero when the Ar gas was removed from the interaction cell.

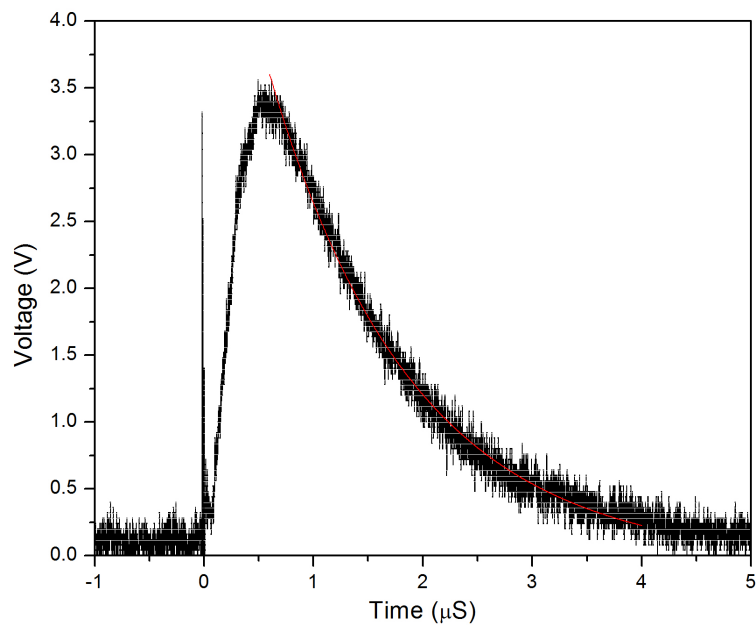


Figure 4.15: Oscilloscope signal of the XUV photodiode measurement for the GDOG-gated XUV spectrum.

CHAPTER 5: OUTLOOK AND CONCLUSIONS

Isolated attosecond pulses, especially at high flux, are difficult to produce, but their application to performing attosecond pump – probe experiments is much more straightforward. The attosecond pump – attosecond probe scheme requires isolated attosecond pulses with high photon flux. Works from the past few years have produced isolated attosecond pulses with 70 pJ [149], 500 pJ [27], and even 2 nJ on target [181].

In the process of boosting attosecond pulse energy to the required μ J level for attosecond pump – probe experiment, our 14 fs, 20 TW high power laser system at the Institute for the Frontier of Attosecond Science and Technology laboratory has been built and put to use. Combined with our GDOG technique for attosecond pulse generation, this laser source has demonstrated the ability to generate a continuous XUV spectrum supporting 230 as isolated attosecond pulses with pulse energy of 100 nJ.

As the journey goes on, the laser system at iFAST lab is currently being upgrading to a carrier-envelope phase-locked Ti:Sapphire double chirped pulse amplifier that operates at 10 Hz which will deliver 3 J, <15 fs 200 TW pulses for microjoule-level isolated attosecond pulse generation. The previously unattainable high XUV flux with attosecond pulse duration will allow us to explore many important areas in attosecond science. For instance, attosecond pump – attosecond probe experiments have been proposed to observe the valence- and inner-shell dynamics of electrons in krypton [182]. It will also enable other investigations such as nonlinear attosecond experiments [183] and attosecond transient absorption spectroscopy [184].

**APPENDIX A: SOURCE CODE FOR DEFORMABLE MIRROR PHASE
MODULATOR PHASE CORRECTION**

Matlab Code

The following Matlab code was used to optimize the OKO deformable mirror by processing the FROG trace as the fitness function. The code also includes reading CCD image data from a TEC cooled UV camera (QSI 520) [185].

”main.m”

```
1 %Main program for oko deformable mirror optimization
2 %Initial camera
3 global cam;
4 global position;
5 cam = actxserver ( 'QSIcamera.CCDcamera' );
6 cam.connected = 1;
7 cam.binx=2;
8 cam.biny=3;
9 cam.StartX=0;
10 cam.Numx=800;
11 cam.Nумы=400;
12 cam.CoolerOn = 1;
13 cam.FanMode = 1;
14 cam.SetCCDTemperature = 0;
15 %First fram
16 X0=x;
17 dmSet ([ X0,X0] );
18 cam.StartExposure (0.1 ,1);
```

```

19 pause(0.1);
20 display(num2str(cam.ImageReady));
21 data = get(cam, 'ImageArrayLong');
22 %Rectangular area
23 figure , imagesc(data);
24 h = imrect;
25 position = wait(h);
26 position = int16(position);
27 %Genetic algorithm optimization
28 options = gaoptimset('InitialPopulation',X0,'Generations',15,'
    PopulationSize',100,'PlotFcns', @gaplotbestfun);
29 nvars = 10; % Number of variables
30 LB = [0 0 0 0 0 0 0 0 0 0]; % Lower bound
31 UB = [4095 4095 4095 4095 4095 4095 4095 4095 4095 4095]; %
    Upper bound
32 IntCon = [1:10];
33 x=ga(@fitfrogga2 , nvars ,[] ,[] ,[] ,[] ,LB,UB,[], IntCon , options );
34 %Clear camera
35 cam.connected = 0;
36 cam.delete ;

```

```
"fitfrogga2.m"
```

```
1 function result=fitfrogga2(p)
2 %Mirror adjusting with FROG measurement
3 global cam;
4 global position;
5 dmSet([p,p]);
6 %Readout from camera
7 cam.StartExposure(0.1,1);
8 pause(0.1);
9 display(num2str(cam.ImageReady));
10 data = get(cam,'ImageArrayLong');
11 %Merit function
12 data(1e(data,500)) = 0;
13 data1=data(position(2):(position(2)+position(4)-1),position(1):(
    position(1)+position(3)-1));
14 data2=data(position(2):(position(2)+position(4)-1),position(1)
    -100:100+(position(1)+position(3)-1));
15 ce=sum(data1(:));
16 sdata=sum(data2(:));
17 fratio=-ce/sdata;
18 result=fratio
```

APPENDIX B: LIST OF ACRONYMS/ABBREVIATIONS

ADK M. V. Ammosov, N. B. Delone, and V. P. Krainov AOM Acousto-optical modulator
AOPDF Acousto-optical programmable dispersive filter
APD Avalanche photo diode
AR Anti-reflection
as Attosecond
ASE Amplified spontaneous emission
ATI Above threshold ionization
BBAR Broadband anti-reflection
BBO Beta barium borate
CE Carrier-envelope
CPA Chirped-pulse amplification
cw Continuous wave
DFG Difference frequency generation
DOE Diffractive optical element
DOG Double optical gating
FROG Frequency resolved optical gating
FS Fused silica
fs Femtosecond
FWHM Full width half maximum
FWOT Full wavelength optical thickness
GD Group delay
GDOG Generalized double optical gating
GNC Gain narrowing compensation
GVD Group velocity dispersion
HCF Hollow core fiber
HHG High harmonic generation

HWP Half-wave plate
IAP Isolated attosecond pulses
iFAST Institute for the Frontier of Attosecond Science and Technology
IR Infrared
KLM Kerr lens mode locked
KLS Kansas Light Source
LCD Liquid crystal display
 M^2 Beam quality parameter
MCP Multichannel plate
MIIPS Multiphoton intrapulse interference phase scan method
NIR Near infrared
OC Output coupler
OPA Optical parametric amplification or optical parametric amplifier
OPCPA Optical parametric chirped-pulse amplification
PC Pockels cell
PCF Photonic crystal fiber
PZT Lead zirconate titanate
PW Petawatt
QWP Quarter-wave plate
RF radio frequency
rms root mean square
SHG Second harmonic generation
SLM Spatial light modulator
SPM Self-phase modulation
TEC Thermoelectrical cooling THG Third harmonic generation
Ti Titanium

TOD Third order dispersion

TW Terawatt

UV Ultraviolet

XUV Extreme ultra-violet

YAG Yttrium aluminum garnet crystal

APPENDIX C: COPYRIGHT PERMISSIONS

**AIP PUBLISHING LLC LICENSE
TERMS AND CONDITIONS**

Nov 11, 2013

All payments must be made in full to CCC. For payment instructions, please see information listed at the bottom of this form.

License Number	3266020241126
Order Date	Nov 11, 2013
Publisher	AIP Publishing LLC
Publication	Applied Physics Letters
Article Title	Generation of high-flux attosecond extreme ultraviolet continuum with a 10 TW laser
Author	Y. Wu,E. Cunningham,H. Zang, et al.
Online Publication Date	May 21, 2013
Volume number	102
Issue number	20
Type of Use	Thesis/Dissertation
Requestor type	Author (original article)
Format	Print and electronic
Portion	Figure/Table
Number of figures/tables	3
Title of your thesis / dissertation	HIGH FLUX ISOLATED ATTOSECOND PULSE GENERATION
Expected completion date	Nov 2013
Estimated size (number of pages)	150
Total	0.00 USD

Terms and Conditions

AIP Publishing LLC -- Terms and Conditions: Permissions Uses

AIP Publishing LLC ("AIPP") hereby grants to you the non-exclusive right and license to use and/or distribute the Material according to the use specified in your order, on a one-time basis, for the specified term, with a maximum distribution equal to the number that you have ordered. Any links or other content accompanying the Material are not the subject of this license.

1. You agree to include the following copyright and permission notice with the reproduction of the Material: "Reprinted with permission from [FULL CITATION]. Copyright [PUBLICATION YEAR], AIP Publishing LLC." For an article, the copyright and permission notice must be printed on the first page of the article or book chapter. For photographs, covers, or tables, the copyright and permission notice may appear with the Material, in a footnote, or in the reference list.
2. If you have licensed reuse of a figure, photograph, cover, or table, it is your responsibility to ensure that the material is original to AIPP and does not contain the copyright of another entity, and that the copyright notice of the figure, photograph, cover, or table does not indicate that it was reprinted by AIPP, with permission, from another source. Under no circumstances does AIPP, purport or intend to grant permission to reuse material to which it does not hold copyright.
3. You may not alter or modify the Material in any manner. You may translate the Material into another language only if you have licensed translation rights. You may not use the Material for promotional purposes. AIPP reserves all rights not specifically granted herein.
4. The foregoing license shall not take effect unless and until AIPP or its agent, Copyright Clearance Center, receives the Payment in accordance with Copyright Clearance Center Billing and Payment Terms and Conditions, which are incorporated herein by reference.
5. AIPP or the Copyright Clearance Center may, within two business days of granting this

license, revoke the license for any reason whatsoever, with a full refund payable to you. Should you violate the terms of this license at any time, AIPP, AIP Publishing LLC, or Copyright Clearance Center may revoke the license with no refund to you. Notice of such revocation will be made using the contact information provided by you. Failure to receive such notice will not nullify the revocation.

6. AIPP makes no representations or warranties with respect to the Material. You agree to indemnify and hold harmless AIPP, AIP Publishing LLC, and their officers, directors, employees or agents from and against any and all claims arising out of your use of the Material other than as specifically authorized herein.
7. The permission granted herein is personal to you and is not transferable or assignable without the prior written permission of AIPP. This license may not be amended except in a writing signed by the party to be charged.
8. If purchase orders, acknowledgments or check endorsements are issued on any forms containing terms and conditions which are inconsistent with these provisions, such inconsistent terms and conditions shall be of no force and effect. This document, including the CCC Billing and Payment Terms and Conditions, shall be the entire agreement between the parties relating to the subject matter hereof.

This Agreement shall be governed by and construed in accordance with the laws of the State of New York. Both parties hereby submit to the jurisdiction of the courts of New York County for purposes of resolving any disputes that may arise hereunder.

If you would like to pay for this license now, please remit this license along with your payment made payable to "COPYRIGHT CLEARANCE CENTER" otherwise you will be invoiced within 48 hours of the license date. Payment should be in the form of a check or money order referencing your account number and this invoice number RLNK501156442.

Once you receive your invoice for this order, you may pay your invoice by credit card. Please follow instructions provided at that time.

**Make Payment To:
Copyright Clearance Center
Dept 001
P.O. Box 843006
Boston, MA 02284-3006**

For suggestions or comments regarding this order, contact RightsLink Customer Support: customer@copyright.com or +1-877-622-5543 (toll free in the US) or +1-978-646-2777.

Gratis licenses (referencing \$0 in the Total field) are free. Please retain this printable license for your reference. No payment is required.

wuyi

From: pubscopyright <copyright@osa.org>
Sent: Monday, November 11, 2013 3:13 PM
To: wuyi
Subject: RE: Copyright request for PhD thesis

Dear Yi,

Thank you for contacting The Optical Society.

Because you are the author of the source paper from which you wish to reproduce material, OSA considers your requested use of its copyrighted materials to be permissible within the author rights granted in the Copyright Transfer Agreement submitted by the requester on acceptance for publication of his/her manuscript. It is requested that a complete citation of the original material be included in any publication. This permission assumes that the material was not reproduced from another source when published in the original publication.

Please let me know if you have any questions.

Best,

Hannah

Hannah Bembia
November 11, 2013
Authorized Agent, The Optical Society

 OSA Light in Focus

From: wuyi [<mailto:wuyi@knights.ucf.edu>]
Sent: Sunday, November 10, 2013 11:17 PM
To: pubscopyright
Subject: Copyright request for PhD thesis

Dear Editors:

I am completing a doctoral dissertation at the University of Central Florida entitled "HIGH FLUX ISOLATED ATTOSECOND PULSE GENERATION". I would like your permission to reprint in my dissertation excerpts from the following:
H. Wang, Y. Wu, C. Li, H. Mashiko, S. Gilbertson, and Z. Chang. Generation of 0.5 mj, few-cycle laser pulses by an adaptive phase modulator. Opt. Express, 16(19):14448–14455, Sep 2008.

The excerpts to be reproduced include Figures 1,3,4 and portions of the text.

The requested permission extends to any future revisions and editions of my dissertation, including non-exclusive world rights in all languages. These rights will in no way restrict republication of the material in any other form by you or by others authorized by you. Your signing of this letter will also confirm that you or your company owns the copyright to the above-described material.

If these arrangements meet with your approval, please sign this letter where indicated below and return it to me by e-mail. Thank you for your attention in this matter.

1

Sincerely,
Yi Wu

APPENDIX D: LIST OF MY PUBLICATIONS

- [1] Y. Wu, E. Cunningham, H. Zang, J. Li, M. Chini, X. Wang, Y. Wang, K. Zhao, and Z. Chang. Generation of high-flux attosecond extreme ultraviolet continuum with a 10 TW laser. *Applied Physics Letters*, 102(20):201104–201104, 2013.
- [2] H. Wang, Y. Wu, C. Li, H. Mashiko, S. Gilbertson, and Z. Chang. Generation of 0.5 mj, few-cycle laser pulses by an adaptive phase modulator. *Opt. Express*, 16(19):14448–14455, Sep 2008.
- [3] S. Gilbertson, Y. Wu, S. D. Khan, M. Chini, K. Zhao, X. Feng, and Z. Chang. Isolated attosecond pulse generation using multicycle pulses directly from a laser amplifier. *PHYSICAL REVIEW A: atomic, molecular, and optical physics*, 81(4):43810, 2010.
- [4] H. Wang, M. Chini, Y. Wu, E. Moon, H. Mashiko, and Z. Chang. Carrier-envelope phase stabilization of 5-fs, 0.5-mj pulses from adaptive phase modulator. *Applied Physics B*, 98(2-3):291–294, 2010.
- [5] S. Chen, M. Chini, H. Wang, C. Yun, H. Mashiko, Y. Wu, and Z. Chang. Carrier-envelope phase stabilization and control of 1 khz, 6 mj, 30 fs laser pulses from a ti: sapphire regenerative amplifier. *Applied optics*, 48(30):5692–5695, 2009.
- [6] M. Chini, H. Mashiko, H. Wang, S. Chen, C. Yun, S. Scott, S. Gilbertson, and Z. Chang. Delay control in attosecond pump-probe experiments. *Opt. Express*, 17(24):21459–21464, 2009.
- [7] X. Feng, S. Gilbertson, H. Mashiko, H. Wang, S. D. Khan, M. Chini, Y. Wu, K. Zhao, and Z. Chang. Generation of isolated attosecond pulses with 20 to 28 femtosecond lasers. *Physical review letters*, 103(18):183901, 2009.
- [8] X. Feng, S. Gilbertson, S. D. Khan, M. Chini, Y. Wu, K. Carnes, and Z. Chang. Calibration of electron spectrometer resolution in attosecond streak camera. *Opt. Express*, 18:1316, 2010.

- [9] S. Gilbertson, M. Chini, X. Feng, S. Khan, Y. Wu, and Z. Chang. Monitoring and controlling the electron dynamics in helium with isolated attosecond pulses. *Physical review letters*, 105(26):263003, 2010.
- [10] H. Wang, M. Chini, S. Chen, C.-H. Zhang, F. He, Y. Cheng, Y. Wu, U. Thumm, and Z. Chang. Attosecond time-resolved autoionization of argon. *Physical review letters*, 105(14):143002, 2010.
- [11] S. Gilbertson, S. D. Khan, Y. Wu, M. Chini, and Z. Chang. Isolated attosecond pulse generation without the need to stabilize the carrier-envelope phase of driving lasers. *Physical review letters*, 105(9):093902, 2010.
- [12] K. Zhao, Q. Zhang, M. Chini, Y. Wu, X. Wang, and Z. Chang. Tailoring a 67 attosecond pulse through advantageous phase-mismatch. *Optics letters*, 37(18):3891–3893, 2012.
- [13] X. Wang, M. Chini, Q. Zhang, K. Zhao, Y. Wu, D. A. Telnov, S.-I. Chu, and Z. Chang. Mechanism of quasi-phase-matching in a dual-gas multijet array. *Physical Review A*, 86(2):021802, 2012.
- [14] B. Zeng, W. Chu, G. Li, J. Yao, J. Ni, H. Zhang, Y. Cheng, Z. Xu, Y. Wu, and Z. Chang. Direct generation of intense extreme-ultraviolet supercontinuum with 35-fs, 11-mj pulses from a femtosecond laser amplifier. *Physical Review A*, 85(3):033839, 2012.
- [15] M. Chini, X. Wang, Y. Cheng, Y. Wu, D. Zhao, D. A. Telnov, S.-I. Chu, and Z. Chang. Sub-cycle oscillations in virtual states brought to light. *Scientific reports*, 3, 2013.
- [16] X. Wang, M. Chini, Y. Cheng, Y. Wu, and Z. Chang. In situ calibration of an extreme ultraviolet spectrometer for attosecond transient absorption experiments. *Applied optics*, 52(3):323–329, 2013.

- [17] X. Wang, M. Chini, Y. Cheng, Y. Wu, X.-M. Tong, and Z. Chang. Subcycle laser control and quantum interferences in attosecond photoabsorption of neon. *Physical Review A*, 87(6):063413, 2013.

LIST OF REFERENCES

- [1] H. Wang, Y. Wu, C. Li, H. Mashiko, S. Gilbertson, and Z. Chang. Generation of 0.5 mj, few-cycle laser pulses by an adaptive phase modulator. *Opt. Express*, 16(19):14448–14455, Sep 2008.
- [2] S. Gilbertson, Y. Wu, S. D. Khan, M. Chini, K. Zhao, X. Feng, and Z. Chang. Isolated attosecond pulse generation using multicycle pulses directly from a laser amplifier. *PHYSICAL REVIEW A: atomic, molecular, and optical physics*, 81(4):43810, 2010.
- [3] S. Gilbertson, S. D. Khan, Y. Wu, M. Chini, and Z. Chang. Isolated attosecond pulse generation without the need to stabilize the carrier-envelope phase of driving lasers. *Physical review letters*, 105(9):093902, 2010.
- [4] T. H. Maiman. Stimulated Optical Radiation in Ruby. *Nature*, 187:493–494, August 1960.
- [5] T. H. Maiman, R. H. Hoskins, I. J. D’Haenens, C. K. Asawa, and V. Evtuhov. Stimulated optical emission in fluorescent solids. ii. spectroscopy and stimulated emission in ruby. *Phys. Rev.*, 123:1151–1157, Aug 1961.
- [6] P. Maine, D. Strickland, P. Bado, M. Pessot, and G. Mourou. Generation of ultrahigh peak power pulses by chirped pulse amplification. *Quantum Electronics, IEEE Journal of*, 24(2):398–403, feb 1988.
- [7] D. Strickland and G. Mourou. Compression of amplified chirped optical pulses. *Optics Communications*, 55:447–449, October 1985.
- [8] C. P. J. Barty, G. Korn, F. Raksi, C. Rose-Petruck, J. Squier, A.-C. Tien, K. R. Wilson, V. V. Yakovlev, and K. Yamakawa. Regenerative pulse shaping and amplification of ultrabroadband optical pulses. *Opt. Lett.*, 21(3):219–221, Feb 1996.

- [9] K. Yamakawa, M. Aoyama, S. Matsuoka, T. Kase, Y. Akahane, and H. Takuma. 100-tw sub-20-fs ti:sapphire laser system operating at a 10-hz repetition rate. *Opt. Lett.*, 23(18):1468–1470, Sep 1998.
- [10] V. Bagnoud and F. Salin. Amplifying laser pulses to the terawatt level at a 1-kilohertz repetition rate. *Applied Physics B*, 70(1):S165–S170, 2000.
- [11] M. Bellini, C. Lyngå, A. Tozzi, M. B. Gaarde, T. W. Hänsch, A. L’Huillier, and C.-G. Wahlström. Temporal coherence of ultrashort high-order harmonic pulses. *Phys. Rev. Lett.*, 81:297–300, Jul 1998.
- [12] J. L. Krause, K. J. Schafer, and K. C. Kulander. High-order harmonic generation from atoms and ions in the high intensity regime. *Physical Review Letters*, 68(24):3535, 1992.
- [13] P. B. Corkum. Plasma perspective on strong field multiphoton ionization. *Phys. Rev. Lett.*, 71:1994–1997, Sep 1993.
- [14] C. Winterfeldt, C. Spielmann, and G. Gerber. Colloquium: Optimal control of high-harmonic generation. *Reviews of Modern Physics*, 80(1):117, 2008.
- [15] L. Keldysh. Ionization in the field of a strong electromagnetic wave. *Sov. Phys. JETP*, 20(5):1307–1314, 1965.
- [16] H. R. Reiss. Effect of an intense electromagnetic field on a weakly bound system. *Physical Review A*, 22(5):1786, 1980.
- [17] K. Miyazaki and H. Takada. High-order harmonic generation in the tunneling regime. *Physical Review A*, 52(4):3007, 1995.
- [18] M. Protopapas, C. H. Keitel, and P. L. Knight. Atomic physics with super-high intensity lasers. *Reports on Progress in Physics*, 60(4):389, 1997.

- [19] K. Kulander and T. Rescigno. Effective potentials for time-dependent calculations of multi-photon processes in atoms. *Computer Physics Communications*, 63(1):523–528, 1991.
- [20] M. Lewenstein, P. Balcou, M. Y. Ivanov, A. l’Huillier, and P. B. Corkum. Theory of high-harmonic generation by low-frequency laser fields. *Physical Review A*, 49(3):2117, 1994.
- [21] N. Milosevic, A. Scrinzi, and T. Brabec. Numerical characterization of high harmonic attosecond pulses. *Physical review letters*, 88(9):093905, 2002.
- [22] P. Sauères, A. L’huillier, P. Antoine, and M. Lewenstein. Study of the spatial and temporal coherence of high-order harmonics. *Advances in atomic, molecular, and optical physics*, 41:83–142, 1999.
- [23] T. Pfeifer, C. Spielmann, and G. Gerber. Femtosecond x-ray science. *Reports on Progress in Physics*, 69(2):443, 2006.
- [24] P. Antoine, A. L’Huillier, and M. Lewenstein. Attosecond pulse trains using high-order harmonics. *Phys. Rev. Lett.*, 77:1234–1237, Aug 1996.
- [25] J. Itatani, J. Levesque, D. Zeidler, H. Niikura, H. Pépin, J.-C. Kieffer, P. B. Corkum, and D. M. Villeneuve. Tomographic imaging of molecular orbitals. *Nature*, 432(7019):867–871, 2004.
- [26] D. Shafir, Y. Mairesse, D. Villeneuve, P. Corkum, and N. Dudovich. Atomic wavefunctions probed through strong-field light–matter interaction. *Nature Physics*, 5(6):412–416, 2009.
- [27] E. Goulielmakis, M. Schultze, M. Hofstetter, V. S. Yakovlev, J. Gagnon, M. Uiberacker, A. L. Aquila, E. M. Gullikson, D. T. Attwood, R. Kienberger, F. Krausz, and U. Kleineberg. Single-cycle nonlinear optics. *Science*, 320(5883):1614–1617, 2008.
- [28] B. Shan, S. Ghimire, and Z. Chang. Effect of orbital symmetry on high-order harmonic generation from molecules. *PHYSICAL REVIEW-SERIES A-*, 69(2):021404–R, 2004.

- [29] G. Sansone, E. Benedetti, F. Calegari, C. Vozzi, L. Avaldi, R. Flammini, L. Poletto, P. Villoresi, C. Altucci, R. Velotta, S. Stagira, S. De Silvestri, and M. Nisoli. Isolated single-cycle attosecond pulses. *Science*, 314(5798):443–446, 2006.
- [30] The Kansas Light Source (KLS) provides high-intensity ultrafast laser light. <http://jrm.phys.ksu.edu/lasers.html>.
- [31] H. Wang, M. Chini, Y. Wu, E. Moon, H. Mashiko, and Z. Chang. Carrier-envelope phase stabilization of 5-fs, 0.5-mj pulses from adaptive phase modulator. *Appl Phys B*, 98:291–294, 2010.
- [32] X. Feng, S. Gilbertson, H. Mashiko, H. Wang, S. D. Khan, M. Chini, Y. Wu, K. Zhao, and Z. Chang. Generation of isolated attosecond pulses with 20 to 28 femtosecond lasers. *Phys. Rev. Lett.*, 103:183901, Oct 2009.
- [33] X. Feng, S. Gilbertson, H. Mashiko, H. Wang, S. D. Khan, M. Chini, Y. Wu, K. Zhao, and Z. Chang. Generation of isolated attosecond pulses with 20 to 28 femtosecond lasers. *Physical review letters*, 103(18):183901, 2009.
- [34] X. Feng, S. Gilbertson, S. D. Khan, M. Chini, Y. Wu, K. Carnes, and Z. Chang. Calibration of electron spectrometer resolution in attosecond streak camera. *Opt. Express*, 18:1316, 2010.
- [35] S. Gilbertson, M. Chini, X. Feng, S. Khan, Y. Wu, and Z. Chang. Monitoring and controlling the electron dynamics in helium with isolated attosecond pulses. *Physical review letters*, 105(26):263003, 2010.
- [36] Institute for the Frontier of Attosecond Science and Technology (iFAST). <http://ifast.ucf.edu/>.

- [37] K. Zhao, Q. Zhang, M. Chini, Y. Wu, X. Wang, and Z. Chang. Tailoring a 67 attosecond pulse through advantageous phase-mismatch. *Optics letters*, 37(18):3891–3893, 2012.
- [38] M. Chini, X. Wang, Y. Cheng, Y. Wu, D. Zhao, D. A. Telnov, S.-I. Chu, and Z. Chang. Sub-cycle oscillations in virtual states brought to light. *Scientific reports*, 3, 2013.
- [39] X. Wang, M. Chini, Y. Cheng, Y. Wu, X.-M. Tong, and Z. Chang. Subcycle laser control and quantum interferences in attosecond photoabsorption of neon. *Physical Review A*, 87(6):063413, 2013.
- [40] Y. Wu, E. Cunningham, H. Zang, J. Li, M. Chini, X. Wang, Y. Wang, K. Zhao, and Z. Chang. Generation of high-flux attosecond extreme ultraviolet continuum with a 10 TW laser. *Applied Physics Letters*, 102(20):201104–201104, 2013.
- [41] D. Strickland and G. Mourou. Compression of amplified chirped optical pulses. *Optics Communications*, 55(6):447–449, 1985.
- [42] G. Vaillancourt, T. Norris, J. S. Coe, P. Bado, and G. Mourou. Operation of a 1-khz pulse-pumped ti: sapphire regenerative amplifier. *Optics letters*, 15(6):317–319, 1990.
- [43] S. Backus, C. G. Durfee, M. M. Murnane, and H. C. Kapteyn. High power ultrafast lasers. *Review of scientific instruments*, 69(3):1207–1223, 1998.
- [44] A. Dubietis, G. Jonušauskas, and A. Piskarskas. Powerful femtosecond pulse generation by chirped and stretched pulse parametric amplification in bbo crystal. *Optics Communications*, 88(4):437–440, 1992.
- [45] I. Ross, P. Matousek, M. Towrie, A. Langley, and J. Collier. The prospects for ultrashort pulse duration and ultrahigh intensity using optical parametric chirped pulse amplifiers. *Optics Communications*, 144(1):125–133, 1997.

- [46] G. Cerullo and S. De Silvestri. Ultrafast optical parametric amplifiers. *Review of scientific instruments*, 74(1):1–18, 2003.
- [47] D. E. Spence, P. N. Kean, and W. Sibbett. 60-fsec pulse generation from a self-mode-locked ti:sapphire laser. *Opt. Lett.*, 16(1):42–44, Jan 1991.
- [48] U. Morgner, F. X. Kärtner, S. H. Cho, Y. Chen, H. A. Haus, J. G. Fujimoto, E. P. Ippen, V. Scheuer, G. Angelow, and T. Tschudi. Sub-two-cycle pulses from a kerr-lens mode-locked ti:sapphire laser. *Opt. Lett.*, 24(6):411–413, Mar 1999.
- [49] C. Cook. Pulse compression-key to more efficient radar transmission. *Proceedings of the IRE*, 48(3):310–316, march 1960.
- [50] O. Martinez. Design of high-power ultrashort pulse amplifiers by expansion and recompression. *Quantum Electronics, IEEE Journal of*, 23(8):1385–1387, 1987.
- [51] O. Martinez. 3000 times grating compressor with positive group velocity dispersion: Application to fiber compensation in 1.3-1.6 μm region. *Quantum Electronics, IEEE Journal of*, 23(1):59–64, 1987.
- [52] O. Martinez, J. Gordon, and R. Fork. Negative group-velocity dispersion using refraction. *JOSA A*, 1(10):1003–1006, 1984.
- [53] J. Murray and W. Lowdermilk. Nd: Yag regenerative amplifier. *Journal of Applied Physics*, 51(7):3548–3556, 1980.
- [54] K.-H. Hong, S. Kostritsa, T. J. Yu, J. H. Sung, I. W. Choi, Y.-C. Noh, D.-K. Ko, and J. Lee. 100-khz high-power femtosecond ti: sapphire laser based on downchirped regenerative amplification. *Optics Express*, 14(2):970–978, 2006.

- [55] S. Chen, M. Chini, H. Wang, C. Yun, H. Mashiko, Y. Wu, and Z. Chang. Carrier-envelope phase stabilization and control of 1 khz, 6 mj, 30 fs laser pulses from a ti: sapphire regenerative amplifier. *Applied optics*, 48(30):5692–5695, 2009.
- [56] C. Barty, T. Guo, C. Le Blanc, F. Raksi, C. Rose-Petruck, J. Squier, K. Wilson, V. Yakovlev, and K. Yamakawa. Generation of 18-fs, multiterawatt pulses by regenerative pulse shaping and chirped-pulse amplification. *Optics letters*, 21(9):668–670, 1996.
- [57] A. Rundquist, C. Durfee, Z. Chang, G. Taft, E. Zeek, S. Backus, M. Murnane, H. Kapteyn, I. Christov, and V. Stoev. Ultrafast laser and amplifier sources. *Applied Physics B: Lasers and Optics*, 65(2):161–174, 1997.
- [58] W. Lowdermilk and J. Murray. The multipass amplifier: Theory and numerical analysis. *Journal of Applied Physics*, 51(5):2436–2444, 1980.
- [59] C. L. Blanc, G. Grillon, J. Chambaret, A. Migus, and A. Antonetti. Compact and efficient multipass ti: sapphire system for femtosecond chirped-pulse amplification at the terawatt level. *Optics letters*, 18(2):140–142, 1993.
- [60] S. Backus, J. Peatross, C. Huang, M. Murnane, and H. Kapteyn. Ti: sapphire amplifier producing millijoule-level, 21-fs pulses at 1 khz. *Optics letters*, 20(19):2000–2002, 1995.
- [61] J. Valasek. Properties of rochelle salt related to the piezo-electric effect. *Physical Review*, 20(6):639, 1922.
- [62] M. Holland. Thermal conductivity of several optical maser materials. *Journal of Applied Physics*, 33(9):2910–2911, 1962.
- [63] A. C. DeFranzo and B. Pazol. Index of refraction measurement on sapphire at low temperatures and visible wavelengths. *Applied optics*, 32(13):2224–2234, 1993.

- [64] P. A. Schulz and S. R. Henion. Liquid-nitrogen-cooled $\text{Ti:Al}_2\text{O}_3/\text{Ti:CaF}_2/\text{Ti:CaF}_2$ laser. *Quantum Electronics, IEEE Journal of*, 27(4):1039–1047, 1991.
- [65] M. Zavelani-Rossi, F. Lindner, C. Le Blanc, G. Cheriaux, and J. Chambaret. Control of thermal effects for high-intensity Ti: Sapphire laser chains. *Applied Physics B*, 70(1):S193–S196, 2000.
- [66] D. C. Brown. The promise of cryogenic solid-state lasers. *Selected Topics in Quantum Electronics, IEEE Journal of*, 11(3):587–599, 2005.
- [67] See the data sheet of PT60 Cryorefrigerator, Cryomech, Inc. <http://www.cryomech.com/PT60.php>.
- [68] See the data sheet of Plane ruled reflection grating 53*-360R, Richardson Gratings, Newport Corporation. http://www.gratinglab.com/Products/Product_Tables/T2.aspx.
- [69] R. L. Fork, C. Cruz, P. Becker, and C. V. Shank. Compression of optical pulses to six femtoseconds by using cubic phase compensation. *Optics Letters*, 12(7):483–485, 1987.
- [70] M. Nisoli, S. De Silvestri, and O. Svelto. Generation of high energy 10 fs pulses by a new pulse compression technique. *Applied Physics Letters*, 68(20):2793–2795, 1996.
- [71] M. Nisoli, S. Stagira, S. De Silvestri, O. Svelto, S. Sartania, Z. Cheng, M. Lenzner, C. Spielmann, and F. Krausz. A novel-high energy pulse compression system: generation of multi-gigawatt sub-5-fs pulses. *Applied Physics B: Lasers and Optics*, 65(2):189–196, 1997.
- [72] M. Nisoli, S. De Silvestri, O. Svelto, R. Szipöcs, K. Ferencz, C. Spielmann, S. Sartania, and F. Krausz. Compression of high-energy laser pulses below 5 fs. *Optics letters*, 22(8):522–524, 1997.

- [73] A. Öffner. U.s. patent no. 2748015: Unit power imaging catoptric anastigmat, July 1973.
- [74] D. Du, J. Squier, S. Kane, G. Korn, G. Mourou, C. Bogusch, and C. T. Cotton. Terawatt ti:sapphire laser with a spherical reflective-optic pulse expander. *Optics letters*, 20(20):2114–2116, 1995.
- [75] G. Cheriaux, P. Rousseau, F. Salin, J. Chambaret, B. Walker, and L. Dimauro. Aberration-free stretcher design for ultrashort-pulse amplification. *Optics letters*, 21(6):414–416, 1996.
- [76] J. Seres, A. Müller, E. Seres, K. O’Keeffe, M. Lenner, R. F. Herzog, D. Kaplan, C. Spielmann, and F. Krausz. Sub-10-fs, terawatt-scale ti:sapphire laser system. *Optics letters*, 28(19):1832–1834, 2003.
- [77] A. A. Eilanlou, Y. Nabekawa, K. L. Ishikawa, H. Takahashi, and K. Midorikawa. Direct amplification of terawatt sub-10-fs pulses in a cpa system of ti:sapphire laser. *Opt. Express*, 16(17):13431–13438, Aug 2008.
- [78] C. Kopp, L. Ravel, and P. Meyrueis. Efficient beamshaper homogenizer design combining diffractive optical elements, microlens array and random phase plate. *Journal of Optics A: Pure and Applied Optics*, 1(3):398, 1999.
- [79] K. Ertel, C. Hooker, S. J. Hawkes, B. T. Parry, and J. L. Collier. Ase suppression in a high energy titanium sapphire amplifier. *Optics Express*, 16(11):8039–8049, 2008.
- [80] A. Siegman. *Lasers*. University Science Books, Mill Valley,CA, 1986.
- [81] Z. Cheng, F. Krausz, and C. Spielmann. Compression of 2 mj kilohertz laser pulses to 17.5 fs by pairing double-prism compressor: analysis and performance. *Optics communications*, 201(1):145–155, 2002.
- [82] P. F. Moulton. Ti-doped sapphire: tunable solid-state laser. *Optics News*, 8(6):9, Nov 1982.

- [83] H. Takada, M. Kakehata, and K. Torizuka. Broadband regenerative amplifier using a gain-narrowing compensator with multiple dielectric layers. *Japanese Journal of Applied Physics*, 43(11B):L1485–L1487, 2004.
- [84] M. Hentschel, Z. Cheng, F. Krausz, and C. Spielmann. Generation of 0.1-tw optical pulses with a single-stage ti: sapphire amplifier at a 1-khz repetition rate. *Applied Physics B*, 70(1):S161–S164, 2000.
- [85] H. Takada and K. Torizuka. Design and construction of a tw-class 12-fs ti:sapphire chirped-pulse amplification system. *Selected Topics in Quantum Electronics, IEEE Journal of*, 12(2):201 – 212, march-april 2006.
- [86] J. Dobrowolski and R. Kemp. Refinement of optical multilayer systems with different optimization procedures. *Applied Optics*, 29(19):2876–2893, 1990.
- [87] J. R. McNeil, A. C. Barron, S. Wilson, W. Herrmann Jr, et al. Ion-assisted deposition of optical thin films: low energy vs high energy bombardment. *Applied optics*, 23(4):552–559, 1984.
- [88] P. Martin. Ion-based methods for optical thin film deposition. *Journal of materials science*, 21(1):1–25, 1986.
- [89] See the data sheet of TLMB, TLM2. <https://www.cvimellesgriot.com/Products/TiSapphire-Mirrors.aspx>.
- [90] H. Takada, M. Kakehata, and K. Torizuka. Broadband high-energy mirror for ultrashort pulse amplification system. *Applied Physics B*, 70(1):S189–S192, 2000.
- [91] L. Yuan, Y. Zhao, H. He, and J. Shao. Femtosecond laser induced damage of optical coatings. *Chinese Optics Letters*, 5(101):S257–S259, 2007.

- [92] F. Eggenstein, F. Senf, T. Zeschke, and W. Gudat. Cleaning of contaminated xuv-optics at bessy ii. *Nuclear Instruments and Methods in Physics Research Section A: Accelerators, Spectrometers, Detectors and Associated Equipment*, 467:325–328, 2001.
- [93] E. Gubbini, G. Kommol, M. Schnürer, H. Schönagel, U. Eichmann, M. Kalashnikov, P. Nickles, F. Eggenstein, G. Reichardt, and W. Sandner. On-line cleaning of optical components in a multi-tw-ti: Sa laser system. *Vacuum*, 76(1):45–49, 2004.
- [94] E. Takahashi, Y. Nabekawa, and K. Midorikawa. Generation of 10- μ j coherent extreme-ultraviolet light by use of high-order harmonics. *Opt. Lett.*, 27(21):1920–1922, Nov 2002.
- [95] See the data sheet of Spectrogon Pulse Compression Gratings. <http://www.spectrogon.com/product-services/gratings/pulse-compression-gratings>.
- [96] R. Szipöcs, K. Ferencz, C. Spielmann, and F. Krausz. Chirped multilayer coatings for broadband dispersion control in femtosecond lasers. *Opt. Lett.*, 19(3):201–203, Feb 1994.
- [97] F. Kärtner, N. Matuschek, T. Schibli, U. Keller, H. Haus, C. Heine, R. Morf, V. Scheuer, M. Tilsch, and T. Tschudi. Design and fabrication of double-chirped mirrors. *Optics letters*, 22(11):831–833, 1997.
- [98] P. Tournois. Acousto-optic programmable dispersive filter for adaptive compensation of group delay time dispersion in laser systems. *Optics communications*, 140(4):245–249, 1997.
- [99] F. Verluise, V. Laude, Z. Cheng, C. Spielmann, and P. Tournois. Amplitude and phase control of ultrashort pulses by use of an acousto-optic programmable dispersive filter: pulse compression and shaping. *Optics Letters*, 25(8):575–577, 2000.

- [100] M. Yamashita, K. Yamane, and R. Morita. Quasi-automatic phase-control technique for chirp compensation of pulses with over-one-octave bandwidth-generation of few-to mono-cycle optical pulses. *Selected Topics in Quantum Electronics, IEEE Journal of*, 12(2):213–222, 2006.
- [101] B. Schenkel, J. Biegert, U. Keller, C. Vozzi, M. Nisoli, G. Sansone, S. Stagira, S. De Silvestri, and O. Svelto. Generation of 3.8-fs pulses from adaptive compression of a cascaded hollow fiber supercontinuum. *Optics letters*, 28(20):1987–1989, 2003.
- [102] R. Szipőcs and A. Kőházi-Kis. Theory and design of chirped dielectric laser mirrors. *Applied Physics B: Lasers and Optics*, 65(2):115–135, 1997.
- [103] Femtooptics catalog. http://www.femtolasers.com/fileadmin/documents/Leaflets/2013/FEMTOOPTICKatalog2013_06_HL.pdf, 2013.
- [104] See the data sheet of DAZZLER. <http://proxy.siteo.com.s3.amazonaws.com/www.fastlite.com/file/datasheet-dazzler-2013.pdf>.
- [105] See the data sheet of Liquid Crystal Spatial Light Modulators SLM-S640, JENOPTIK Optical Systems GmbH. http://www.jenoptik.com/en_generic_productpage?open&reopen=prodnav&pid=3765&ccm=020.
- [106] B. Xu, J. M. Gunn, J. M. D. Cruz, V. V. Lozovoy, and M. Dantus. Quantitative investigation of the multiphoton intrapulse interference phase scan method for simultaneous phase measurement and compensation of femtosecond laser pulses. *J. Opt. Soc. Am. B*, 23(4):750–759, Apr 2006.
- [107] B. Xu, Y. Coello, V. V. Lozovoy, D. A. Harris, and M. Dantus. Pulse shaping of octave spanning femtosecond laser pulses. *Opt. Express*, 14(22):10939–10944, 2006.

- [108] A. Baltuska, M. S. Pshenichnikov, and D. A. Wiersma. Second-harmonic generation frequency-resolved optical gating in the single-cycle regime. *Quantum Electronics, IEEE Journal of*, 35(4):459–478, 1999.
- [109] S. Akturk, C. D’Amico, and A. Mysyrowicz. Measuring ultrashort pulses in the single-cycle regime using frequency-resolved optical gating. *JOSA B*, 25(6):A63–A69, 2008.
- [110] L. Xu, N. Nakagawa, R. Morita, H. Shigekawa, and M. Yamashita. Programmable chirp compensation for 6-fs pulse generation with a prism-pair-formed pulse shaper. *Quantum Electronics, IEEE Journal of*, 36(8):893–899, 2000.
- [111] K.-H. Hong and C. H. Nam. Adaptive Pulse Compression of Femtosecond Laser Pulses Using a Low-Loss Pulse Shaper. *Japanese Journal of Applied Physics*, 43:5289, August 2004.
- [112] See the data sheet of Flexible Optical B.V. PDM-LIN20USB. <http://www.okotech.com/linear>.
- [113] P. Wnuk, C. Radzewicz, et al. Bimorph piezo deformable mirror for femtosecond pulse shaping. *Optics Express*, 13(11):4154–4159, 2005.
- [114] D. E. Goldberg, B. Korb, and K. Deb. Messy genetic algorithms: Motivation, analysis, and first results. *Complex systems*, 3(5):493–530, 1989.
- [115] G. Sansone, E. Benedetti, J.-P. Caumes, S. Stagira, C. Vozzi, M. Pascolini, L. Poletto, P. Villoresi, S. De Silvestri, and M. Nisoli. Measurement of harmonic phase differences by interference of attosecond light pulses. *Phys. Rev. Lett.*, 94:193903, May 2005.
- [116] P. B. Corkum, N. H. Burnett, and M. Y. Ivanov. Subfemtosecond pulses. *Opt. Lett.*, 19(22):1870–1872, Nov 1994.

- [117] V. T. Platonenko and V. V. Strelkov. Single attosecond soft-x-ray pulse generated with a limited laser beam. *J. Opt. Soc. Am. B*, 16(3):435–440, Mar 1999.
- [118] C. A. Haworth, L. E. Chipperfield, J. S. Robinson, P. L. Knight, J. P. Marangos, and J. W. G. Tisch. Half-cycle cutoffs in harmonic spectra and robust carrier-envelope phase retrieval. *Nat Phys*, 3(1):52–57, 2007.
- [119] A. de Bohan, P. Antoine, D. B. Milošević, and B. Piraux. Phase-dependent harmonic emission with ultrashort laser pulses. *Physical review letters*, 81(9):1837, 1998.
- [120] G. G. Paulus, F. Grasbon, H. Walther, P. Villoresi, M. Nisoli, S. Stagira, E. Priori, and S. De Silvestri. Absolute-phase phenomena in photoionization with few-cycle laser pulses. *Nature*, 414:182–184, Nov 2001.
- [121] M. Kling, C. Siedschlag, A. Verhoef, J. Khan, M. Schultze, T. Uphues, Y. Ni, M. Uiberacker, M. Drescher, F. Krausz, et al. Control of electron localization in molecular dissociation. *Science*, 312(5771):246–248, 2006.
- [122] A. Baltuska, T. Udem, M. Uiberacker, E. Hentschel, M. and Goulielmakis, C. Gohle, R. Holzwarth, V. S. Yakovlev, A. Scrinzi, T. W. Hansch, and F. Krausz. Attosecond control of electronic processes by intense light fields. *Nature*, 421(6923):611–615, 2003.
- [123] J. K. Ranka, R. S. Windeler, and A. J. Stentz. Visible continuum generation in air-silica microstructure optical fibers with anomalous dispersion at 800 nm. *Optics letters*, 25(1):25–27, 2000.
- [124] D. J. Jones, S. A. Diddams, J. K. Ranka, A. Stentz, R. S. Windeler, J. L. Hall, and S. T. Cundiff. Carrier-envelope phase control of femtosecond mode-locked lasers and direct optical frequency synthesis. *Science*, 288(5466):635–639, 2000.

- [125] F. Helbing, G. Steinmeyer, U. Keller, R. S. Windeler, J. Stenger, and H. R. Telle. Carrier-envelope offset dynamics of mode-locked lasers. *Opt. Lett.*, 27(3):194–196, Feb 2002.
- [126] F. Helbing, G. Steinmeyer, J. Stenger, H. Telle, and U. Keller. Carrier-envelope-offset dynamics and stabilization of femtosecond pulses. *Applied Physics B: Lasers and Optics*, 74:s35–s42, 2002. 10.1007/s00340-002-0898-4.
- [127] A. Baltuska, M. Uiberacker, E. Goulielmakis, R. Kienberger, V. Yakovlev, T. Udem, T. Hansch, and F. Krausz. Phase-controlled amplification of few-cycle laser pulses. *Selected Topics in Quantum Electronics, IEEE Journal of*, 9:972–989, Jul-Aug 2003.
- [128] M. Kakehata, H. Takada, Y. Kobayashi, K. Torizuka, Y. Fujihira, T. Homma, and H. Takahashi. Single-shot measurement of carrier-envelope phase changes by spectral interferometry. *Opt. Lett.*, 26(18):1436–1438, Sep 2001.
- [129] M. Takeda, H. Ina, and S. Kobayashi. Fourier-transform method of fringe-pattern analysis for computer-based topography and interferometry. *JosA*, 72(1):156–160, 1982.
- [130] C. Li, E. Moon, and Z. Chang. Carrier-envelope phase shift caused by variation of grating separation. *Optics letters*, 31(21):3113–3115, 2006.
- [131] Z. Chang. Carrier-envelope phase shift caused by grating-based stretchers and compressors. *Appl. Opt.*, 45(32):8350–8353, Nov 2006.
- [132] E. Treacy. Optical pulse compression with diffraction gratings. *Quantum Electronics, IEEE Journal of*, 5(9):454–458, 1969.
- [133] M. Hentschel, R. Kienberger, C. Spielmann, G. Reider, N. Milosevic, T. Brabec, P. Corkum, U. Heinzmann, M. Drescher, and F. Krausz. Attosecond metrology. *Nature*, 414(6863):509–513, 2001.

- [134] M. Drescher, M. Hentschel, R. Kienberger, G. Tempea, C. Spielmann, G. A. Reider, P. B. Corkum, and F. Krausz. X-ray pulses approaching the attosecond frontier. *Science*, 291(5510):1923–1927, 2001.
- [135] H. Mashiko, S. Gilbertson, C. Li, S. D. Khan, M. M. Shakya, E. Moon, and Z. Chang. Double optical gating of high-order harmonic generation with carrier-envelope phase stabilized lasers. *Phys. Rev. Lett.*, 100:103906, Mar 2008.
- [136] Z. Chang, A. Rundquist, J. Zhou, M. Murnane, H. Kapteyn, X. Liu, B. Shan, J. Liu, L. Niu, M. Gong, et al. Demonstration of a sub-picosecond x-ray streak camera. *Applied physics letters*, 69(1):133–135, 1996.
- [137] E. Goulielmakis, M. Uiberacker, R. Kienberger, A. Baltuska, V. Yakovlev, A. Scrinzi, T. Westerwalbesloh, U. Kleineberg, U. Heinzmann, M. Drescher, et al. Direct measurement of light waves. *Science*, 305(5688):1267–1269, 2004.
- [138] A. Stolow, A. E. Bragg, and D. M. Neumark. Femtosecond time-resolved photoelectron spectroscopy. *Chemical Reviews*, 104(4):1719–1758, 2004. PMID: 15080710.
- [139] H. Wang, M. Chini, S. Chen, C.-H. Zhang, F. He, Y. Cheng, Y. Wu, U. Thumm, and Z. Chang. Attosecond time-resolved autoionization of argon. *Physical review letters*, 105(14):143002, 2010.
- [140] A. Scrinzi, M. Y. Ivanov, R. Kienberger, and D. M. Villeneuve. Attosecond physics. *Journal of Physics B: Atomic, Molecular and Optical Physics*, 39(1):R1, 2006.
- [141] M. Ivanov, P. B. Corkum, T. Zuo, and A. Bandrauk. Routes to control of intense-field atomic polarizability. *Phys. Rev. Lett.*, 74:2933–2936, Apr 1995.

- [142] J. Mauritsson, P. Johnsson, E. Gustafsson, A. L’Huillier, K. J. Schafer, and M. B. Gaarde. Attosecond pulse trains generated using two color laser fields. *Phys. Rev. Lett.*, 97:013001, Jul 2006.
- [143] Y. Oishi, M. Kaku, A. Suda, F. Kannari, and K. Midorikawa. Generation of extreme ultraviolet continuum radiation driven by a sub-10-fs two-color field. *Opt. Express*, 14(16):7230–7237, Aug 2006.
- [144] Z. Chang. Controlling attosecond pulse generation with a double optical gating. *Phys. Rev. A*, 76:051403, Nov 2007.
- [145] H. Mashiko, S. Gilbertson, M. Chini, X. Feng, C. Yun, H. Wang, S. D. Khan, S. Chen, and Z. Chang. Extreme ultraviolet supercontinua supporting pulse durations of less than one atomic unit of time. *Opt. Lett.*, 34(21):3337–3339, Nov 2009.
- [146] S. Gilbertson, H. Mashiko, C. Li, E. Moon, and Z. Chang. Effects of laser pulse duration on extreme ultraviolet spectra from double optical gating. *Applied Physics Letters*, 93(11):111105, 2008.
- [147] P. Antoine, A. L’Huillier, M. Lewenstein, P. Salières, and B. Carré. Theory of high-order harmonic generation by an elliptically polarized laser field. *Physical Review A*, 53(3):1725, 1996.
- [148] C. Lyngå, A. L’Huillier, and C. Wahlström. High-order harmonic generation in molecular gases. *Journal of Physics B: Atomic, Molecular and Optical Physics*, 29(14):3293, 1996.
- [149] I. J. Sola, E. Mevel, L. Elouga, E. Constant, V. Strelkov, L. Poletto, P. Villoresi, E. Benedetti, J.-P. Caumes, S. Stagira, C. Vozzi, G. Sansone, and M. Nisoli. Controlling attosecond electron dynamics by phase-stabilized polarization gating. *Nat Phys*, 2:319–322, 2006.

- [150] T. Pfeifer, L. Gallmann, M. J. Abel, D. M. Neumark, and S. R. Leone. Single attosecond pulse generation in the multicycle-driver regime by adding a weak second-harmonic field. *Opt. Lett.*, 31(7):975–977, Apr 2006.
- [151] J. Itatani, F. Quéré, G. L. Yudin, M. Y. Ivanov, F. Krausz, and P. B. Corkum. Attosecond streak camera. *Physical review letters*, 88(17):173903–173903, 2002.
- [152] M. Y. Kuchiev and V. Ostrovsky. Quantum theory of high harmonic generation as a three-step process. *Physical Review A*, 60(4):3111, 1999.
- [153] N. B. Ammosov, M. V. Delone and V. P. Krainov. *Adk. Sov. Phys. JETP*, 64:1191, 1986.
- [154] D. M. Pennington, M. D. Perry, B. C. Stuart, R. D. Boyd, J. A. Britten, C. G. Brown, S. M. Herman, J. L. Miller, H. T. Nguyen, B. W. Shore, et al. Petawatt laser system. In *Second International Conference on Solid State Lasers for Application to ICF*, pages 490–500. International Society for Optics and Photonics, 1997.
- [155] M. Perry, D. Pennington, B. Stuart, G. Tietbohl, J. Britten, C. Brown, S. Herman, B. Golick, M. Kartz, J. Miller, et al. Petawatt laser pulses. *Optics Letters*, 24(3):160–162, 1999.
- [156] Y. Mairesse and F. Quéré. Frequency-resolved optical gating for complete reconstruction of attosecond bursts. *Physical Review A*, 71(1):011401, 2005.
- [157] J. Gagnon, E. Goulielmakis, and V. Yakovlev. The accurate frog characterization of attosecond pulses from streaking measurements. *Applied Physics B*, 92(1):25–32, 2008.
- [158] M. FieB, M. Schultze, E. Goulielmakis, B. Dennhardt, J. Gagnon, M. Hofstetter, R. Kienberger, and F. Krausz. Versatile apparatus for attosecond metrology and spectroscopy. *Review of Scientific Instruments*, 81(9):093103–093103, 2010.

- [159] T. Popmintchev, M.-C. Chen, O. Cohen, M. E. Grisham, J. J. Rocca, M. M. Murnane, and H. C. Kapteyn. Extended phase matching of high harmonics driven by mid-infrared light. *Optics letters*, 33(18):2128–2130, 2008.
- [160] S. P. Tewari and G. Agarwal. Control of phase matching and nonlinear generation in dense media by resonant fields. *Physical review letters*, 56(17):1811–1814, 1986.
- [161] S. Chin. Some fundamental concepts of femtosecond laser filamentation. *JOURNAL-KOREAN PHYSICAL SOCIETY*, 49(1):281, 2006.
- [162] P. Balcou, A. S. Dederichs, M. B. Gaarde, and A. L’Huillier. Quantum-path analysis and phase matching of high-order harmonic generation and high-order frequency mixing processes in strong laser fields. *Journal of Physics B: Atomic, Molecular and Optical Physics*, 32(12):2973, 1999.
- [163] A. L’huillier, M. Lewenstein, P. Salieres, P. Balcou, M. Ivanov, J. Larsson, and C. Wahlström. High-order harmonic-generation cutoff. *Physical review. A*, 48(5A):R3433–R3436, 1993.
- [164] M. Lewenstein, P. Salieres, and A. L’huillier. Phase of the atomic polarization in high-order harmonic generation. *Physical Review A*, 52(6):4747, 1995.
- [165] T. Ditmire, J. Crane, H. Nguyen, L. DaSilva, and M. Perry. Energy-yield and conversion-efficiency measurements of high-order harmonic radiation. *Physical Review A*, 51(2):R902, 1995.
- [166] E. Constant, D. Garzella, P. Breger, E. Mével, C. Dorrer, C. Le Blanc, F. Salin, and P. Agostini. Optimizing high harmonic generation in absorbing gases: Model and experiment. *Physical Review Letters*, 82(8):1668, 1999.

- [167] E. J. Takahashi, Y. Nabekawa, H. Mashiko, H. Hasegawa, A. Suda, and K. Midorikawa. Generation of strong optical field in soft x-ray region by using high-order harmonics. *Selected Topics in Quantum Electronics, IEEE Journal of*, 10(6):1315–1328, 2004.
- [168] J. L. Krause, K. J. Schafer, and K. C. Kulander. Calculation of photoemission from atoms subject to intense laser fields. *Physical Review A*, 45(7):4998, 1992.
- [169] M. Ferray, A. l’Huillier, X. Li, L. Lompre, G. Mainfray, and C. Manus. Multiple-harmonic conversion of 1064 nm radiation in rare gases. *Journal of Physics B: Atomic, Molecular and Optical Physics*, 21(3):L31, 1988.
- [170] C. G. Durfee III, A. R. Rundquist, S. Backus, C. Herne, M. M. Murnane, and H. C. Kapteyn. Phase matching of high-order harmonics in hollow waveguides. *Physical Review Letters*, 83(11):2187, 1999.
- [171] S. Kazamias, D. Douillet, F. Weihe, C. Valentin, A. Rousse, S. Sebban, G. Grillon, F. Aude, D. Hulin, and P. Balcou. Global optimization of high harmonic generation. *Physical review letters*, 90(19):193901, 2003.
- [172] E. J. Takahashi, H. Hasegawa, Y. Nabekawa, and K. Midorikawa. High-throughput, high-damage-threshold broadband beam splitter for high-order harmonics in the extreme-ultraviolet region. *Optics letters*, 29(5):507–509, 2004.
- [173] See the data sheet of Aberration-corrected concave gratings for flat-field spectrograph, grating number 001-0640, Hitachi High Technologies America, Inc. http://www.hitachi-hta.com/sites/default/files/ConcaveGrating-Spectrograph-Grazing%281%29_0.pdf.

- [174] X. Wang, M. Chini, Y. Cheng, Y. Wu, and Z. Chang. In situ calibration of an extreme ultraviolet spectrometer for attosecond transient absorption experiments. *Applied optics*, 52(3):323–329, 2013.
- [175] J. Ladislav Wiza. Microchannel plate detectors. *Nuclear Instruments and Methods*, 162(1):587–601, 1979.
- [176] L. Poletto, S. Bonora, M. Pascolini, and P. Villoresi. Instrumentation for analysis and utilization of extreme-ultraviolet and soft x-ray high-order harmonics. *Review of scientific instruments*, 75(11):4413–4418, 2004.
- [177] See the data sheet of Advanced Performance Long-Life Microchannel Plate Detector APD 275/32/25/8 I 40:1 NR 8”FM CT P47, PHOTONIS USA, Inc. <http://www.photonis.com/en/ism/22-advanced-performance-detectors-overview.html>.
- [178] S. Gilbertson, S. D. Khan, Y. Wu, M. Chini, and Z. Chang. Isolated attosecond pulse generation without the need to stabilize the carrier-envelope phase of driving lasers. *Phys. Rev. Lett.*, 105:093902, Aug 2010.
- [179] See the data sheet of UV photodiodes AXUV576C. <http://optodiode.com/pdf/AXUV576C.pdf>.
- [180] F. R. Powell, J. F. Lindblom, S. F. Powell, and P. W. Vedder. Thin film filter performance for extreme ultraviolet and x-ray applications. *Optical Engineering*, 29(6):614–624, 1990.
- [181] F. Ferrari, F. Calegari, M. Lucchini, C. Vozzi, S. Stagira, G. Sansone, and M. Nisoli. High-energy isolated attosecond pulses generated by above-saturation few-cycle fields. *Nat Photon*, 4(12):875–879, Dec 2010.
- [182] J. C. Baggesen, E. Lindroth, and L. B. Madsen. Theory of attosecond absorption spectroscopy in krypton. *Physical Review A*, 85(1):013415, 2012.

- [183] T. Popmintchev, M.-C. Chen, P. Arpin, M. M. Murnane, and H. C. Kapteyn. The attosecond nonlinear optics of bright coherent x-ray generation. *Nature Photonics*, 4(12):822–832, 2010.
- [184] E. Goulielmakis, Z.-H. Loh, A. Wirth, R. Santra, N. Rohringer, V. S. Yakovlev, S. Zherebtsov, T. Pfeifer, A. M. Azzeer, M. F. Kling, et al. Real-time observation of valence electron motion. *Nature*, 466(7307):739–743, 2010.
- [185] See the data sheet of QSI 520i Scientific Cooled CCD Camera, Quantum Scientific Imaging, Inc. <http://www.qsimaging.com/520overview.html>.